Romilkumar
Kantibhai Patel

Transmissores-Recetores de Baixa Complexidade para Redes Óticas

Simplified Coherent Transceiver for Optical Communication Networks

Romilkumar Kantibhai Patel

Transmissores-Recetores de Baixa Complexidade para Redes Óticas

Simplified Coherent Transceiver for Optical Communication Networks

Tese apresentada à Universidade de Aveiro para cumprimento dos requisitos necessários à obtenção do grau de Doutor em Engenharia Eletrotécnica, realizada sob a orientação científica do Professor Doutor **Armando Humberto Moreira Nolasco Pinto**, Professor Associado com Agregação do Departamento de Eletrónica, Telecomunicações e Informática (DETI), Universidade de Aveiro, e Doutor **Nelson de Jesus Cordeiro Muga**, Investigador do Instituto de Telecomunicações (IT), Universidade de Aveiro.

This work was supported in part by Fundação para a Ciência e a Tecnologia (FCT) through national funds, by the European Regional Development Fund (FEDER), through the Competitiveness and Internationalization Operational Programme (COMPETE 2020) of the Portugal 2020 framework, under the projects DSPMetroNet (POCI-01-0145-FEDER-029405), UIDB/50008/2020-UIDP/50008/2020 (action DigCORE). The Instituto de Telecomunicações Aveiro site was the host institution of this research work.

Fundação para a Ciência e a Tecnologia
MINISTÉRIO DA CIÊNCIA, TECNOLOGIA E ENSINO SUPERIOR

instituto de telecomunicações

REPÚBLICA PORTUGUESA
CIÊNCIA, TECNOLOGIA E ENSINO SUPERIOR
COMPETE 2020
PORTUGAL 2020
UNIÃO EUROPEIA
Fundo Europeu de Desenvolvimento Regional
DSP METRO Net
DigCORE

To my Parents!

Mrs.Ushaben Patel** & **Mr.Kantibhai Patel

o júri / the jury

presidente / president

Professor Doutor Amadeu Mortágua Velho da Maia Soares
Professor Catedrático da Universidade de Aveiro

vogais / examiners committee

Professor Doutor Adolfo da Visitação Tregeira Cartaxo
Professor Catedrático do Instituto Universitário de Lisboa e Investigador Sénior do Instituto de Telecomunicações (IT), Instituto Universitário de Lisboa

Professor Doutor Armando Humberto Moreira Nolasco Pinto
Professor Associado com Agregação da Universidade de Aveiro e Investigador Sénior do Instituto de Telecomunicações (IT), Universidade de Aveiro (Orientador)

Professora Doutora Maria do Carmo Raposo de Medeiros
Professora Associada da Universidade de Coimbra e Investigadora do Instituto de Telecomunicações (IT), Universidade de Coimbra

Professor Doutor Henrique Manuel de Castro Faria Salgado
Professor Associado da Universidade do Porto e Investigador Sénior do Instituto de Engenharia de Sistemas e Computadores, Tecnologia e Ciência (INESC TEC), Universidade do Porto

Professora Doutora Susana de Jesus Mota
Professora Auxiliar da Universidade de Aveiro, Investigadora do Instituto de Telecomunicações (IT), Universidade de Aveiro

Acknowledgment

I am deeply grateful to my supervisor Prof. Armando Pinto to guide me well throughout the research work from topic selection to finding the results and publications. Most importantly, he always showed his availability to address my queries and provide resources as and when needed in my Ph.D. journey. Conducting the academic study regarding such a difficult topic couldn't be as simple as he made this for me. Thank you Prof. Armando for guiding me (with big doses of patience) throughout this Ph.D. study!

I am also very grateful to my co-supervisor Dr. Nelson Muga for giving encouragement, sharing insightful suggestions, and providing constructive feedback throughout my research work. Thank you, Dr. Nelson, for proving me with all the needed resources to pursue my Ph.D. research and making the overall process as smooth as possible.

Two people from Instituto de Telecomunicações deserve a very special word of gratitude for their high impact contribution: one is Dr. Fernando Guiomar, who helped me analyse the overall work and provided very constructive feedback and suggestion. I always enjoyed technical discussions with him and he has played a major role in the experimental validation of the research study. The other person is Dr. Isiaka Alimi, who supported me in preparing and reviewing the research articles and other related documentation. In addition to the help in research work, he always showed his availability to help me in dealing with the paperwork and bureaucracies of immigrations. Their support will always be remembered!

I would like to thank Prof. Paulo Monteiro for granting me access to the required instruments in the laboratory, and Marco Fernandes for his support in the experimental setup. Also, I would like to thank Dr. Nuno Silva, Dr. Celestino Martins, Guilherme Domingues, Mariana Ramos, and Daniel Pereira for helping me one way or another in this Ph.D. journey.

I would like to acknowledge Departamento de Eletrónica, Telecomunicações e Informática (DETI) of the Universidade de Aveiro. I was greatly benefited from the well-structured coursework in the first year, it helped me pursue Ph.D. in the subsequent years. I would also acknowledge Instituto de Telecomunicações - Pólo de Aveiro for hosting this Ph.D. work and providing the state of the art facilities for research and development. Also, I would like to acknowledge projects DSPMetroNet and DigCORE for providing funding to this Ph.D. research.

Finally, my family deserves endless gratitude for unconditional support during my time here! Thank you very much to all! Muito obrigado a todos!

Palavras-chave

Comunicações óticas, deteção direta, transmissão de banda lateral única, relação de potência entre a portadora e o sinal, sinal de fase mínima, ruído de batimento de sinal-sinal, Kramers-Kronig, método de valor DC, fator de contribuição da portadora, mapeamento probabilístico

Resumo

Os sistemas de transcetores coerentes tradicionais permitem a codificação de informação em ambas quadraturas e em duas polarizações ortogonais do campo elétrico. Contudo, estes transcetores utilizados atualmente são baseados num esquema intradino, que requer dois híbridos óticos de 90^o e quatro pares de fotodetetores para sistemas de transmissão com polarização dupla, fazendo com que o custo destes sistemas seja pouco atrativo para aplicações de curto alcance. Por isso, métodos de banda lateral única com deteção direta, também referidos como transcetores coerentes simplificados, podem ser implementados como uma alternativa de baixo custo aos sistemas coerentes tradicionais. Contudo, o desempenho de sistemas de banda lateral única tradicionais é gravemente degradado pelo batimento sinal-sinal. Nesta tese foi desenvolvida uma nova arquitetura de transcetor coerente simplificada com um melhor desempenho para aplicações de curto alcance. Em particular, o desenvolvimento de técnicas de processamento digital de sinal para a reconstrução de fase, bem como de outros subsistemas de processamento digital de sinal que minimizem os requerimentos de hardware e a sua otimização de desempenho são o foco principal desta tese.

O princípio fundamental do transcetor proposto é baseado na receção de um sinal que satisfaz a condição mínima de fase na deteção direta. Para reconstruir a informação de fase em falta causada pela deteção direta, um novo método de *valor DC* que explora sinais de banda lateral única e as propriedades DC da condição de fase mínima é desenvolvido nesta tese. O método de *valor DC* facilita a reconstrução da fase à frequência de amostragem de Nyquist e requer um sinal piloto de baixa intensidade. Além disso, a validação experimental do método de *valor DC* foi executada com sucesso em ligações óticas de curto alcance. Adicionalmente, foi realizado um estudo intensivo do método de *valor DC* para otimizar o desempenho do sistema. Neste processo de otimização, verificou-se que o fator de contribuição da portadora é um parâmetro importante para explorar todas as vantagens do método de *valor DC*. Neste contexto, é proposto um novo método para a sua estimativa. Por último, o desempenho do método de *valor DC* é otimizado recorrendo a mapeamento probabilístico de constelação com taxa adaptativa.

keywords

Optical communications, direct-detection (DD), single sideband (SSB) transmission, carrier to signal power ratio (CSPR), minimum phase signal, signal-to-signal beating noise (SSBN), Kramers-Kronig (KK), DC-Value method, carrier contribution factor (CCF), probabilistic shaping

Abstract

Traditional coherent (COH) transceivers allow encoding of information in both quadratures and the two orthogonal polarizations of the electric field. Nevertheless, such transceivers used today are based on the intradyne scheme, which requires two 90^o optical hybrids and four pairs of balanced photodetectors for dual-polarization transmission systems, making its overall cost unattractive for short-reach applications. Therefore, SSB methods with DD reception, commonly referred to as self-coherent (SCOH) transceivers, can be employed as a cost-effective alternative to the traditional COH transceivers. Nevertheless, the performance of SSB systems is severely degraded. This work provides a novel SCOH transceiver architecture with improved performance for short-reach applications. In particular, the development of phase reconstruction digital signal processing (DSP) techniques, the development of other DSP subsystems that relax the hardware requirement, and their performance optimization are the main highlights of this research.

The fundamental principle of the proposed transceiver is based on the reception of the signal that satisfies the minimum phase condition upon DD. To reconstruct the missing phase information imposed by DD, a novel DC-Value method exploring the SSB and the DC-Value properties of the minimum phase signal is developed in this Ph.D. study. The DC-Value method facilitates the phase reconstruction process at the Nyquist sampling rate and requires a low intensity pilot signal. Also, the experimental validation of the DC-Value method was successfully carried out for short-reach optical networks. Additionally, an extensive study was performed on the DC-Value method to optimize the system performance. In the optimization process, it was found that the estimation of the CCF is an important parameter to exploit all advantages of the DC-Value method. A novel CCF estimation technique was proposed. Further, the performance of the DC-Value method is optimized employing the rate-adaptive probabilistic constellation shaping.

Contents

List of Figures

List of Tables

List of Acronyms

100 GbE 100 Gigabit ethernet
ADC analog to digital converter
ADSL asymmetric digital subscriber line
AGC automatic gain control
APD avalanche photodetector
ASE amplified spontaneous emission
ASK amplitude shift keying
AWGN additive white Gaussian noise
AWG arbitrary waveform generator
BER bit error rate
BPD balanced photodetector
BPS-DD block-wise phase switching direct-detection
BPS block-wise phase switching
CAP carrier-less amplitude and phase modulation
CCF carrier contribution factor
CD chromatic dispersion
CO-Rx coherent receiver
COH coherent
CPS carrier phase switching
CSF carrier suppression filter
CSPR carrier to signal power ratio
CW continuous wave
DAC digital to analog converter
DCF dispersion compensating fiber
DCI datacenter interconnect
DCN datacenter network
DD-OFDM direct-detected OFDM
DDMZM dual-drive Mach-Zehnder modulator

DD direct-detection
DFB distributed feedback
DML direct modulated laser
DMT discrete multitone
DM distribution matcher
DP dual-polarization
DR datacenter reach
DSB double sideband
DSP digital signal processing
DWDM dense wavelength division multiplexing
E/O electrical to optical
EAM electro-absorption modulator
ECL external cavity laser
EDC electronic dispersion compensation
EDFA erbium-doped fiber amplifier
EEPN equalization-enhanced phase noise
EML electro-absorption modulated laser
ENOB effective number of bits
ER extended reach
ESE electrical spectral efficiency
EVM error vector magnitude
FEC forward error correction
FFT fast Fourier transform
FIR finite impulse response
FR fiber reach
GMI generalized mutual information
GaAs gallium arsenide
HD-FEC hard-decision-FEC
IC interference cancellation
IFFT inverse fast Fourier transform
IID independent and identically distributed
IM-DD intensity modulation direct-detection
IM intensity modulation
IQ-MZM IQ Mach–Zehnder modulator
IQM IQ modulator
ISI inter-symbol interference

ITU-T ITU-Telecommunication Standardization Sector
InP indium phosphide
IoT Internet of Things
KK Kramers-Kronig
LO local oscillator
LR long reach
LSB lower sideband
LUT look-up-table
LiNbO3 lithium niobite
MIMO multiple input multiple output
MMF multi-mode fiber
MPC minimum phase condition
MPS minimum phase signal
MQW multiple quantum well
MZM Mach–Zehnder modulator
NGMI normalized generalized mutual information
NMSE normalized mean squared error
NRZ-OOK non-return to zero on-off keying
NRZ non-return to zero
O/E optical to electrical
OFDM orthogonal frequency division multiplexing
OM-4 optical mode-4
OOK on-off keying
OSA optical spectrum analyzer
OSNR optical signal to noise ratio
PAM pulse amplitude modulation
PAPR peak to average power ratio
PAS probabilistic amplitude shaping
PBC polarization beam combiner
PCS probabilistic constellation shaping
PDM-DD polarization division multiplexing direct-detection
PDM polarization division multiplexing
PMD polarization mode dispersion
QAM quadrature amplitude modulation
RF radio frequency
RIN relative intensity noise

RRC root raised cosine
RTO real-time oscilloscope
Rx-DSP receiver digital signal processing
Rx-EDC receiver electronic dispersion compensation
Rx receiver
S2P serial-to-parallel
SCI-DD signal carrier interleaved direct-detection
SCOH self-coherent
SCPS subcarrier phase switching
SD-FEC soft-decision-FEC
SE spectral efficiency
SF sideband filter
SMF single-mode fiber
SM single-mode
SNR signal to noise ratio
SPR set phase reversal
SPS samples per symbol
SQNR signal to quantization noise ratio
SR short reach
SSB-OFDM single sideband orthogonal frequency division multiplexing
SSBN signal-to-signal beating noise
SSB single sideband
SSLF single-stage linearization filter
SSMF standard single-mode fiber
SV-DD Stokes vector direct-detection
SiP silicon photonics
TE transverse electric
TIA trans-impedance amplifier
Tx-DSP transmitter digital signal processing
Tx-EDC transmitter electronic dispersion compensation
Tx transmitter
USB upper sideband
VCSEL vertical-cavity surface-emitting laser
VDSL2 very-high-speed DSL 2
VOA variable optical attenuator
VSSB vestigial single sideband

List of Symbols

$\mathcal{H}\{\bullet\}$	Hilbert Transform Operator
$\mathcal{F}\{\bullet\}$	Fourier Transform Operator
$\mathcal{F}^{-1}\{\bullet\}$	Inverse Fourier Transform Operator
$\Re\{\bullet\}$	Real Part
∞	Infinity
ω	Angular Frequency
$\approxeq$	Approximately Equal To
ε_n	Normalized Mean Square Error After n Iterations
ε_H	Threshold Normalized Mean Square Error
$\int$	Integration
$\int_x^y$	Integration Between x and y
$\langle\bullet\rangle$	Mean Value Operator
$\geq$	Greater Than Equal To
$\sqrt{\{\bullet\}}$	Square Root Operator
γ	Nonlinearity Coefficient of an Optical Fiber
$\lceil\bullet\rceil$	Ceiling Operator
σ^2	Noise Variance of the Additive White Gaussian Noise Channel

π	Pi
$\phi(t)$	Phase of the Minimum Phase Signal
$\sim$	Similar To
$\times$	Multiplication
$\pm$	Plus or Minus
δ_{FEC}	Non-ideal Forward Error Correction Performance Loss
δ_o	Offset Assigned to Carrier Contribution Factor
$\delta\theta_n(t)$	Phase Correction Vector in the DC-Value Method
λ	Shaping Parameter in Maxwell-Boltzmann Distribution
$\dagger$	kbits
ϱ	bits
ΔE_o	Carrier Contribution Factor Estimation Error
$3D$	3 Dimensional View
$2D$	2 Dimensional View
B	Bandwidth
$E(t)$	Complex Electric Field of the Minimum Phase Optical Signal
$E'_n(t)$	Digitally Reconstructed Minimum Phase Signal after $n-1$ Iterations
$\tilde{E'}_n(\omega)$	Fourier Transform of $E'_n(t)$
$E_n(t)$	Digitally Reconstructed Minimum Phase Signal after n Iterations
$\tilde{E}_n(\omega)$	Fourier Transform of $E_n(t)$
$E^*(t)$	Complex Conjugate of $E(t)$
$E_{ssb}(t)$	Complex Electric Field of Single Sideband Signal
$E_{ssb,i}(t)$	Imaginary Part of $E_{ssb}(t)$
$E_{ssb,r}(t)$	Real Part of $E_{ssb}(t)$

$E_{ssb}(z)$	Analytical Continuation of $E_{ssb}(t)$ in Complex z plane
f_o	Virtual Carrier Frequency
f_{clock}	Clock Frequency
f_s	Sampling Frequency
G	Gain
G_{PCS}	Achievable Shaping Gain
H_{CD}	Chromatic Dispersion
H_{CD}^{-1}	Chromatic Dispersion Compensation
$H_{DM,in}$	Entropy Fed in to Distribution Matcher
$H_{DM,out}$	Entropy Out from Distribution Matcher
H_{FEC}	Entropy Allocated for the Forward Error Correction Parity Bits
H_{PCS}	Overall Probabilistic Constellation Shaping Entropy
H_{quad}	Entropy of the Quadrant Bits
i	Imaginary Unit
I_k	In-phase k^{th} Transmitted Symbol
$\tilde{I}_k$	In-phase k^{th} Received Symbol
$I(t)$	Photocurrent
$I_{AC}(t)$	Photocurrent of AC-coupled Photodetector
$I_{DC}(t)$	Photocurrent of DC-coupled Photodetector
ln	Natural Logarithmic
$\log_2$	Logarithmic with Base 2
$\log_{10}$	Logarithmic with Base 10
M_{PCS}	Constellation Size of Probabilistic Constellation Shaping
M_{QAM}	Constellation Size of Uniform Quadrature Amplitude Modulation

p	Constant Scaling Factor
P_c	Carrier-Carrier Beating
P_s	Mean of Signal-Signal Beating
P_{s_k}	Symbols of the Shaped Constellations
P_{x_n}	Quadrature Amplitude Modulation Symbol Probabilities
Q	Quality Factor
Q_k	Quadrature k^{th} Transmitted Symbol
$\tilde{Q}_k$	Quadrature k^{th} Received Symbol
r	Constellation Point
R	Upsampling factor
R_b	Target Net Bit Rate in Probabilistic Constellation Shaping
$R_{b,min}$	Minimum Net Bit Rate in Probabilistic Constellation Shaping
$R_{b,max}$	Maximum Net Bit Rate in Probabilistic Constellation Shaping
R_{DM}	Rate of Distribution Matcher
R_{FEC}	Forward Error Correction Rate
R_{pd}	Photodetector Responsivity
R_{pil}	Digital Signal Processing Pilot Rate
R_s	Operating Symbol Rate
S_{21}	S Parameter of Photodetector
s_k	Symbols of the Shaped Constellations
t	Time
u_n	Symbols of the Uniform Constellations
V_{DD}	The Normalized Signal After the Square-law Detection
V_{pp}	Peak-to-Peak Voltage

x_n	n^{th} Symbol of Square Probabilistic Constellation Shaping
z	Complex z plane
$Z(\lambda)$	Partition Function to Normalize the Distribution

Chapter 1

Introduction

Coherent optical transmission schemes provide the solution for medium-to-long-reach optical links. Nevertheless, the cost of a coherent receiver is a major obstacle in the case of short-reach optical links such as datacenter, metro and access networks [1]. In fact, coherent receivers used today are based on the intradyne scheme, which requires optical hybrids, pairs of balanced photodiodes, and a requirement of a local oscillator (LO) making its overall cost unacceptably high for short-reach links above mentioned. In recent years, the requirement for low-cost solutions in short-reach optical communication links has led to a number of simpler, direct-detection (DD) based, transmission schemes [2]. The most common technique is the pulse amplitude modulation (PAM) scheme, which relies on the transmission of pulses of several amplitudes. Another popular approach is to employ an orthogonal frequency division multiplexing (OFDM) in such a manner that the OFDM tones are symmetric with respect to the center frequency with an introduction of a bias to prevent signal negativity [3], [4]. Nevertheless, the loss of phase information in DD methods limits the use of post-processing digital signal processing (DSP) which tends to limits DD transmission systems' capacity.

In an effort to overcome this issue, a simplified solution is to employ DD with the single sideband (SSB) transmission, which offers low-cost and low-complexity self-coherent (SCOH) transceiver architecture [5]. Nevertheless, the main challenge associated with the SSB transmission scheme is the inherent signal-to-signal beating noise (SSBN) generated upon the DD system. The SSBN falls within the signal bandwidth and interferes with the desired signal to carrier beating term. Therefore, in the quest for a cost-effective transceiver architecture, we should discover techniques that can effectively address the SSBN issue in the SSB transmission systems.

In this chapter, we present a discussion about the aim and objectives of the proposed research in the quest of finding a new cost-effective transceiver architecture for the applications in short-reach optical communication systems. This chapter is organized into four sections. Section 1.1 discusses the motivation of the work. Next, section 1.2 presents the goals of the research work. In section 1.3, the major contributions of the research work are summarized. Finally, the last section 1.4 present the organization of this Ph.D. thesis.

1.1 Motivation

Scaling the capacity of short-reach optical links relies on using multiple wavelengths or multiple fibers carrying conventional noncoherent modulation formats such as on-off keying (OOK) and, more recently, higher-order PAM [6]. As these formats encode information only in signal intensity, increasing the data rate per wavelength becomes progressively more challenging as the symbol rate increases. Also, these methods have a small tolerance to linear propagation effects, primarily chromatic and polarization-mode dispersion. Therefore, further scaling of the system capacity per wavelength requires more degrees of freedom to encode information. Conventional coherent detection with polarization multiplexing and a strong LO recovers phase and magnitude in each polarization, thus utilizing all four degrees of freedom of the optical channel while maximizing optical power efficiency [1], [7]. Coherent receivers are widely used in long-haul communications, but short-reach applications require redesigning those receivers to satisfy strict constraints on cost and power consumption. Research on SCOH detection for short-reach links has sought to meet those goals by simplifying receiver signal processing or simplifying receiver optics [8].

As mentioned earlier, the cost of a conventional coherent (COH) receiver makes it less suitable for short-reach applications. Due to the cost-sensitive nature of the short-reach applications, it may be desirable to utilize the single photodetector based DD transceivers configurations as it offers low complexity and cost of their optical hardware structure [9]. However, they impose an irreversible loss of phase information upon the square-law detection. Therefore, SSB methods have been employed to recover the missing phase information through the carrier-signal beating terms in DD optical communication systems [10], [11]. Nevertheless, the performance of SSB systems is severely degraded because of the nonlinear effect, introduced by the DD in the receiver (Rx), referred to as SSBN. The SSBN falls within the signal bandwidth and interferes with the wanted signal to carrier beating term causing a significant degradation in the Rx sensitivity [12].

The impact of the SSBN is maximum at the low frequencies and reduces to zero at a point equal to the bandwidth of an information signal. The adverse effect of the SSBN can be alleviated by enlarging the band-gap between the carrier and information signal [13], [14], however, these methods reduce the spectral efficiency. An alternative method to mitigate the effects of SSBN includes the utilization of multicore fibers and balanced detection discussed in [15]. In this method, the information signal with the carrier is transmitted in one core of the fiber while the other core contains only the information signal. At the receiver end, balanced detection is employed to mitigate the effect of the SSBN which ultimately increases the optical complexity. [15]. The iterative technique based on the linear filtering discussed in [16] works by calculating SSBN terms and subtracting them from the photodetected signal. The scheme can further help in enhancing the performance of the stage-based linearization filters. However, due to the inaccuracy of the SSBN approximation caused by the introduction of additional distortion by the linear filters, this technique has the drawback of limited effectiveness [16].

In this context, the key aim is to study the spectrally efficient transceiver architecture and reduce its implementation cost for short-reach applications. In particular, the development of new techniques to effectively alleviate the SSBN effect in the SSB optical communication sys-

tems is the main focus of this research work. Moreover, an extensive investigation on different potential solutions and their performance assessment focusing on the resource requirement are also carried to enable cost-effective and high-performance optical transceiver.

1.2 Objectives

For effective service delivery, the ensuing traffic transportation requires a consistent increase in bandwidth in optical fiber networks. Consequently, this imposes unprecedented bandwidth requirements on the short-to-medium reach optical transport networks. In this perspective, to satisfy diverse requirements such as robustness, flexibility, high bandwidth, and relatively reduced cost per unit bandwidth, bandwidth-efficient and cost-effective transmission systems have to be adopted. The main intent of this Ph.D. study is to develop simplified and cost-effective alternative solutions to traditional optical COH transceivers for supporting short-reach applications. The key objectives of the proposed study are to:

- Design and develop suitable and simplified SCOH transceiver architectures for the short-reach application in optical communication networks;
- Develop suitable DSP techniques for the SCOH transceiver architectures.
- Assess the complexity and optimization of the proposed techniques.
- Carry out the performance assessment and comparative analysis of the proposed techniques with the existing techniques.
- Perform experimental validation of the proposed phase recovery techniques.

To accomplish the aforementioned objectives of short-reach optical links, significant effort is given in studying and analyzing the SSB transmission techniques. The work focused on the SCOH systems in which the SSBN or the beating between the modulated signal and the copropagated continuous wave (CW) laser tone is exploited. In this context, effective means and related concepts of signal phase reconstruction based on the intensity information using the SCOH detection systems are presented. The work is divided into four main categories to realize the objectives of the Ph.D. research.

1.2.1 Detailed Study of the Optical Transceiver Architectures

This work involves a detailed analysis of the existing transceiver architectures deployed in the optical communication networks. The main objectives are to define the key parameters of the transceivers in terms of symbol rates, modulation formats, and links distances for the short-reach applications; and the analysis of the DSP subsystem requirements in the transceiver architectures. To fully accomplish these objectives, it is sub-divided into 2 parts as follows:

Transceiver architecture analysis

We started with the global analysis of the COH and DD transceiver architecture used in the optical communication network. This task should define the key design parameters like link distance, bandwidth, spectral efficiency, modulation formats, etc. and their implementation

cost involved in the optical communication networks.

Analysis of the DSP requirements

This includes investigating the minimum DSP subsystem requirements by taking into account the key design parameters discussed earlier for both the COH and DD transceiver architectures in the optical communication networks.

1.2.2 Study and Develop a Suitable Architecture for Short-reach Applications

This part is responsible for the development of a suitable architecture for the short-reach applications. The main objectives are to perform a comparative analysis of the optical and digital complexity involved in the COH and DD architectures in optical communication networks. and the development of an alternative cost-effective SCOH transceiver architecture suitable for the short-reach application. To fully accomplish these objectives, it is sub-divided into 2 parts as follows:

Complexity analysis of the transceiver architectures

After a general introduction to optical communication networking, presenting the most common standards in subsection 1.2.1, we explored the optical and digital complexity associated with the stated COH and DD transceiver architectures. The goal was to cope with the ever-increasing quest for higher transmission capacity and the cost-effectiveness requirement of the short-reach links.

Development of a new SCOH transceiver architecture

To meet the bandwidth, flexibility, and cost-effectiveness requirement of the future short-reach applications, we focused on the SSB transmission and DD system based SCOH transceiver approach. The SCOH transceiver architectures require the generation of an SSB signal with a co-propagating tone at the edge of the signal spectrum. Therefore, we explored suitable cost-effective techniques to generate SSB signals and co-propagating tone for the SCOH transceiver architectures. Additionally, we also performed a comparative analysis of the hardware requirement and their overall impact on the system performance for the possible way of generating a SCOH transceiver compatible signal.

1.2.3 Development of Techniques for the Self-Coherent (SCOH) Transceiver

This includes the development of new DSP techniques to effectively alleviate the effect of the SSBN in the DD optical systems and integrate them with the post-DSP subsystem of the traditional COH transceiver. The main objectives are to develop novel modulation format transparent DSP techniques for SCOH transceiver architectures; the development of DSP subsystems to make the SCOH Rx compatible with the post-DSP of the traditional COH Rxs; and the optimization of the computational demand of the proposed DSP techniques. To accomplish the stated objectives, it is sub-divided into 3 parts as follows:

Development of new DSP techniques for the SCOH

In this task, we performed an in-depth analysis of the DSP techniques adopted in the SSB optical communication. Thereupon, we developed a new set of DSP techniques to effectively get rid of the SSBN term in the DD optical communication system. We performed numerical validation of the proposed new DSP techniques using an in-house C++/MATLAB simulator, named NetXpto-LinkPlanner, developed by the researchers and Ph.D. students of the Instituto de Telecomunicações over the years. Moreover, we also assessed the performance of the proposed SSBN mitigation DSP techniques in comparison with the existing state-of-the-art techniques.

Development of DSP subsystem for the SCOH transceiver

This task includes the detailed analysis of the DSP subsystem required by the traditional COH transceiver and the SCOH transceiver, respectively. The goal was to integrate the SCOH transceiver with the existing traditional COH transceiver DSP subsystem.

Computational complexity analysis and optimization

A systematic study on the algorithms was carried out to lessen the computational complexity of the receiver DSP to improve speed and performance. This task includes the analysis and optimization of the complexity of DSP blocks. The analysis helps to understand the computational resource requirement of each DSP technique and pick out the most appropriate one for the hardware implementation.

1.2.4 Experimental Validation of SCOH Transceiver

This final objective is to experimentally implement and validate the DSP techniques in the short-reach application scenario. The transmission is supported by state-of-the-art testbeds utilized in the optical communications which include high-bandwidth PIN photodetector receivers, 1 Arbitrary Waveform Generator, 100 GSps Oscilloscope, a Mach-Zehnder modulator and other supporting equipment. The developed techniques are validated through offline processing (MATLAB environment) of the experimental data. Also, the comparative analysis of the developed DSP techniques for the SCOH transceiver is carried out with the other state of the art techniques in consideration of the quality of the recovered signal.

1.3 Major Contribution

This thesis proposes simplified and low-cost alternative solution for the short-reach optical links. The main contributions of this Ph.D. thesis can be summarized as follows:

- Proposed a novel approach, namely the DC-Value method, to reconstruct the phase information in DD optical links to address high sampling-rate requirement and sensitivity penalty problems in Kramers-Kronig based methods. [J1]
- Experimental validation of the proposed novel DC-Value method for short-reach application (80 km). [C1]

- A detailed investigation on the carrier contribution factor (CCF) constraint of the DC-Value method is carried out and proposed solutions to overcome challenges and improve the overall performance of the system. [J2]

- Optimization of the system performance employing probabilistic constellation shaping (PCS) in the minimum phase signal based transmission system. [J3]

Also, this thesis presents a comprehensive state of the art on the optical transceiver architectures, and also considers the requirements for a SCOH transceiver architectural evolution along with a piece of broad information on the technicalities of different related challenges and potential solutions. Besides that, some other contributions of this Ph.D. thesis can be summarized as follows:

- A comprehensive survey on SSB based transmission and reception and associated challenges with it. In this context, an overview of high-speed short-reach systems regarding their classifications, advanced optoelectronic devices, potential modulation formats, requirements, and challenges are well addressed in the state of the art. Also, it covers investigation on the minimum phase signal, how it can be generated and how we can benefit from them in the short-reach optical communication links. [J4]

- Active participation in the following projects:

  DSPMetroNet:
  The main objective is to investigate, develop and validate new technological paradigms in terms of optical coherent detection schemes and advanced DSP techniques to support optical coherent transceivers for future optical metro networks. The DSPMetroNet project enables the use of higher-order modulation formats along with higher data rates, and employment of more complex and computationally demanding DSP stages. Moreover, DSP eliminates the need for complex and costly compensation techniques applied in the optical domain.

  `http://dspmetronet.av.it.pt/index.html`

  SoftTransceiver:
  The primary technical objective of the project is to develop and implement a flexible optical transceiver prototype with software-driven reconfigurability and arbitrarily low bit-rate granularity. The development of this technology enables to increase the network capacity and the spectral/energy efficiency while providing a future-proof flexible solution for an increasingly heterogeneous global network.
  Moreover, employing Instituto de Telecomunicações's state-of-the-art laboratory facilities, all developed concepts, algorithms and components are thoroughly experimentally validated.

  `https://www.it.pt/Projects/Index/4268`

1.3.1 List of Publications

The major achievements obtained from the work of this thesis were submitted for peer review by the international scientific community through the list of publications (journals and conferences) that are listed below.

Journals

Author:

[J1] **Romil K. Patel**, Isiaka A. Alimi, Nelson J. Muga, and Armando N. Pinto, "Optical Signal Phase Retrieval with Low Complexity DC-Value Method", *IEEE/OSA Journal of Lightwave Technology*, August 2020.
https://ieeexplore.ieee.org/document/9064955

[J2] **Romil K. Patel**, Fernando P. Guiomar, Marco A. Fernandes, Isiaka A. Alimi, Paulo P. Monteiro, Nelson J. Muga, and Armando N. Pinto, "Impact of Carrier Contribution Factor in the Self-Coherent DC-Value Method", *Optics Express*, November 2021.
https://doi.org/10.1364/OE.444980

[J3] **Romil K. Patel**, Fernando P. Guiomar, Marco A. Fernandes, Isiaka A. Alimi, Paulo P. Monteiro, Nelson J. Muga, and Armando N. Pinto, "Implementation of Self-Coherent DC-Value Method with Adaptive Probabilistic Constellation Shaping", to be submitted to *IEEE/OSA Journal of Lightwave Technology*, 2022.

Co-author:

[J4] Isiaka A. Alimi, **Romil K. Patel**, Nuno A. Silva, Armando N. Pinto, Chuanbowen Sun, Honglin Ji, William Shieh, and Nelson J. Muga, "A Tutorial on Simplified Optical Coherent Transceivers for 5G and Beyond Networks", *Applied Sciences (Switzerland)*, August 2021.
https://doi.org/10.3390/app11167554

Conferences

Author:

[C1] **Romil. K. Patel**, Fernando P. Guiomar, Marco A. Fernandes, Isiaka A. Alimi, Paulo P. Monteiro, Nelson. J. Muga, and Armando. N. Pinto,"Virtual Carrier Assisted Self-Coherent Detection Employing DC-Value Method", Optical Fiber Communications Conference and Exhibition (OFC), San Francisco, USA, June 2021.
https://ieeexplore.ieee.org/document/9489986

Co-author:

[C2] Nelson. J. Muga, **Romil. K. Patel**, Isiaka. A. Alimi, Nuno. A. Silva and Armando. N. Pinto,"Self-coherent optical detection for access and metro networks", International Conference on Transparent Optical Networks (ICTON), Angers, France, July 2019
https://ieeexplore.ieee.org/document/8840560

[C3] Nelson. J. Muga, **Romil. K. Patel**, Isiaka. A. Alimi, Nuno. A. Silva and Armando. N. Pinto,"DSP optimization for simplified coherent receivers", International Conference on Transparent Optical Networks (ICTON), Bary, Italy, July 2020. `https://ieeexplore.ieee.org/document/9203090`

1.4 Thesis Structure

This thesis is organized into seven chapters. The Chapter 1 includes motivation, objectives, the major contribution of the study, and the overall structure of the thesis.

Chapter 2 presents a state of the art on the main requirements, technologies, architectures, and the major associated challenges of different transceiver systems in consideration with short-reach applications. It also presents the advantages of SCOH beyond the conventional intensity modulation direct-detection (IM-DD) while still relatively maintaining the simplicity and salient cost-efficiency feature for short and medium-reach applications.

Chapter 3 presents a novel SCOH technique namely the DC-Value method to reconstruct the missing phase information in the DD optical communication system. The chapter includes an in-depth theoretical, numerical and simulation analysis of the proposed DC-Value method. It also shows that the proposed method effectively alleviates the SSBN when compared with the other state-of-the-art techniques and reconstructs the full optical field in the digital domain.

Chapter 4 presents the experimental setup employed for the validation of the DC-Value method. The chapter includes a different method of generating SSB signal and discuss their associated complexity. It also presents a comparative analysis between the performance of the DC-Value method with the other state of the art techniques. Additionally, it includes a detailed explanation about the implementation of the state of the art phase recovery algorithms.

Chapter 5 presents the impact of the CCF in the DC-Value method as it is used to guarantee the minimum phase condition (MPC) for the DC-Value method algorithm. The chapter mainly includes the CCF sensitivity analysis in the minimum phase signal reconstruction and its overall impact on the system performance. It also covers a novel proposed method to calculate the value of the CCF at the receiver-end and assesses its effectiveness in the DC-Value method.

Chapter 6 presents an experimental performance analysis of the DC-Value method employing the rate-adaptive PCS. It presents a brief discussion about PCS modulations and assesses its performance for short-reach optical links. The chapter also includes a discussion about performance assessment metrics such as generalized mutual information (GMI) and normalized generalized mutual information (NGMI).

Finally, the main conclusions of the thesis and some suggestions for future research work are summarized in Chapter 7.

References

[1] A. Shahpari, R. M. Ferreira, R. S. Luis, *et al.*, "Coherent Access: A Review," *IEEE/OSA Journal of Lightwave Technology*, vol. 35, no. 4, pp. 1050–1058, 2017.

[2] S. Randel, F. Breyer, S. C. J. Lee, *et al.*, "Advanced Modulation Schemes for Short-Range Optical Communications," *IEEE Journal of Selected Topics in Quantum Electronics*, vol. 16, no. 5, pp. 1280–1289, 2010.

[3] T. Takahara, T. Tanaka, M. Nishihara, *et al.*, "Discrete Multi-Tone for 100 Gb/s Optical Access Networks," *Optical Fiber Communications Conference and Exhibition (OFC)*, p. M2I.1, 2014.

[4] A. Weiss, A. Yeredor, and M. Shtaif, "Iterative Symbol Recovery for Power-Efficient DC-Biased Optical OFDM Systems," *IEEE/OSA Journal of Lightwave Technology*, vol. 34, no. 9, pp. 2331–2338, 2016.

[5] M. Schuster, S. Randel, C. A. Bunge, *et al.*, "Spectrally Efficient Compatible Single-Sideband Modulation for OFDM Transmission With Direct Detection," *IEEE Photonics Technology Letters*, vol. 20, no. 9, pp. 670–672, 2008.

[6] K. Zhong, X. Zhou, T. Gui, *et al.*, "Experimental study of PAM-4, CAP-16, and DMT for 100 Gb/s Short Reach Optical Transmission Systems," *Optics Express*, vol. 23, no. 2, pp. 1176–1189, 2015.

[7] E. Ip, A. P. T. Lau, D. J. F. Barros, *et al.*, "Coherent Detection in Optical Fiber Systems," *Optics Express*, vol. 16, no. 2, pp. 753–791, 2008.

[8] J. K. Perin, A. Shastri, and J. M. Kahn, "Coherent Data Center Links," *IEEE/OSA Journal of Lightwave Technology*, vol. 39, no. 3, pp. 730–741, 2021.

[9] D. Che, Q. Hu, and W. Shieh, "Linearization of Direct Detection Optical Channels Using Self-Coherent Subsystems," *IEEE/OSA Journal of Lightwave Technology*, vol. 34, no. 2, pp. 516–524, 2016.

[10] W. Peng, X. Wu, V. R. Arbab, *et al.*, "Theoretical and Experimental Investigations of Direct-Detected RF-Tone-Assisted Optical OFDM Systems," *IEEE/OSA Journal of Lightwave Technology*, vol. 27, no. 10, pp. 1332–1339, 2009.

[11] M. S. Erkılınç, S. Pachnicke, H. Griesser, *et al.*, "Performance Comparison of Single-Sideband Direct Detection Nyquist-Subcarrier Modulation and OFDM," *IEEE/OSA Journal of Lightwave Technology*, vol. 33, no. 10, pp. 2038–2046, 2015.

[12] A. J. Lowery, "Amplified-spontaneous Noise Limit of Optical OFDM Lightwave Systems," *Optics Express*, vol. 16, no. 2, pp. 860–865, 2008.

[13] A. J. Lowery and J. Armstrong, "Orthogonal-frequency-division multiplexing for Dispersion Compensation of Long-haul Optical Systems," *Optics Express*, vol. 14, no. 6, pp. 2079–2084, 2006.

[14] J. Ma, "Simple Signal-to-Signal Beat Interference Cancellation Receiver Based on Balanced Detection for a Single-Sideband Optical OFDM Signal with a Reduced Guard Band," *Optics Letters*, vol. 38, no. 21, pp. 4335–4338, 2013.

[15] Y. Wang, Z. Wang, Y. Shen, *et al.*, "Beyond 100-Gb/s Single-sideband Direct Detection Using Multi-core Fiber and SSBI Elimination," *Opto-Electronics and Communications Conference (OECC) and Photonics Global Conference (PGC)*, pp. 1–3, 2017.

[16] Z. Li, M. S. Erkılınç, K. Shi, *et al.*, "SSBI Mitigation and the Kramers–Kronig Scheme in Single-Sideband Direct-Detection Transmission With Receiver-Based Electronic Dispersion Compensation," *IEEE/OSA Journal of Lightwave Technology*, vol. 35, no. 10, pp. 1887–1893, 2017.

Chapter 2

Short-Reach Transceivers

Intense research efforts are being made focusing on enhancing the performance of the short-reach systems through the adoption of the coherent transmission system. Nevertheless, due to the main concern regarding the cost in the short-reach transceivers market, the direct application of the traditional coherent (COH) system concepts into the short-reach links is unattractive. Hence, for effective support of different applications and services, innovative schemes regarding detection, signaling, and digital signal processing (DSP) are of paramount importance.

In this perspective, to satisfy diverse requirements such as robustness, flexibility, and reduced cost per unit bandwidth, cost-effective and bandwidth-efficient transmission systems have to be adopted. One of such effective technique that enables self-coherent (SCOH) solution is to deploy single sideband (SSB) transmission with a direct-detection (DD) receiver [1]. The SCOH schemes are opening up new prospects for ultra-high-capacity transceivers. They present remarkable advantages beyond the conventional intensity modulation direct-detection (IM-DD) while still relatively maintaining the simplicity and salient cost-efficiency feature for the short- and medium reach applications [1], [2].

This chapter presents a state of the art short-reach systems with their enabling technologies and standards with the main focus on the short-reach optical links such as metro and access networks and datacenter networks (DCNs). This chapter is organized into four sections. Section 2.1 discusses the potential technologies for the short-reach optical networks. Next, section 2.2 presents various the SCOH transceiver architectures. In section 2.3, various signal generation techniques and structures of the state of the art SCOH transceiver are presented. Finally, the last section 2.4 presents the concluding remarks.

2.1 Enabling Technologies for Short-reach Optical Networks

This section discusses the current state of the art for the short-reach systems with the main focus on the metro and access networks and DCNs. Also, the related short-reach system features such as classifications, potential modulation formats, advanced optoelectronic devices, standards, requirements, and challenges that necessitate novel transceiver architectures and DSP techniques are comprehensively analyzed.

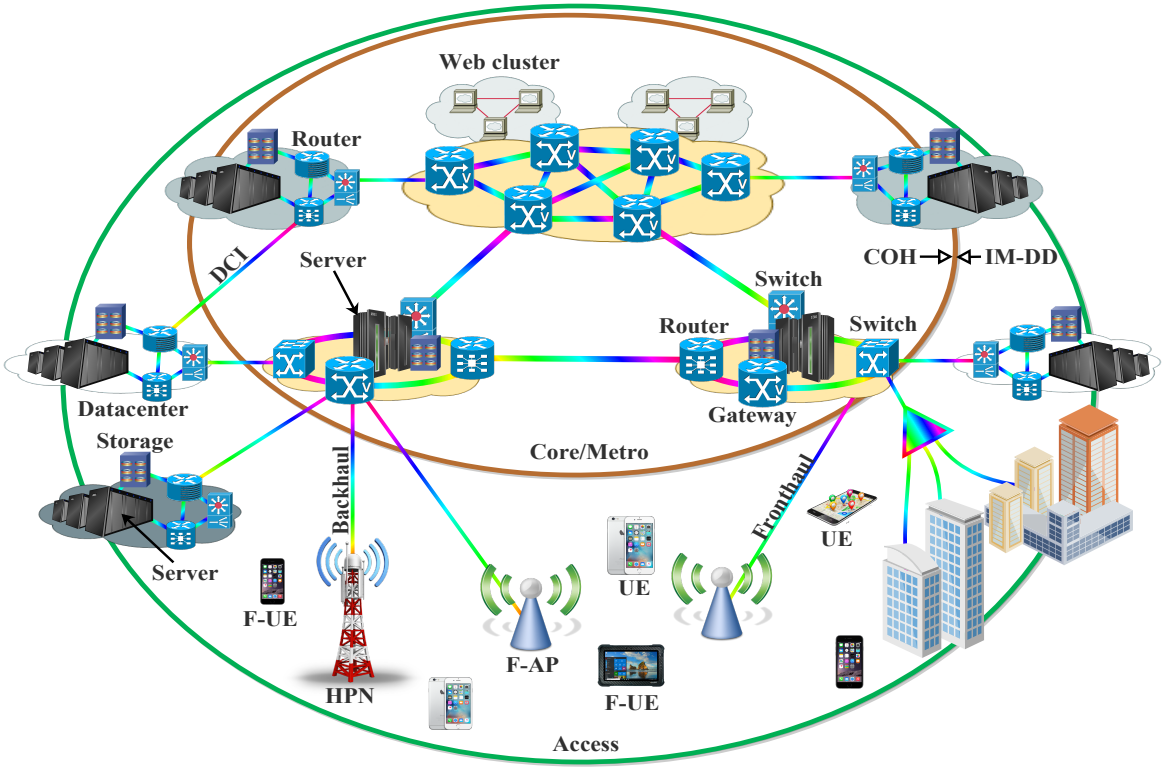

Figure 2.1: Typical access, metro, and core network scenarios depicting intra-/inter-datacenter links. DCI: Datacenter interconnects; F-AP: Fog-computing-based access point; UE: User equipment; F-UE: "smart" user equipment; HPN: High-power nodes. (adapted from [4])

2.1.1 Short-reach System Overview

The short-reach connections are optical communication links that are in the range of hundreds of meters to tens of kilometers. Within intra-DCNs, they are appropriate for connecting one server to another. Besides, they are applicable to inter-DCNs as well.

2.1.1.1 Short-reach Systems Classification

A typical optical communication scenario is illustrated in Fig. 2.1. The infographic depicts the core/metro and access network along with the intra-/inter-DCN links. It should be noted that the demarcation point for the digital coherent and IM-DD solution applications is increasingly becoming unclear with a growing quest for low-cost but high-capacity transceivers. In this regard, there exist different economic and technical challenges to keep abreast of the bandwidth increase for IM-DD based solutions [3]. Based on the supported transmission distance, the 100 Gigabit ethernet (100 GbE) transceiver standards can be grouped as shown in Table 2.1 [3]. Generally, the short-reach systems can be grouped in line with the associated technological features and limiting factors. They can be broadly grouped into intra-datacenter, inter-datacenter, as well as extended reach inter-datacenter, access and metro links [5].

Table 2.1: 100 GbE Transceivers Standards Group (adapted from [5])

Groups	Descriptions
Short reach (SR)	This can support around 100 m optical mode-4 (OM-4) multi-mode fiber (MMF) links.
Datacenter reach (DR)	It can support around 500 m single-mode fiber (SMF) links.
Fiber reach (FR)	It is mainly for supporting approximately 2 km SMF.
Long reach (LR)	It is capable of supporting up to 10 km SMF.
Extended reach (ER)	This can support around 40 km SMF.

Intra-Datacenter or Server-to-Server Links

In a DCN, intra-datacenter or server-to-server links are the data links that connect one server to another and the racks together inside the DCN. These kinds of links are usually lying below 300 m and they comprise the major amount of the datacenter interconnects (DCIs). Currently, the links are dominated by MMF and vertical-cavity surface-emitting laser (VCSEL) transmitters. Since the link is mainly based on the MMF, the major limiting factor is the associated inter-modal dispersion [3], [5].

Inter-Datacenter Links

Inter-datacenter links are usually below 20 km and are typically employed to connect one datacenter to another and ensure data exchange between multiple DCNs [3], [5]. Furthermore, they are usually referred to as DCI [3]. Unlike what entails in the intra-datacenter links, the inter-datacenter links exploit the standard single-mode fiber (SSMF). This is mainly owing to the length scale that is too long for the MMF implementation. Employment of MMF for this length scale can bring about an inter-modal dispersion. Furthermore, with an increase in the chromatic dispersion (CD) effects in conjunction with the baud rate and distance, the DD scheme limits the system performance. Consequently, the CD effects have to be attended to by exploiting innovative signaling and DSP techniques.

Extended Reach Inter-Datacenter, Access and Metro Links

As these links can be between 20 km and 80 km, an optical amplification can be employed in certain scenarios. Despite this, DD receivers are still the preferred candidates for these applications when compared with the full coherent receivers (CO-Rxs). Therefore, to enhance the bit rate, polarization-multiplexed DD configurations like the Stokes vector direct-detection (SV-DD) receivers have been receiving considerable attention. Alternatively, various intensive efforts are being made towards enhancing the bit rate, as well as the transmission distance of O-band systems without the need for optical amplification [5].

2.1.1.2 Potential Modulation Formats

The employment of advanced modulation formats may be indispensable in the realization of a high data rate systems if optical and electrical components with higher bandwidth are not commercially available. In the following, we present some advanced high order modulation formats that can be exploited to scale the transmission speed of short-reach systems.

Pulse Amplitude Modulation

The simplest high order modulation format for achieving a higher bit rate with limited bandwidth components is pulse amplitude modulation (PAM). Compared to the non-return to zero on-off keying (NRZ-OOK) format, information bits can be encoded on multiple optical amplitude levels like PAM-4, PAM-8, or PAM-16. However, the non-return to zero (NRZ) modulation format is more tolerant of inter-symbol interference (ISI) compared to a multi-level intensity signaling like PAM-M [3], [6]. Furthermore, it is noteworthy that when the level number doubles, the receiver sensitivity will be significantly reduced. So, a higher optical signal to noise ratio (OSNR) is usually demanded by the higher-order PAM signals. Besides being more susceptible to channel impairments like the CD, they demand DSP schemes that are more complex. Therefore, PAM-4 is a more practical and promising alternative compared with higher-order PAM signals [5], [7]. Therefore, regarding the implementation complexity and system performance, it has been considered as a more attractive format for short-reach applications [8]. Remarkably, PAM-4 has been adopted by the IEEE 400GbE P802.3bs task force for the DCI [5], [7]. Also, PAM-4 has been adopted by the 100GBASE-KP4 for electrical backplane interconnects [9].

Carrier-less Amplitude and Phase modulation

The Bell Laboratories proposed carrier-less amplitude and phase modulation (CAP) modulation for asymmetric digital subscriber line (ADSL) applications to improve the transmission capacity through orthogonal multiplexing method [10], [11], [12]. It facilitates the quadrature amplitude modulation (QAM)-type signal generation with relatively simpler implementation [5]. Unlike the QAM scheme where individual data streams are modulated, a digital filtering process is employed in the CAP for the generation of quadrature signals without additional carriers. To achieve this, the CAP transmitter generates a QAM-like signal through the combination of the Hilbert pair of two filtered multilevel signals [13], [10]. In this regard, the CAP system implementation is relatively simple. However, CAP is highly sensitive to non-flat channel frequency responses.

Discrete multi-tone modulation

Discrete multitone (DMT) is a category of orthogonal frequency division multiplexing (OFDM) scheme and it is known as direct-detected OFDM (DD-OFDM). In the DMT, the frequency spectrum is divided into orthogonally modulated subcarriers. Then, the input data sequence is electrically encoded onto each subcarrier. Also, being a multi-carrier modulation scheme, it presents attractive features such as flexible multi-level coding, high spectral efficiency (SE), and high tolerance to channel impairments. As aforementioned, DMT is being implemented in the ITU-Telecommunication Standardization Sector (ITU-T) ADSL standard and it is later adopted for the ITU-T very-high-speed DSL 2 (VDSL2) standard. Also, it has been attracting considerable attention for the low-cost and bandwidth limited short-reach communication applications. This is because of its inherent flexibility for shaping the transmitted signal's frequency spectrum [3], [14]. Nonetheless, like other multi-carrier schemes such as OFDM, DMT presents a high peak to average power ratio (PAPR) issue. The high PAPR issue usually has considerable influence on the DMT's tolerance to the relative intensity noise (RIN), as well as the analog to digital converter (ADC) and digital to analog converter (DAC) resolution requirements [3], [15], [16].

2.1.1.3 Advanced Optoelectronic Devices for Datacenter Interconnects (DCIs)

Apart from the advanced modulation formats that have been discussed so far, different research efforts are being made on optoelectronic devices and components for supporting high-speed DCIs. This subsection focuses on different devices for short-reach transmissions systems.

Vertical cavity surface-emitting laser

The gallium arsenide (GaAs) 850 nm multimode (MM) VCSEL in conjunction with MMF are widely employed in the commercial short-reach intra-DCI. However, one of the main performance limitations of this implementation is the modal dispersion that may be instigated by the differential modal delay in the MMF [3], [17]. The modal dispersion effect can be mitigated by employing a single-mode or few-mode operation. Based on this, SMF deployment will be a promising option for supporting the evolving hyper-scale DCNs. Similarly, adoption of single-mode (SM) VCSEL-based technologies that are capable of mitigating the CD effects and supporting spectrally efficient transmissions over an extended reach is also an attractive option [14], [18], [19]. Nevertheless, the major weaknesses of SM VCSELs are that they usually have limited output power and demand further complex optical alignment. Furthermore, VCSELs emitting at 980 nm [18], [19], 1060 nm [20]–[22] and 1100 nm [23], [24] with negligible increase in fabrication complexities and significantly high modulation bandwidths have been studied in the upper limit of GaAs technology [3].

Direct modulated laser

Direct modulated laser (DML) typically generates high output power and has been considered to be more power- and cost-efficient approach compared with the external modulation solutions. This is because the laser bias current is driven directly by the modulated signal. Moreover, due to their compactness, they can be easily integrated with other devices. Based on the associated features, DMLs have been considered as attractive solutions for cost-sensitive DCNs and access networks. Nevertheless, the DML capability for high-speed data links is hindered by the limited modulation bandwidth. To attend to the drawback, many viable techniques can be adopted along with advanced modulation formats and DSP. For instance, the DML modulation bandwidth can be enhanced through the exploitation of innovative design and techniques such as multisection laser design [25], multiple quantum wells (MQWs) laser design [3], [25], and injection locking [3], [26]. Moreover, another limiting factor for the DML-based system is the spectrum broaden which is mainly due to the inherent chirp effect. There are several techniques both in optical and digital domains that can be employed to address the chirp effect [3], [27]–[29].

Mach–Zehnder modulator

The Mach–Zehnder modulator (MZM) has been widely employed in the IM-DD optical communications for external modulation. It is noteworthy that commercial MZMs are usually made from lithium niobite (LiNbO3) and are capable of supporting high-capacity transmissions [30]. Nevertheless, they are typically packaged into bulky modules that are not only expensive but also energy-intensive. So, their application for client-side optical interfaces like pluggable optical transceivers is hindered. These challenges can be addressed by the employment of monolithically integrated LiNbO3 electro-optic modulators [31]. Likewise, MZMs that are based on an indium phosphide (InP) can be produced at low-cost and be monolithi-

cally integrated into a small size [3], [30]. Additionally, silicon photonics (SiP)-based MZMs fabricated with wafer-scale technology are also viable solutions [30], [32]. In this context, there have been intensive research efforts made on multi-electrode MZM [33], [34], and SiP-based traveling-wave MZM [35], [36].

Double-side electro-absorption modulated lasers

Electro-absorption modulated lasers (EMLs) are based on a well developed technology and have been extensively employed for short-reach links because of the associated advantages such as high bandwidth, small form-factor, and large extinction ratio [37]. Typically, an EML has just one modulated output and the other output is normally employed for monitoring. In a double-side EML, two electro-absorption modulators (EAMs) are integrated on both sides of the laser. Consequently, two independent optical modulated signals can be offered at the same wavelength by a double-side EML. It should be noted that it is relatively challenging to generate polarization division multiplexing (PDM) signals by employing two discrete EML. This is owing to the relative wavelength drifting. In this regard, a double-side EML is an ideal solution for PDM signal generation due to the offered two independent modulated outputs at the same wavelength [5], [37].

Electro-absorption modulator integrated with a distributed feedback laser

In the commercial 10G and 25G transceiver applications, distributed feedback (DFB) laser with EAM (EA-DFB) lasers have been widely employed [38]. Compared with the DML, the EA-DFB lasers offer notable advantages such as an improved extinction ratio, better modulation linearity, and enhanced bandwidth. In general, short-reach transmission based on PAM-4 or 8, with both separated or integrated modulators and lasers can support 100 Gb/s per lane. Nevertheless, the DMLs or EMLs system performances are limited by factors such as the modulation bandwidth and the electro-optical components' nonlinear impairments for modulation and detection of the signal.

Semiconductor optical amplifier (SOA)-PIN/TIA Receiver

To realize a high-power budget or receiver sensitivity, optical pre-amplification employment is essential. This can be achieved by employing erbium-doped fiber amplifiers (EDFAs). However, the EDFA implementation results in relatively higher costs and larger footprints, making it inappropriate for short-reach applications. To address this, a monolithic integrated semiconductor optical amplifier PIN/TIA receiver can be employed. Nonetheless, it operates only in the transverse electric (TE) polarization.

High-bandwidth APD Receiver

Compared with the PIN diode, an avalanche photodetector (APD) has a much higher responsivity. Based on this, it is an attractive device that can help in achieving high receiver sensitivity, low-cost, and long-reach transmission. Besides, it is a promising device for future high-speed applications due to its ease of integration with other silicon photonics devices [5].

2.1.1.4 Requirements and Challenges

This part presents several system requirements and the specific constraints that make the application of conventional COH systems, that are meant for long-haul systems, inappropriate for the short-reach systems. Consequently, the associated system requirements prompt

further research directions on novel transceiver architectures and DSP techniques. These are being discussed in the following section.

Cost

The short-reach transceiver applications require low-cost, so, high-performance devices such as thermoelectric cooling, LiNbO3 external modulators, and low bandwidth external cavity lasers (ECLs) are unattractive. It is noteworthy that the implementation of local oscillators (LOs) and full CO-Rxs are undesirable. On the other hand, most of the short-reach transceivers usually comprise components such as DML, low bandwidth PIN, VCSEL, and EAM. Besides, DD-based schemes with simplified DSP are the more promising solutions for the short-reach systems.

Form-factor

In general, small form-factors are very essential to the majority of optical transceivers. However, the demanded form-factor by the short-reach applications such as DCNs is even more stringent. This is mainly because the underlying form-factors have significant effects on the port number and density, as well as the rack size to support the ports. Besides, these parameters determine the size of the DCN as a whole and the required cooling system. So, the form factor plays a pivotal role in total energy consumption/usage by the system [5].

Other Challenges of Short-Reach Systems

As aforementioned, short-reach systems demand low-cost components. However, these kinds of components usually offer imperfect results that consequently bring about the initiation of additional transmission impairments that are mainly peculiar to the short-reach systems. For instance, when a DML is directly modulated, a signal chirp will be generated. Besides, components such as trans-impedance amplifier (TIA), EAM, and photodetector, also generate additional nonlinear distortions. The low-pass filtering effect that is owing to the insufficient bandwidth of different components is another typical impairment of the short-reach systems. Besides, the RIN of the laser source and the finite extinction ratios of the EAM degrade the signal to noise ratio (SNR) and, subsequently, the link power budget margins are reduced. Moreover, the equalization of linear transmission impairments such as polarization mode dispersion (PMD) and CD is very challenging using direct detection with non-negative signaling [5], [6], [39].

2.1.2 Datacenter Networks (DCNs)

A datacenter is a physical facility being employed by different organizations for accommodating vital data and applications for the advancement in the IT industry and economy transformation[40]. The modern datacenters cover multiple private and public clouds to the network edge through mobile devices and embedded computing.

2.1.2.1 Types of DCNs

There are different DCNs and service models that are currently available. Their grouping depends on several factors such as the ownership (i.e. owned either by one or more organizations), fitness into the topology of other datacenters, adopted technologies for storage and computing, and related energy efficiency. Based on these, the DCNs can be broadly grouped

into four main categories as discussed in the following.

Enterprise datacenters

The Enterprise datacenters are usually built, owned, and managed by establishments. So, they are optimized to suit their end-users' requirements. Also, they are usually deployed on the premises of the company. Besides, they can be deployed at a standalone location that is own by the company [41], [42].

Managed services datacenters

These types of datacenters are normally managed on behalf of a company by the third party that can be a service provider. So, the equipment and infrastructure are leased by the company [41].

Colocation datacenters

A colocation (also known simply as "colo") is a datacenter provision in which a company rents space for servers and other computing hardware, within a DCN that belongs to others and located off the company's premises. Usually, the colo offers the cooling, building, physical security, and ensures that the required bandwidth is adequately met. On the other end, the customer (company) provides and manages the components such as storage, servers, and additional hardware that essential for day-to-day operations [41], [43], [44].

Cloud datacenters

These are the off-premises type of DCNs where data and applications are hosted by a cloud services provider. Providers like Microsoft (Azure), Amazon Web Services (AWS), and IBM Cloud usually offer this kind of service. They support different services on energy-efficient and secure facilities that run on 24x7 with the utmost possible speed and reliability [41], [42].

2.1.2.2 Core Components of DCNs

The DCN main components are the storage systems, switches, routers, firewalls, servers, and application delivery controllers for the application delivery assurance. This can be achieved by the deployment of firewalls, as well as intrusion protection. The DCN infrastructure can be grouped as follows [41]:

Network infrastructure

The network infrastructure helps in the connection of (physical and virtualized) servers, storage, data-center services, and external connectivity to the end-user locations [41].

Storage infrastructure

The storage systems are employed to hold the huge amount of the network data which is an important asset in the Internet of Things (IoT) [41].

Computing resources

The supported applications by the servers are the engines of the DCNs. The servers offer different services such as processing, local storage, memory, and network connectivity that helps in driving the applications [41].

2.1.2.3 Standards for DCNs Infrastructure

In the DCN design and data center infrastructure, the most extensively implemented standard is the ANSI/TIA-942. This comprises standards for the ANSI/TIA-942-ready certification. The certification ensures adequate compliance with one of four classes of datacenter tiers. The tiers are rated based on the levels of fault tolerance and redundancy [41], [45].

Tier 1: Basic site infrastructure

A Tier 1 datacenter presents limited protection against physical activities, so it is susceptible to disruptions from planned and unplanned events. This can be attributed to the offered non-redundant (N) components and distribution paths. It has to be shutdown completely to perform preventive maintenance. Its typical availability and annual downtime are 99.671% and 28.8 hours, respectively [41], [45].

Tier 2: Redundant-capacity component site infrastructure

Unlike Tier 1, the Tier 2 datacenter gives enhanced protection against physical events and it is less susceptible to disruption. Also, it supports redundant-capacity components (N +1). Moreover, like Tier 1, it has a single, non-redundant distribution path. The power path and some parts maintenance demand a processing shutdown. Its typical availability and annual downtime are 99.741% and 22.0 hours, respectively [41], [45].

Tier 3: Concurrently maintainable site infrastructure

The Tier 3 datacenter can offer considerable protection against almost all physical events. This can be as a result of the provided redundant-capacity components (N +1), as well as multiple independent distribution paths that enable the load and maintenance to be concurrently supported. Its typical availability and annual downtime are 99.982% and 1.6 hours, respectively [41], [45].

Tier 4: Fault-tolerant site infrastructure

A datacenter with fault-tolerant infrastructure offers comparatively the highest levels of redundancy and fault tolerance. It offers standard maintenance and fault rectification on the network without causing downtime. Its typical availability and annual downtime are 99.995% and 0.4 hour, respectively [41], [45].

2.1.2.4 Requirement and Challenges

In this subsection, we present a comprehensive discussion on the DCN requirements and the associated challenges.

Resilience

Network resilience is one of the main concerns in the DCNs. For example, optical interconnects that employ centralized architectures in which a single ultra-high capacity optical switch is supporting a significant amount of servers are highly susceptible to single-point-of-failure issues. Consequently, robust architectures are required to address the issues [46].

Energy consumption

The required energy for an effective operation usually results in higher operational expendi-

ture (OPEX) costs. It has been observed that in every five years, the energy expenditures of running a typical DCN doubles [40]. Consequently, substantially energy-efficient interconnections are required for sustainable higher network traffic [46].

Traffic

It has been observed that the majority of network traffic processing is within the DCNs (intra-DCNs). This is mainly due to a large amount of hosted applications that are based on parallel programming frameworks. This set-up demands significant interaction among the distributed storage and processing nodes for huge data management. DCN operators have been adopting 100 Gb/s Ethernet and beyond to meet the network demands [46].

Scalability

One of the major benefits of the existing DCNs is that they can efficiently scale to a fat-tree topology that is capable of interconnecting racks that are hosting thousands of servers. In contrast, the majority of optical interconnects are based on centralized architectures that causes significant scalability limitations. Consequently, the means of achieving scalable optical interconnect schemes that are capable of hosting a huge number of servers in the DCNs is of utmost importance to the operators [46].

Latency

Based on the associated supercomputing, as well as other delay-sensitive cloud applications/services, the DCNs demand more stringent latency than the long-haul systems [46], [47]. For short-reach systems, the main element that incurs significant latency is the forward error correction (FEC). Based on this, complicated soft-decision-FEC (SD-FEC) with iterative decoding methods is not usually considered as an effective option. So, either a standard hard-decision-FEC (HD-FEC) or other innovative low-latency codes are more applicable to the short-reach systems [5].

2.2 Towards Self-Coherent (SCOH) Transceiver Architecture

There are several transceiver architectures that can be employed to address the requirements in the optical transmission systems and consequently enhance the performance regarding the reach and the SE. The need for the SCOH system for short- and medium-reach applications such as DCN are comprehensively discussed here. Moreover, concerning the COH detection and the IM-DD, the relative benefits and classifications of the SCOH schemes are presented.

2.2.1 Full Coherent Optical System

The COH system can effectively detect the full optical field. Also, as regards SE, COH optical transmission techniques are viable solutions that can offer optimal performance. This is as a result of the concurrent support for information encoding in both quadratures and polarizations of the electric field [48], [49]. Furthermore, CO-Rxs can be broadly based on two configurations which are intradyne/homodyne and heterodyne systems. As illustrated in Fig.2.2, in the former (i.e. Fig. 2.2(a)), a pair of the balanced detector is required per polarization, while for the latter (i.e. Fig. 2.2(b) and (c)), a detector whose bandwidth is twice that of the former, per polarization is usually employed [50], [51], [52], [53]. It is noteworthy

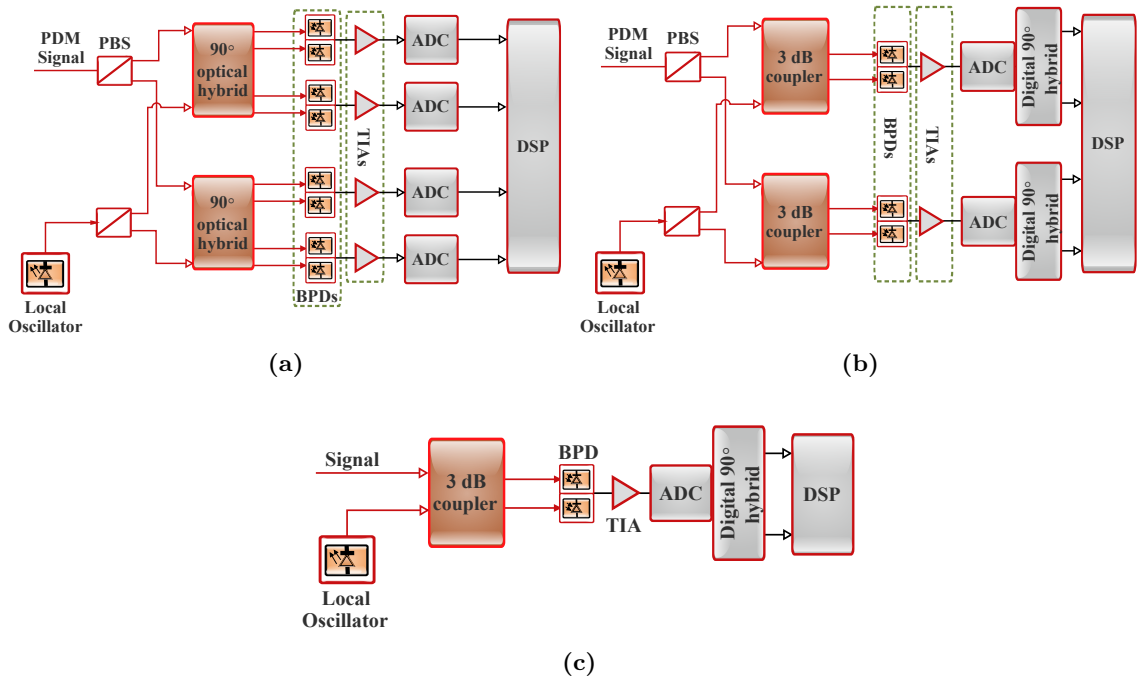

Figure 2.2: Digital coherent receivers (Rxs) configurations: (a) polarization and phase-diverse intradyne/homodyne detection, (b) polarization- and phase-diverse heterodyne detection, and (c) phase-diversity heterodyne detection. (adapted from [56]–[59][52])

that, the polarization-diverse intradyne scheme is mainly adopted in the existing CO-Rxs [49], [51]. In general, full CO-Rxs are viable solutions for medium-to-long-reach applications, the main concerns about their implementation for the short-reach links are the associated high cost and complexity. For instance, a full CO-Rx implementation (i.e. Fig. 2.2(a)) is usually based on components such as a LO laser, optical hybrids, either polarization diversity system or an optical polarization tracking setup, and balanced photodetectors (BPDs) (i.e. four pairs) to suppress the signal-to-signal beating noise (SSBN) at relatively lower LO powers. Detailed information on the DSP for long-haul COH systems is available in [54], [55]. In spite of the fact that a full CO-Rx might be an effective long-term scheme, currently, it is not a cost-efficient solution for cost-sensitive and short-reach link applications like DCNs [49], [50], [52], [53]. Simplified SCOH optical schemes have been presented to address the associated challenges of the full COH system implementation.

2.2.2 SCOH Optical System

The short-reach links have been gaining considerable attention in different application areas such as access, 5G fronthaul, and inter-DCN communications [48], [49]. In an effort to offer economical solutions for supporting the short-reach links and the associated applications, several simpler transmission schemes that are based on the DD system have been presented [48], [49]. One of such simplified solution is to employ DD on just one side of the optical spectrum [50]. This implementation gives rise to a SSB power detection technique. The SSB transmission scheme not only has the ability to address the frequency selective power fading but also helps in doubling the SE compared with the double sideband (DSB) modulation [60],

[61], [62]. In the subsequent sections 2.2.3 and 2.2.4, we comprehensively discuss the SCOH system classification and their relative advantages over IM-DD and traditional COH systems.

2.2.3 SCOH System Classification

This subsection presents a comprehensive analysis of the existing SCOH based schemes. Also, the schemes can be grouped in accordance with the Rx structure. Mainly, they can be classified as either being based on the single-ended photodetector or a balanced Rx scheme.

2.2.3.1 Direct-Detection Based Single-Ended Photodetector

In a conventional DD scheme, intensity modulation (IM) is normally employed at the transmitter (Tx). Also, the modulator is usually driven through a real-valued radio frequency (RF) signal. This results in a Hermitian symmetric optical spectrum. However, it should be noted that half of the optical SE is being wasted by this scheme. Besides, another notable drawback of DD scheme is the associated CD-induced power fading that eventually gives rise to the transmission distance limitation [2]. The CD related challenges in the DD scheme can be attended to by exploiting means that prevented the reception of the two interfering sidebands. In this context, an SSB field modulation is a promising candidate that can easily be employed in the DD scheme [63]. Single-ended photodetector based DD structures such as offset SSB, vestigial single sideband (VSSB), and block-wise phase switching direct-detection (BPS-DD) schemes are good implementation examples of this classification. A piece of comprehensive information on the SSB signal generation and associated concepts are given in section 2.3.

As aforementioned, an electrical bandwidth is a determining factor for the transponder cost, so, to further increase the electrical spectral efficiency (ESE), it is very important to exploit the DSB modulation scheme. It is noteworthy that at a moderate distance, the conventional DSB scheme is prone to dispersion-induced fading. To address the issue, the BPS-DD concept has been presented [64], [65]. In this scheme, for two comparable consecutive signal blocks, either the main carrier or subcarriers phase is switched by 90° or 180° at the Tx, while phase diversity is employed at the Rx to recover the DSB signal [2], [65].

In addition, there are three different schemes that can be employed in the block-wise phase switching (BPS) implementation. An instance of this is a carrier phase switching (CPS). In the CPS, the phase of the main carrier is switched by 90° for the two consecutive blocks while the subcarriers are unchanged. Also, another implementation is the signal subcarrier phase switching (SCPS). The SCPS entails switching the phase of signal subcarrier by 90° while the phase of the main carrier is unchanged. Likewise, signal set phase reversal (SPR) is another form of BPS implementation. In the SPR, the phase of lower sideband is switched by 180° while that of the upper sideband is left unchanged [2], [65].

2.2.3.2 Direct-Detection Based Balanced Receiver

Balanced Rx based DD offers benefits such as the feasibility of recovering phase diverse signals and instinctive elimination of SSBN by means of BPD. This helps in addressing the associated high computational complexity of the iterative SSBN cancellation algorithm. Conceptually, the traditional SCOH scheme that supports coherent-like detection without LO normally co-propagates the carrier in conjunction with the signal at the Tx. Then, at Rx, the signal and the carrier are separated again. The resulting signal is separated into two paths that are used

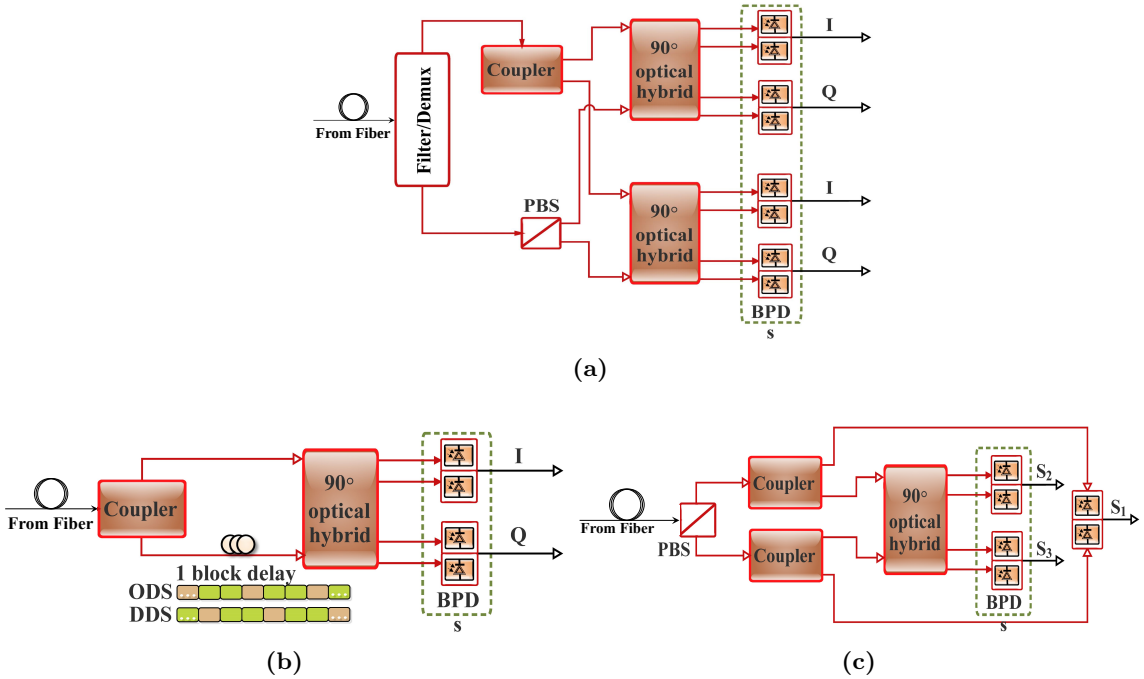

Figure 2.3: Balanced Rxs based direct detection structures: (a) polarization division multiplexing direct-detection (PDM-DD); (b) signal carrier interleaved direct-detection (SCI-DD); (c) Stokes vector direct-detection (SV-DD). PBS: Polarization beam splitter; BPD: Balanced photo-detector; DDS: Delayed data stream; ODS: Original data stream (adapted from [2], [66], [67], [68])

to drive the two inputs of the standard CO-Rx [2], [69]. For instance, as illustrated in Fig. 2.3(a), the PDM-DD, employs a narrow bandwidth low pass filter to separate the signal and the carrier in the frequency domain [2], [70]. It is worth noting that this process limits the SE of DD-based systems. Also, the performance of the optical filter is another limitation that deserves considerable attention [70]. Besides, it helps in accommodating the laser wavelength drift as well as the filter bandwidth [2].

To address the associated issue of the PDM-DD scheme, a SCI-DD has been presented. The SCI-DD scheme separates the signal and the carrier in the time domain by assigning the main carrier and the signals to different time slots. As illustrated in Fig. 2.3(b), one carrier block is appended to two consecutive signal blocks at the Tx. At the Rx, the stream is separated into two different paths and the lower path is delayed by one block length. This helps in ensuring that the signal and the carrier from different path beat effectively with each other at the Rx [2], [71] However, one-third of the SE is being sacrificed by the SCI-DD [2].

In an effort to further enhance the system capacity per wavelength, an SV-DD scheme has been presented. This scheme is capable of realizing a 100% SE with regard to the COH detection of single-polarization modulation [2]. As depicted in Fig. 2.3(c), in the SV-DD scheme, the Tx locates the signal and the carrier at two orthogonal polarizations using a polarization beam combiner (PBC). With the help of a DSP based 3x3 Stokes vector rotation, the desired signal can be well-retrieved with the full phase diversity [2], [72]. Moreover, in the SV-DD scheme, just one-polarization modulation is required, resulting in a simpler Tx design compared with COH detection.

2.2.4 Relative Advantages of SCOH Schemes

Compared to the COH detection, the relative benefits of the SCOH are as follows [66]:

- There is a significant simplification in the optical hardware, mainly for the optical front-end hardware of the Rx.
- Besides, dual-polarization (DP) Rx is highly important in the COH system to enable 2 x 2 multiple input multiple output (MIMO) polarization recovery. On the other hand, single polarization is one of the suitable options in the SCOH for the polarization alignment for the signal and the carrier at the Tx.
- The required DSP by the Rx is simplified. For instance, there is no requirement for the execution of sophisticated carrier recovery since LO is not required.
- SCOH can be implemented un-cooled while this is really challenging in the COH system as there is a need for tight control of the laser wavelength at both Tx and Rx.
- As an ultimate consequence of the previous itemized advantages, the SCOH based scheme provides a cost-effective solution compared with the full COH scheme for short- and medium-reach applications.

Next, compared to IM-DD, the following benefits can be offered by the SCOH [2], [66]:

- The received signal in the SCOH is a linear replica of the transmitted one based on the linear channel that facilitates optical field modulation and detection.
- The co-propagated carrier facilitates phase diversity realization and helps remarkably in increasing the Rx sensitivity.
- Since the carrier and the signal are generated through the same laser source, the system's vulnerability to the laser phase noise is inherently mitigated in the SCOH system.
- One of the main problems of an IM-DD system is the CD induced power fading that cannot be recovered by means of DSP. Consequently, a single-carrier IM-DD system is susceptible to ISI, and this results in the transmission distance (<10 km) limitation. This issue can be addressed with the implementation of the SCOH system in which the DSP can be exploited for the channel estimation and impairment compensation.
- SCOH offers 2-D DD Rx that helps in expanding the optical SE. Also, the RF bandwidth utilization ratio at the Rx can reach up to 100% with the employment of the DSB modulation (i.e. SV-DD). This helps in relaxing the Rx bandwidth requirement.
- The supported optical field modulation in the SCOH system facilitates the dense wavelength division multiplexing (DWDM) and even super-channel implementation. This can significantly help in the full utilization of the optical spectrum.

In general, a SCOH system attempts to offer a good trade-off between COH and IM-DD schemes.

2.3 SCOH Transceiver Architectures

This section presents different potential transceiver structures for the SCOH system. The structures are compared to show their respective advantages and disadvantages. Also, apart from the technical challenges that are discussed, potential solutions are proffered for addressing the related issues of the transceiver structures. Moreover, the SSB signal generation techniques at the Tx and the associated SSBN mitigation schemes at the Rx are considered.

2.3.1 Carrier and Single Sideband (SSB) Signal Generation Techniques

In this section, different means of generating SSB signals are discussed regarding the signal filtering methods and carrier insertion techniques. It should be noted that these SSB generation schemes could either be based on optical or digital filtering [73]–[76]. In this context, the four extensively employed methods for generating optical SSB signals are considered in the following subsections. They are classified into two fundamental groups based on the adopted generation approach which can be a bias-induced or carrier-assisted scheme.

2.3.1.1 Bias-Induced Carrier Generation Scheme

Bias induced carrier generation scheme is based on the manner in which the IQ modulator (IQM) or the dual-drive Mach-Zehnder modulator (DDMZM) is biased in order to generate the carrier. This subsection presents the associated schemes that can be employed based on the bias point of the component.

SSB Subcarrier Modulation with IQ Modulator Approach

The first approach is based on the employment of an optical SSB filter to remove one of the two sidebands of the DSB signal at the Tx end [76]. In this scheme, both SSB Nyquist baseband signals are up-converted to a subcarrier frequency (f_{sc}) of $B/2$ by multiplexing $exp(j2\pi(B/2)t)$, where B is the bandwidth of the signal. Instead of the null-point, the IQM can be biased either above or below the null-point for an optical carrier to be induced. So, an intensity modulator and an optical filter can be used for generating an optical SSB signal as shown in Fig. 2.4(a). Moreover, the SSB modulation has been implemented in some OFDM based SCOH schemes such as the offset-SSB OFDM system. It should be noted that the frequency gap being created between the carrier and the signal is in an effort to address the associated 2nd order SSBN. Although this method is the simplest solution, it requires a sharp optical filter for removing one of the two sidebands of the DSB signal. So, apart from the extra expense that has to be incurred on the optical filter, when the spectrum gap between the SSB signal and carrier is narrow, the sideband that is meant to be eliminated will present some residuals, owing to the optical filter non-ideal characteristics [73], [75], [76]. Furthermore, since the spectral gap bandwidth is the same as that of the signal, half of the ESE is being sacrificed in the process [71], [76]–[78].

SSB Subcarrier Modulation with DDMZM Approach

Based on the associated cost and the required high roll-off factor of the optical filter, SSB signal generation based on complex modulation with a pair of Hilbert transform signals is more desirable. Fig. 2.4(b) depicts an optical SSB signal generation with a DDMZM-based approach. In this, a digital SSB filter that depends on the Hilbert transformation is implemented

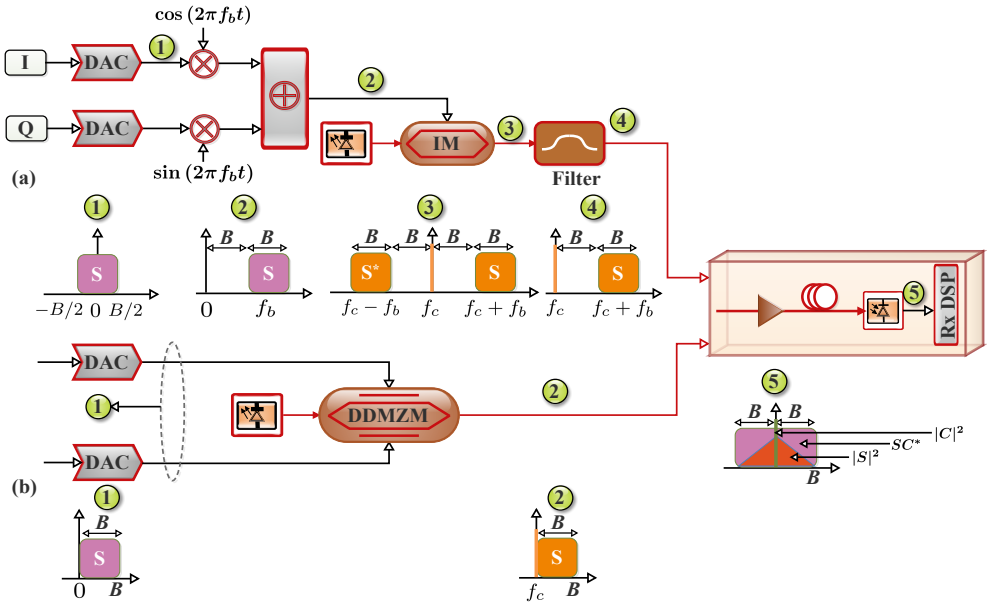

Figure 2.4: Bias-induced carrier generation scheme based on (a) an electrical I/Q mixer with intensity modulation (IM) and optical filter and (b) with a DDMZM. f_b : electrical center frequency of the transmitted signal; f_c : frequency of the Tx laser; $|S|^2$: signal-signal beating; SC^* : signal-carrier beating; $|C|^2$: carrier-carrier beating (adapted from [66], [73]–[76]).

at the Tx. Consequently, the two driving signals of the DDMZM are a pair of Hilbert signals with a phase difference of $\pi/2$ [75], [76] [79]. For instance, in the IM-DD-based SSB-OFDM scheme, after the inverse fast Fourier transform (IFFT), the data and their corresponding conjugates are converted to real-valued signals. Also, the resulting electrical signal and its Hilbert transform are sent to the two arms of a quadrature-biased DDMZM which results in a single sideband orthogonal frequency division multiplexing (SSB-OFDM) [77]. However, it should be noted that as half of the subcarriers are employed as the data subcarrier conjugates, the required electrical bandwidth is 2B, where B denotes the transmission (i.e. output optical signal) bandwidth. Based on this, double of the transmitted optical bandwidth is the required electrical bandwidth. This is as a result of the real-valued OFDM signal that is required for an IM. Therefore, half of the electrical bandwidth which comprises the OFDM generator's DSP processor and the DAC bandwidths are not exploited for data transmission and are being wasted.

2.3.1.2 Carrier-Assisted Generation Scheme

The carrier assisted generation scheme depends on whether the carrier tone to be appended to the signal spectrum is generated digitally or optically.

Optical Carrier-Assisted SSB Approach

An optical IQM driven by a pair of baseband signals can be employed for the SSB signal generation as illustrated in Fig. 2.5(a). Besides, contrary to the implementations illustrated in Fig. 2.4(a) where the IM can be biased either above or below the null-point, in the optical carrier-assisted SSB approach, it is biased at the null point. This helps in the optical

carrier suppression [75]. So, in this approach, a separate optical tone can be appended to the signal spectrum at $-B/2$ or $+B/2$ frequency. It should be noted that this implementation demands an optical frequency comb generation or an extra laser for generating the optical tone. However, this can bring an increase in the cost and hardware complexity regarding the system implementation compared with methods in Fig. 2.4(b) and Fig. 2.5(b) [76].

Virtual Carrier-Assisted SSB Approach

Another promising and viable approach of generating an SSB signal is based on appending

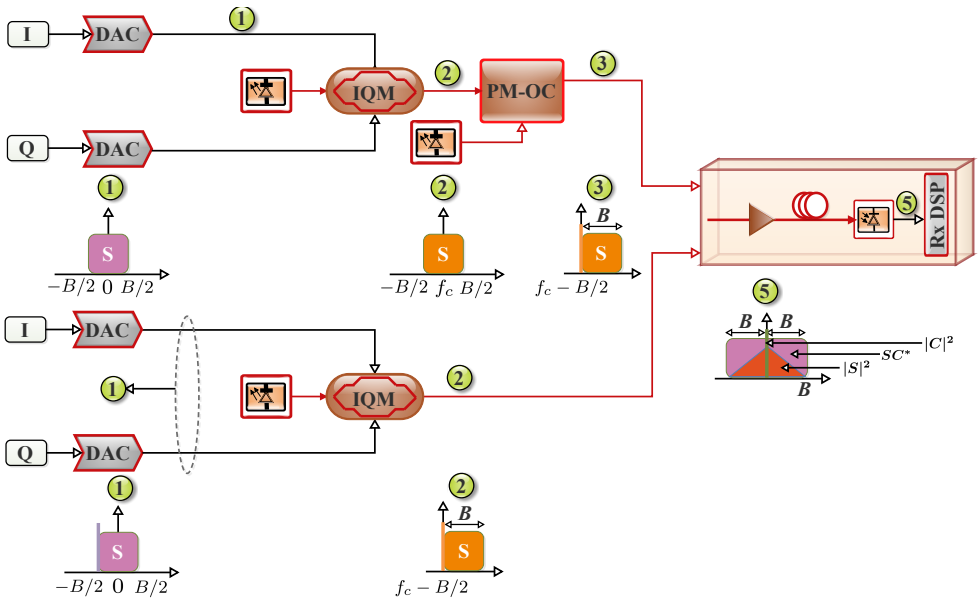

Figure 2.5: Carrier-assisted generation scheme based on (a) an optical IQ modulator (IQM) with appended optical tone at the Tx and (b) an optical IQM with appended digital tone in the DSP. f_b : electrical center frequency of the transmitted signal; f_c : frequency of the Tx laser; $|S|^2$: signal-signal beating; SC^* : signal-carrier beating; $|C|^2$: carrier-carrier beating (adapted from [66], [73]–[76]).

and co-propagating a digital RF tone that serves as a virtual carrier in conjunction with the signal at the Tx [73], [76] [80]. Like the previously discussed scheme, this approach employs one IQM and two DACs. Besides, as illustrated in Fig. 2.5(b), to suppress the optical carrier, the IQM is biased at the null-point like the approach in Fig. 2.5(a). The configuration has been employed for improving the ESE of an OFDM system. For instance, ESE of the offset-SSB OFDM can be enhanced with the implementation of a linear field-modulated and DD-based VSSB-OFDM [71]. In this scheme, an RF tone is inserted at the left-most OFDM subcarrier and it is then transformed along with the data to a complex signal by means of an IFFT. The real and imaginary parts of the signal are subsequently employed for driving the two arms of an optical IQM that has been biased at the null point. Based on the modulator bias point, the initial optical carrier has been suppressed. Therefore, the inserted RF tone presents a new optical carrier. The optical carrier is placed at the left edge of the subsequent signal spectrum [2], [77].

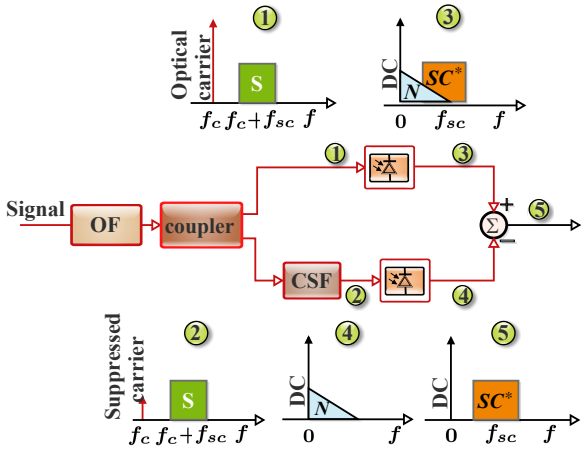

Figure 2.6: SSBN cancellation Rx. OF : optical filter, CSF : carrier suppression filter, N : signal-signal beat noise, SC^*: signal-carrier beating, S : sideband signal

2.3.2 Optical Signal to Signal Beating Noise (SSBN) Mitigation

As aforementioned, the DD transceivers performance is severely degraded by the SSBN penalty that is owing to the square-law photodetection. As illustrated in Fig. 2.6, the SSBN mitigation schemes are majorly based on using an optical amplified spontaneous emission (ASE) filter for removing the dominating noise. Then, the received signal can be split into two branches through a 1x2 optical coupler. One section (the upper branch) is fed directly to the photodetector for generating both the SSBN and desired data sideband. Likewise, in the lower branch, a carrier suppression filter (CSF) can be employed to suppress the optical carrier which brings about just the SSBN after the photodetector. Therefore, the outputs of the two branches can be subtracted to achieve the desired signal. It should be noted that apart from the ability of the linearization schemes to remove the SSBN, they are also capable of alleviating the beat noise power effect. This subsequently results in an enhanced Rx sensitivity [58], [81]. In addition, the optical transmission systems for short-to-medium-reach applications can extend from quite a few tens to a small number of hundred kilometers. Consequently, dispersion compensation is highly imperative in such links [82]. Also, it has been observed that digital compensation of the fiber link dispersion is highly desirable due to the associated cost and complexity motives. Unlike the optical compensation scheme such as a dispersion compensating fiber (DCF), the digital compensation scheme is known as an electronic dispersion compensation (EDC) [83] [83]–[86].

In addition, effective linearization schemes can be employed for performing linear optical effects (dispersion) compensation at the Rx. This can offer comparable performance to the systems with pre-compensation [49]. Also, based on the current development of digital linearization techniques, it is possible to prevent the nonlinear SSBN distortion or compensate for it partially [1]. In the following subsection, the SSBN mitigation concepts, focusing on the performance of transmitter electronic dispersion compensation (Tx-EDC) and receiver electronic dispersion compensation (Rx-EDC) systems are considered. In this context, their performance in conjunction with different Rx-based digital linearization methods is discussed.

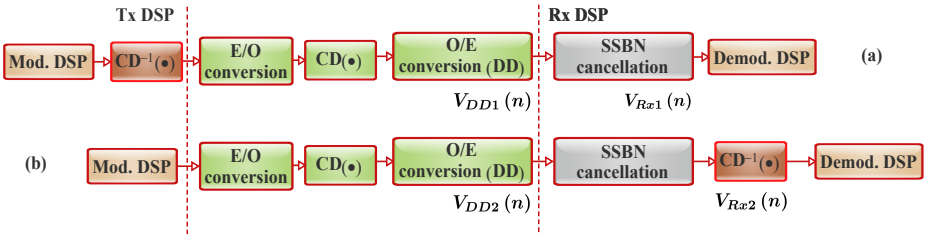

Figure 2.7: Direct-detection scheme with (a) Tx-EDC and (b) Rx-EDC, together with SSBN cancellation (adapted from [1]).

2.3.3 Electronic Dispersion Compensation (EDC) and SSBN Cancellation

The performance of the Tx-EDC and Rx-EDC systems in conjunction with linearization methods can be analyzed by considering Fig. 2.7. The Tx-EDC implementation is depicted in Fig. 2.7(a) while that of the Rx-EDC system is illustrated in Fig. 2.7(b). In the Tx-EDC scheme, the SSB signal $E_0(n)$ is generated at the Tx and modulation DSP is implemented. Then, for CD compensation, the Tx-EDC, H_{CD}^{-1} , is accomplished via signal pre-distortion [1], [87]. The optical carrier, $E_{carrier}$, is subsequently inserted by means of an IQM in the process of electrical to optical (E/O) conversion. Consequently, the normalized DSB signal, $V_{DDi}(n)$, after the square-law detection for the Tx-EDC and Rx-EDC systems, can be expressed respectively as [1],

$$\begin{aligned} V_{DD1}(n) &= |H_{CD}\big(E_{carrier} + H_{CD}^{-1}(E_o(n))\big)|^2 \\ &= E_{carrier}^2 + 2\Re[E_{carrier} \cdot E_o(n)] + |E_o(n)|^2 \end{aligned} \tag{2.1}$$

$$V_{DD1}(n) = E_{carrier}^2 + 2\Re[E_{carrier} \cdot H_{CD}(E_o(n))] + |H_{CD}(E_o(n))|^2 \tag{2.2}$$

where the first and second terms in the right-hand side of Eq. 2.1 represents the DC and the desired carrier-signal beating products, respectively, and the third term denotes the SSBN. A close comparison between Eq. 2.1 and Eq. 2.2 reveals that the second and the third terms of Eq. 2.2 are the products of the beating between the dispersed signal with the optical carrier and with itself, respectively. It is noteworthy that the implementation of the Rx-EDC scheme without linearizing the Rx will result in the inability of the Rx-EDC scheme to recover the undispersed signal accurately. This limitation will be due to the frequency-dependent phase rotation of the SSBN terms, $H_{CD}^{-1}(|H_{CD}(E_0(n))|^2)$, which is owing to the dispersion. Based on this, the Rx-EDC performance will be hindered considerably compared with that of the Tx-EDC scheme. Moreover, supposing that the third term of both Eq. 2.1 and Eq. 2.2 can be removed entirely with the implementation of the SSBN compensation scheme, then, the received signal, $V_{Rxi}(n)$, prior to the demodulation DSP block, for the Tx-EDC and the Rx-EDC systems, can be defined respectively as [1]

$$V_{DD1}(n) \approx E_{carrier}^2 + 2\Re[E_{carrier} \cdot E_o(n)] \tag{2.3}$$

$$\begin{aligned} V_{DD1}(n) &\approx H_{CD}^{-1}(E_{carrier}^2 + 2\Re[E_{carrier} \cdot H_{CD}(E_0(n))]) \\ &\approx E_{carrier}^2 + 2\Re[E_{carrier} \cdot E_o(n)] \end{aligned} \tag{2.4}$$

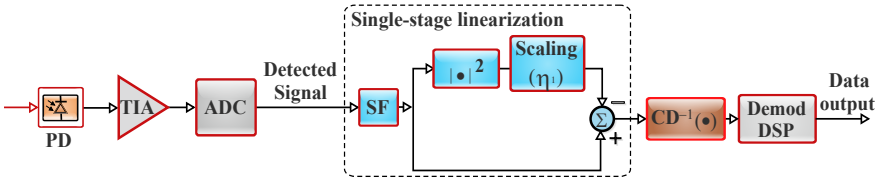

Figure 2.8: Single-stage linearization filter. SF: Sideband filter; $\eta(\bullet)$: Scaling parameter that controls the compensation gain (adapted from [58], [51], [1], [88],[61], [74],[89]–[91].

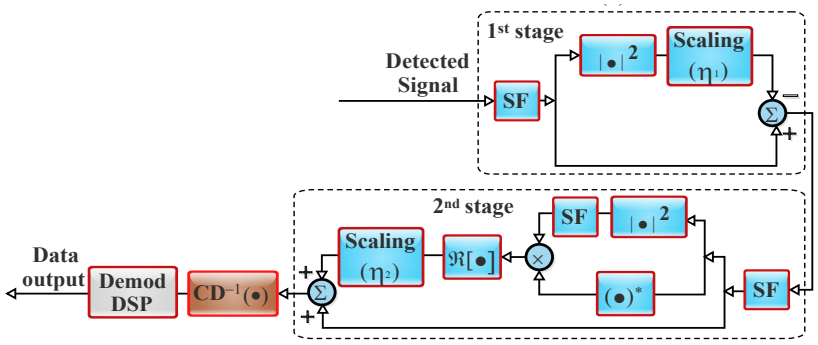

Figure 2.9: Two-stage linearization filter. SF: Sideband filter; $\eta(\bullet)$: Scaling parameter that controls the compensation gain (adapted from [58], [51], [1],[61], [88],[74], [89]–[91]).

The similarity between Eq. 2.3 and Eq. 2.4 implies that the Rx-EDC can realize comparable performance to that of Tx-EDC on condition that the beating interference term is well-suppressed. In the following subsections, we discuss a number of Rx-based digital linearization techniques and the associated interference cancellation (IC) schemes.

2.3.3.1 Single-Stage Linearization Filter Approach

The Rx DSP configuration that is based on a single-stage linearization filter (SSLF) and Rx-EDC is illustrated in Fig. 2.8. In the SSLF block, a digital SSB signal is acquired from the detected electrical DSB signal by means of a sideband filter (SF) [1]. Also, in this scheme, the SSBN terms are treated as a perturbation to the signal [58]. Then, the SSBN terms waveform approximation is estimated in accordance with the SSB signal and subtracted from the SSB signal that has been filtered. This process helps in partial compensation of the SSBN [92]. So, the performance difference between Tx-EDC and Rx-EDC can be reduced with the implementation. Nevertheless, since the SSBN terms estimation is in line with the received distorted signal, extra beating interference is being presented by the scheme. This considerably limits the compensation performance [1].

2.3.3.2 Two-Stage Linearization Filter Approach

The SSLF approach can be improved by adopting a two-stage linearization filter and Rx-EDC in the Rx DSP design as depicted in Fig. 2.9. The main limitation of the SSLF approach is the introduced beating interference that is primarily the signal-SSBN beating products. This issue can be addressed by employing another linearization stage in addition to a stage being employed in the SSLF approach. This will facilitate the elimination of the unwanted beating

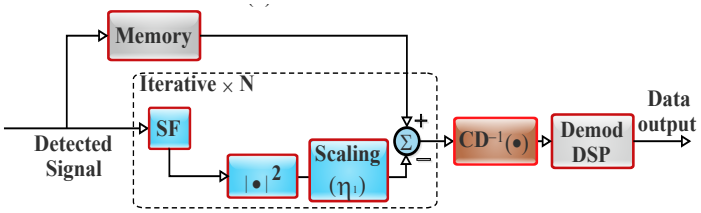

Figure 2.10: Iterative linearization filter.SF: Sideband filter; $\eta(\bullet)$: Scaling parameter that controls the compensation gain (adapted from [58], [51], [1], [88],[61],[76],[89]–[91]).

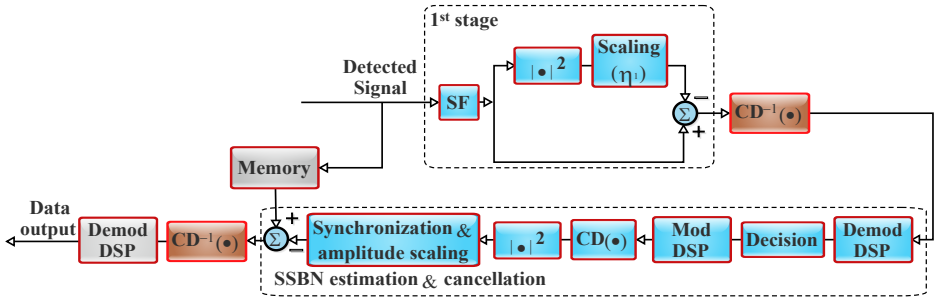

Figure 2.11: SSBN estimation and cancellation. SF: Sideband filter; $\eta(\bullet)$: Scaling parameter that controls the compensation gain (adapted from [58], [51],[1], [88][61],[74], [89]–[91]).

interference that emanates from the first linearization stage [93]. Therefore, the second-stage helps further in improving the compensation gain. Furthermore, it can help the Rx-EDC in having an enhanced bit error rate (BER) performance and transmission performance that is comparable to that of the Tx-EDC.

2.3.3.3 Iterative Linearization Filter Approach

Another viable solution for improving the Rx DSP performance is the iterative linearization filter and Rx-EDC implementation. The iterative linearization filter scheme can further help in enhancing the SSLF and two-stage linearization filter performance. In this approach, the detected signal waveform is initially stored in the memory as illustrated in Fig. 2.10. Subsequently, the SSBN is determined according to the sideband-filtered signal. Then, the resulting signal can be subtracted from the stored signal waveform so as to alleviate the SSBN [89], [90]. The procedure will then be iterated several times with the intention of accomplishing a maximum compensation gain. Besides significant latency that can be incurred, the associated iterations can considerably increase the DSP power consumption [94].

2.3.3.4 SSBN Estimation and Cancellation Approach

The Rx DSP that comprises the SSBN estimation and cancellation technique in addition to the Rx-EDC is depicted in Fig. 2.11. Unlike the iterative SSBN cancellation scheme, the need for multiple symbol decision based SSBN reconstruction procedures that demand multiple IFFT/FFT pairs is prevented. Also, the scheme entails having two replicas of the detected signal. A copy is stored in the memory while the other is sent to an SSLF that offers partial elimination of the SSBN terms. Then, a non-iterative SSBN estimation and cancellation is executed to construct an approximation of the SSBN. Subsequently, the resulting signal

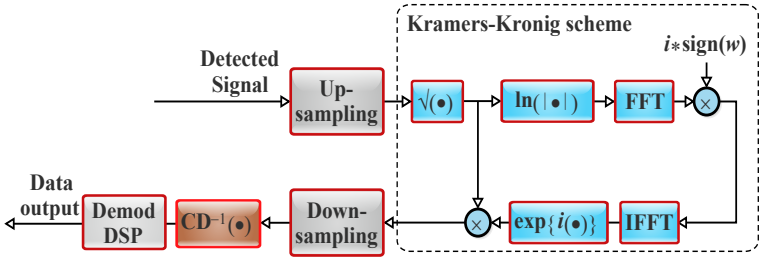

Figure 2.12: Kramers-Kronig algorithm

is subtracted from the signal waveform that is being stored in the memory [1], [91]. It is noteworthy that no additional unwanted beating product is presented by the scheme, as usual in the case of the linearization filtering schemes. Consequently, the SSBN estimation and cancellation scheme presents an improved compensation gain in particular, at the higher OSNR values. Nonetheless, the dependency on the symbol decision accuracy is the main limitation of the SSBN estimation and cancellation. This limitation results in performance degradation at lower OSNR levels [1].

2.3.3.5 Kramers-Kronig Approach

The Rx DSP that exploits the Kramers-Kronig (KK) algorithm and Rx-EDC is shown in Fig. 2.12. Rather than considering SSBN terms as a perturbation that should be eliminated as in the case of other linearization approaches, the KK algorithm reconstructs the optical phase of the transmitted SSB signal based on its detected intensity [58]. This is possible because the KK scheme is based on the minimum phase signal property (comprehensively discussed in chapter 3). To satisfy the minimum-phase condition, an amplitude that is larger (stronger) than that of the signal is demanded by the optical carrier [58], [95]. In this context, the optical phase of a minimum-phase transmitted signal can be digitally reconstructed from the measurement of its optical envelope [49],[96]–[98]. So, with the KK relation, the transmitted signal phase can be linked to its intensity. However, violation of the minimum-phase condition brings about distortions in the recovered phase waveform [62]. Compared to the other concurrent techniques, the KK coherent transceiver exhibits better accuracy in the field recovery.

Open Issues:

SSB methods have been explored to obtain amplitude and phase information using DD. However, they tend to suffer a strong penalty due to SSBN. More recently, a minimum phase signal based KK receiver has been proposed which significantly reduces the impact of SSBN. However, the nonlinear operations in the KK algorithm demand the DSP to be operated much faster than Nyquist sampling rate to accommodate spectral broadening. To reduce the sampling rate, some approximations can be used in-place of nonlinear operations. Nevertheless, those approximations tend to require higher tone powers which result in the receiver sensitivity penalty. Therefore, the need is to address sampling-rate and high tone power requirements of the KK methods!

2.4 Final Remarks

This chapter presents comprehensive tutorials on the main requirements, technologies, architectures, and the associated challenges of different transceiver systems considering short-reach applications. Besides, different advancements in modulation formats, devices, and digital signal processing algorithms capable of facilitating 100 Gb/s and beyond per wavelength have been broadly reviewed. Also, a set of SCOH schemes have been well-reviewed and comprehensively compared. The SCOH schemes are opening up new prospects for ultra-high-capacity transceivers. It presents remarkable advantages beyond the conventional intensity modulation with direct detection while maintaining the simplicity and salient cost-efficiency for short and medium-reach applications. The offered benefits are a result of the exploited advantages of the cost-effective and simplified intensity modulation with direct detection and the high sensitivity and complex modulation format that enabled sophisticated coherent systems.

Moreover, specific related open-ended issues have been presented, and the proffered potential solutions are well-examined. It can be established that based on the promising and significant progress, there is considerable prospect towards high-speed optical transceivers that are capable of fulfilling the current and future requirements. This can be attributed to the fact that the SCOH schemes aim to bridge the performance gaps between the conventional COH and IM-DD schemes.

References

[1] Z. Li, M. S. Erkılınç, K. Shi, *et al.*, "SSBI Mitigation and the Kramers–Kronig Scheme in Single-Sideband Direct-Detection Transmission With Receiver-Based Electronic Dispersion Compensation," *IEEE/OSA Journal of Lightwave Technology*, vol. 35, no. 10, pp. 1887–1893, 2017.

[2] D. Che, X. Chen, A. Li, *et al.*, "Optical Direct Detection for 100G Short Reach Applications," *Asia Communications and Photonics Conference (ACP)*, pp. 1–3, 2014.

[3] X. Pang, O. Ozolins, R. Lin, *et al.*, "200 Gbps/Lane IM/DD Technologies for Short Reach Optical Interconnects," *IEEE/OSA Journal of Lightwave Technology*, vol. 38, no. 2, pp. 492–503, 2020.

[4] I. Alimi, R. Patel, N. Silva, *et al.*, "A Review of Self-Coherent Optical Transceivers: Fundamental Issues, Recent Advances, and Research Directions," *Applied Sciences*, vol. 11, no. 16, 2021.

[5] K. Zhong, X. Zhou, J. Huo, *et al.*, "Digital Signal Processing for Short-Reach Optical Communications: A Review of Current Technologies and Future Trends," *IEEE/OSA Journal of Lightwave Technology*, vol. 36, no. 2, pp. 377–400, 2018.

[6] M. Chagnon, "Optical Communications for Short Reach," *IEEE/OSA Journal of Lightwave Technology*, vol. 37, no. 8, pp. 1779–1797, 2019.

[7] K. Zhong, X. Zhou, Y. Wang, *et al.*, "Recent Advances in Short Reach Systems," *Optical Fiber Communications Conference and Exhibition (OFC)*, pp. 1–3, 2017.

[8] K. Zhong, X. Zhou, Y. Wang, *et al.*, "Recent Advances for High Speed Data Center Inter-Connects," *Asia Communications and Photonics Conference (ACP)*, pp. 1–3, 2016.

[9] J. Wei, Q. Cheng, R. V. Penty, *et al.*, "400 Gigabit Ethernet Using Advanced Modulation Formats: Performance, Complexity, and Power Dissipation," *IEEE Communications Magazine*, vol. 53, no. 2, pp. 182–189, 2015.

[10] J. C. Rasmussen, T. Takahara, T. Tanaka, *et al.*, "Digital Signal Processing for Short Reach Optical Links," *European Conference on Optical Communication (ECOC)*, pp. 1–3, 2014.

[11] A. F. Shalash and K. K. Parhi, "Multidimensional Carrierless AM/PM Systems for Digital Subscriber Loops," *IEEE Transactions on Communications*, vol. 47, no. 11, pp. 1655–1667, 1999.

[12] L. Sun, J. Du, and Z. He, "Multiband Three-Dimensional Carrierless Amplitude Phase Modulation for Short Reach Optical Communications," *IEEE/OSA Journal of Lightwave Technology*, vol. 34, no. 13, pp. 3103–3109, 2016.

[13] J. Wei, Q. Cheng, R. V. Penty, *et al.*, "400 Gigabit Ethernet Using Advanced Modulation Formats: Performance, Complexity, and Power Dissipation," *IEEE Communications Magazine*, vol. 53, no. 2, pp. 182–189, 2015.

[14] K. Zhong, X. Zhou, Y. Wang, *et al.*, "Recent Advances for High Speed Data Center Inter-Connects," *Asia Communications and Photonics Conference (ACP)*, pp. 1–3, 2016.

[15] K. Zhong, X. Zhou, T. Gui, *et al.*, "Experimental study of PAM-4, CAP-16, and DMT for 100 Gb/s Short Reach Optical Transmission Systems," *Optics Express*, vol. 23, no. 2, pp. 1176–1189, 2015.

[16] J. M. Tang, P. M. Lane, and K. A. Shore, "High-speed Transmission of Adaptively Modulated Optical OFDM Signals Over Multimode Fibers Using Directly Modulated DFBs," *IEEE/OSA Journal of Lightwave Technology*, vol. 24, no. 1, pp. 429–441, 2006.

[17] S. K. Pavan, J. Lavrencik, and S. E. Ralph, "VCSEL-Based PAM-4 Links up to 62 Gbit/s Over OM3, OM4, and WB-MMF: Performance Comparison at 850 nm and 1050 nm," *IEEE/OSA Journal of Lightwave Technology*, vol. 35, no. 9, pp. 1614–1623, 2017.

[18] P. Moser, J. A. Lott, P. Wolf, *et al.*, "Error-free 46 Gbit/s Operation of Oxide-confined 980 nm VCSELs at 85°C," *Electronics Letters*, vol. 50, no. 19, pp. 1369–1371, 2014.

[19] Y. Chang and L. A. Coldren, "Efficient, High-Data-Rate, Tapered Oxide-Aperture Vertical-Cavity Surface-Emitting Lasers," *IEEE Journal of Selected Topics in Quantum Electronics*, vol. 15, no. 3, pp. 704–715, 2009.

[20] T. Lengyel, E. Simpanen, J. S. Gustavsson, *et al.*, "Pre-emphasis Enabled 50 Gbit/s Transmission over 1000 m SMF Using a 1060 nm Single-mode VCSEL," *Electronics Letters*, vol. 54, no. 20, pp. 1186–1187, 2018.

[21] E. Simpanen, J. S. Gustavsson, A. Larsson, *et al.*, "1060 nm Single-Mode VCSEL and Single-Mode Fiber Links for Long-Reach Optical Interconnects," *IEEE/OSA Journal of Lightwave Technology*, vol. 37, no. 13, pp. 2963–2969, 2019.

[22] E. Simpanen, J. S. Gustavsson, E. Haglund, *et al.*, "1060 nm Single-mode Vertical-cavity Surface-emitting Laser Operating at 50 Gbit/s Data Rate," *Electronics Letters*, vol. 53, no. 13, pp. 869–871, 2017.

[23] A. Liu, P. Wolf, J. A. Lott, *et al.*, "Vertical-cavity Surface-emitting Lasers for Data Communication and Sensing," *Photonics Research*, vol. 7, no. 2, pp. 121–136, 2019.

[24] K. Yashiki, N. Suzuki, K. Fukatsu, *et al.*, "1.1-μm-Range High-Speed Tunnel Junction Vertical-Cavity Surface-Emitting Lasers," *IEEE Photonics Technology Letters*, vol. 19, no. 23, pp. 1883–1885, 2007.

[25] N. H. Zhu, Z. Shi, Z. K. Zhang, *et al.*, "Directly Modulated Semiconductor Lasers," *IEEE Journal of Selected Topics in Quantum Electronics*, vol. 24, no. 1, pp. 1–19, 2018.

[26] E. K. Lau, X. Zhao, H.-K. Sung, *et al.*, "Strong Optical Injection-locked Semiconductor Lasers Demonstrating >100-GHz Resonance Frequencies and 80-GHz Intrinsic Bandwidths," *Optics Express*, vol. 16, no. 9, pp. 6609–6618, 2008.

[27] H. Ji, L. Yi, Z. Li, *et al.*, "Field Demonstration of a Real-Time 100-Gb/s PON Based on 10G-Class Optical Devices," *IEEE/OSA Journal of Lightwave Technology*, vol. 35, no. 10, pp. 1914–1921, 2017.

[28] D. Che, F. Yuan, and W. Shieh, "Towards High-order Modulation Using Complex Modulation of Semiconductor Lasers," *Optics Express*, vol. 24, no. 6, pp. 6644–6649, 2016.

[29] L. Xue, L. Yi, H. Ji, *et al.*, "Symmetric 100-Gb/s TWDM-PON in O-Band Based on 10G-Class Optical Devices Enabled by Dispersion-Supported Equalization," *IEEE/OSA Journal of Lightwave Technology*, vol. 36, no. 2, pp. 580–586, 2018.

[30] M. Jacques, A. Samani, D. Patel, *et al.*, "Modulator Material Impact on Chirp, DSP, and Performance in Coherent Digital Links: Comparison of the Lithium Niobate, Indium Phosphide, and Silicon Platforms," *Optics Express*, vol. 26, no. 17, pp. 22 471–22 490, 2018.

[31] C. Wang, M. Zhang, B. Stern, *et al.*, "Nanophotonic Lithium Niobate Electro-optic Modulators," *Optics Express*, vol. 26, no. 2, pp. 1547–1555, 2018.

[32] W. Shi, Y. Xu, H. Sepehrian, *et al.*, "Silicon Photonic Modulators for PAM Transmissions," *Journal of Optics*, vol. 20, no. 8, pp. 1–35, 2018.

[33] D. Patel, A. Samani, V. Veerasubramanian, *et al.*, "Silicon Photonic Segmented Modulator-Based Electro-Optic DAC for 100 Gb/s PAM-4 Generation," *IEEE Photonics Technology Letters*, vol. 27, no. 23, pp. 2433–2436, 2015.

[34] A. Samani, D. Patel, M. Chagnon, *et al.*, "Experimental Parametric Study of 128 Gb/s PAM-4 Transmission System Using a Multi-electrode Silicon Photonic Mach Zehnder Modulator," *Optics Express*, vol. 25, no. 12, pp. 13 252–13 262, 2017.

[35] M. Li, L. Wang, X. Li, *et al.*, "Silicon Intensity Mach-Zehnder Modulator for Single Lane 100 Gb/s Applications," *Photonics Research*, vol. 6, no. 2, pp. 109–116, 2018.

[36] G. Cong, M. Ohno, Y. Maegami, *et al.*, "Silicon Traveling-wave Mach–Zehnder Modulator Under Distributed-bias Driving," *Optics Letters*, vol. 43, no. 3, pp. 403–406, 2018.

[37] T. Kimura, "EML vs DML for Datacenter and Client Side Transceivers," NeoPhotonics, NeoPhotonics Blog, 2015.

[38] K. Hasebe, S. Matsuo, H. Sanjoh, *et al.*, "Directly Frequency Modulated DFB Laser Integrated with EA Modulator for Extended Transmission Reach," *European Conference on Optical Communication (ECOC)*, pp. 1–3, 2010.

[39] C. M. Miller, "Intensity Modulation and Noise Characterization of High-speed Semiconductor Lasers," *IEEE LTS*, vol. 2, no. 2, pp. 44–50, 1991.

[40] M. Dayarathna, Y. Wen, and R. Fan, "Data Center Energy Consumption Modeling: A Survey," *IEEE Communications Surveys Tutorials*, vol. 18, no. 1, pp. 732–794, 2016.

[41] "What is a Data Center," Cisco, White Paper.

[42] Y. Sun, "Recent Advances for High Speed Short Reach Optical Interconnects for Datacom Links," *IEEE CPMT Symposium Japan (ICSJ)*, pp. 63–65, 2017.

[43] S. Watts, "What is "Data Center Colocation"? Data Center Colocation Explained," bmc, bmc blogs, 2018.

[44] M. Rouse, "Manage Colocation Costs to Avoid Billing Surprises," WhatIs.com, e-learning, 2015.

[45] "TIA-942- Data Center Standard Overview," ADC, White Paper: TIA-942, 2006.

[46] C. Kachris, K. Kanonakis, and I. Tomkos, "Optical Interconnection Networks in Data Centers: Recent Trends and Future Challenges," *IEEE Communications Magazine*, vol. 51, no. 9, pp. 39–45, 2013.

[47] L. Ma, W. Su, X. Li, *et al.*, "Heterogeneous Data Backup Against Early Warning Disasters in Geo-distributed Data Center Networks," *IEEE/OSA Journal of Optical Communications and Networking*, vol. 10, no. 4, pp. 376–385, 2018.

[48] N. J. Muga, R. K. Patel, I. Alimi, *et al.*, "Self-coherent Optical Detection for Access and Metro Networks," *International Conference on Transparent Optical Networks (ICTON)*, pp. 1–4, 2019.

[49] A. Mecozzi, C. Antonelli, and M. Shtaif, "Kramers-Kronig Coherent Receiver," *Optica*, vol. 3, no. 11, pp. 1220–1227, 2016.

[50] X. Chen, C. Antonelli, S. Chandrasekhar, *et al.*, "Kramers–Kronig Receivers for 100-km Datacenter Interconnects," *IEEE/OSA Journal of Lightwave Technology*, vol. 36, no. 1, pp. 79–89, 2018.

[51] C. Füllner, M. M. H. Adib, S. Wolf, *et al.*, "Complexity Analysis of the Kramers–Kronig Receiver," *IEEE/OSA Journal of Lightwave Technology*, vol. 37, no. 17, pp. 4295–4307, 2019.

[52] M. S. Faruk, H. Louchet, M. S. Erkilinç, *et al.*, "DSP Algorithms for Recovering Single-carrier Alamouti Coded Signals for PON Applications," *Optics Express*, vol. 24, no. 21, pp. 24 083–24 091, 2016.

[53] N. Nabavi and T. J. Hall, "Symmetric Signal and Local Oscillator Polarization Diverse Coherent Optical Receiver," *Optics Express*, vol. 24, no. 3, pp. 2391–2405, 2016.

[54] S. J. Savory, "Digital Coherent Optical Receivers: Algorithms and Subsystems," *IEEE Journal of Selected Topics in Quantum Electronics*, vol. 16, no. 5, pp. 1164–1179, 2010.

[55] E. Ip, A. P. T. Lau, D. J. F. Barros, *et al.*, "Coherent Detection in Optical Fiber Systems," *Optics Express*, vol. 16, no. 2, pp. 753–791, 2008.

[56] K. Kikuchi, "Fundamentals of Coherent Optical Fiber Communications," *IEEE/OSA Journal of Lightwave Technology*, vol. 34, no. 1, pp. 157–179, 2016.

[57] M. S. Erkılınç, D. Lavery, K. Shi, *et al.*, "Comparison of Low Complexity Coherent Receivers for UDWDM-PONs (λ-to-the-User)," *IEEE/OSA Journal of Lightwave Technology*, vol. 36, no. 16, pp. 3453–3464, 2018.

[58] Z. Li, M. Sezer Erkılınç, K. Shi, *et al.*, "Digital Linearization of Direct-Detection Transceivers for Spectrally Efficient 100 Gb/s/λ WDM Metro Networking," *IEEE/OSA Journal of Lightwave Technology*, vol. 36, no. 1, pp. 27–36, 2018.

[59] M. Seimetz, "High-Order Modulation for Optical Fiber Transmission," *Springer Berlin Heidelberg*, Springer Series in Optical Sciences, 2010.

[60] T. Bo and H. Kim, "Toward Practical Kramers-Kronig Receiver: Resampling, Performance, and Implementation," *IEEE/OSA Journal of Lightwave Technology*, vol. 37, no. 2, pp. 461–469, 2019.

[61] T. Bo and H. Kim, "Kramers-Kronig Receiver Operable Without Digital Upsampling," *Optics Express*, vol. 26, no. 11, pp. 13 810–13 818, 2018.

[62] T. Bo and H. Kim, "Performance Analysis of Kramers–Kronig Receiver in the Presence of IQ Imbalance," *IEEE Photonics Technology Letters*, vol. 30, no. 24, pp. 2171–2174, 2018.

[63] M. Schuster, S. Randel, C. A. Bunge, *et al.*, "Spectrally Efficient Compatible Single-Sideband Modulation for OFDM Transmission With Direct Detection," *IEEE Photonics Technology Letters*, vol. 20, no. 9, pp. 670–672, 2008.

[64] X. Chen, A. Li, D. Che, *et al.*, "High-speed Fading-free Direct Detection for Double-sideband OFDM Signal via Block-wise Phase Switching," *Optical Fiber Communication Conference and Exhibition and the National Fiber Optic Engineers Conference (OFC/NFOEC)*, pp. 1–3, 2013.

[65] X. Chen, A. Li, Q. Hu, *et al.*, "Demonstration of Direct Detected Optical OFDM Signals via Block-Wise Phase Switching," *IEEE/OSA Journal of Lightwave Technology*, vol. 32, no. 4, pp. 722–728, 2014.

[66] D. Che, Q. Hu, and W. Shieh, "Linearization of Direct Detection Optical Channels Using Self-Coherent Subsystems," *IEEE/OSA Journal of Lightwave Technology*, vol. 34, no. 2, pp. 516–524, 2016.

[67] D. Che, A. Li, X. Chen, *et al.*, "Stokes Vector Direct Detection for Linear Complex Optical Channels," *IEEE/OSA Journal of Lightwave Technology*, vol. 33, no. 3, pp. 678–684, 2015.

[68] W. Shieh and D. Che, "Optical Field Recovery via Stokes Vector Direct Detection," *Optical Fiber Communications Conference and Exhibition (OFC)*, pp. 1–3, 2019.

[69] Y. Ma, W. Shieh, and Q. Yang, "Bandwidth-Efficient 21.4 Gb/s Coherent Optical 2×2 MIMO OFDM Transmission," *Optical Fiber Communication Conference and Exhibition and the National Fiber Optic Engineers Conference (OFC/NFOEC)*, pp. 1–3, 2008.

[70] B. J. C. Schmidt, Z. Zan, L. B. Du, *et al.*, "120 Gbit/s Over 500-km Using Single-Band Polarization-Multiplexed Self-Coherent Optical OFDM," *IEEE/OSA Journal of Lightwave Technology*, vol. 28, no. 4, pp. 328–335, 2010.

[71] X. Chen, A. Li, D. Che, *et al.*, "Block-wise Phase Switching for Double-sideband Direct Detected Optical OFDM Signals," *Optics Express*, vol. 21, no. 11, pp. 13 436–13 441, 2013.

[72] D. Che, A. Li, X. Chen, *et al.*, "160-Gb/s Stokes Vector Direct Detection for Short Reach Optical Communication," *Optical Fiber Communications Conference and Exhibition (OFC)*, pp. 1–3, 2014.

[73] X. Zhou, J. Huo, K. Zhong, *et al.*, "Single Channel 50 Gbit/s Transmission Over 40 km SSMF Without Optical Amplification and In-Line Dispersion Compensation Using a Single-End PD-Based PDM-SSB-DMT System," *IEEE Photonics Journal*, vol. 9, no. 5, pp. 1–11, 2017.

[74] Y. Zhu, M. Jiang, and F. Zhang, "Direct Detection of Polarization Multiplexed Single Sideband Signals with Orthogonal Offset Carriers," *Optics Express*, vol. 26, no. 12, pp. 15 887–15 898, 2018.

[75] D. Lu, X. Zhou, J. Huo, *et al.*, "Theoretical CSPR Analysis and Performance Comparison for Four Single-Sideband Modulation Schemes With Kramers-Kronig Receiver," *IEEE Access*, vol. 7, pp. 166 257–166 267, 2019.

[76] X. Zhang, C. Zhang, C. Chen, *et al.*, "Digital Chromatic Dispersion Pre-management for SSB Modulation Direct-detection Optical Transmission Systems," *Optics Communications*, vol. 427, pp. 551–556, 2018.

[77] W.-R. Peng, X. Wu, K.-M. Feng, *et al.*, "Spectrally Efficient Direct-detected OFDM Transmission Employing an Iterative Estimation and Cancellation Technique," *Optics Express*, vol. 17, no. 11, pp. 9099–9111, 2009.

[78] A. J. Lowery, L. B. Du, and J. Armstrong, "Performance of Optical OFDM in Ultralong-Haul WDM Lightwave Systems," *IEEE/OSA Journal of Lightwave Technology*, vol. 25, no. 1, pp. 131–138, 2007.

[79] M. Zhu, J. Zhang, X. Yi, *et al.*, "Hilbert Superposition and Modified Signal-to-signal Beating Interference Cancellation for Single Side-band Optical NPAM-4 Direct-detection System," *Opt. Express*, vol. 25, no. 11, pp. 12 622–12 631, 2017.

[80] S. T. Le, K. Schuh, M. Chagnon, *et al.*, "1.72-Tb/s Virtual-Carrier-Assisted Direct-Detection Transmission Over 200 km," *IEEE/OSA Journal of Lightwave Technology*, vol. 36, no. 6, pp. 1347–1353, 2018.

[81] W. Peng, I. Morita, and H. Tanaka, "Enabling High Capacity Direct-detection Optical OFDM Transmissions Using Beat Interference Cancellation Receiver," *European Conference on Optical Communication (ECOC)*, pp. 1–3, 2010.

[82] M. Al-Qadi, G. Vedala, M. O'Sullivan, *et al.*, "QD-MLL-Based Single-Sideband Superchannel Generation Scheme With Kramers–Kronig Direct Detection Receivers," *IEEE Photonics Journal*, vol. 11, no. 4, pp. 1–13, 2019.

[83] H. Bulow, F. Buchali, and A. Klekamp, "Electronic Dispersion Compensation," *IEEE/OSA Journal of Lightwave Technology*, vol. 26, no. 1, pp. 158–167, 2008.

[84] K. Roberts, "Electronic Dispersion Compensation Beyond 10 Gb/s," *IEEE/LEOS Summer Topical Meetings*, pp. 9–10, 2007.

[85] H. Bulow, "Tutorial Electronic Dispersion Compensation," *Optical Fiber Communication Conference and Exhibition and the National Fiber Optic Engineers Conference (OFC/NFOEC)*, pp. 1–25, 2007.

[86] S. J. Savory, G. Gavioli, R. I. Killey, *et al.*, "Electronic Compensation of Chromatic Dispersion Using a Digital Coherent Receiver," *Optics Express*, vol. 15, no. 5, pp. 2120–2126, 2007.

[87] R. I. Killey, P. M. Watts, V. Mikhailov, *et al.*, "Electronic Dispersion Compensation by Signal Predistortion using Digital Processing and a Dual-drive Mach-Zehnder Modulator," *IEEE Photonics Technology Letters*, vol. 17, no. 3, pp. 714–716, 2005.

[88] Z. Li, M. S. Erkilinç, K. Shi, *et al.*, "Joint Optimisation of Resampling Rate and Carrier-to-Signal Power Ratio in Direct-Detection Kramers-Kronig Receivers," *European Conference on Optical Communication (ECOC)*, pp. 1–3, 2017.

[89] S. T. Le, K. Schuh, R. Dischler, *et al.*, "Beyond 400 Gb/s Direct Detection over 80km for Data Center Interconnect Applications," *IEEE/OSA Journal of Lightwave Technology*, pp. 538–545, 2019.

[90] K. Zou, Y. Zhu, F. Zhang, *et al.*, "Spectrally efficient terabit optical transmission with Nyquist 64-QAM half-cycle subcarrier modulation and direct detection," *Optics Letters*, vol. 41, no. 12, pp. 2767–2770, 2016.

[91] Z. Li, M. S. Erkilinc, R. Maher, *et al.*, "Reach Enhancement for WDM Direct-Detection Subcarrier Modulation using Low-Complexity Two-Stage Signal-Signal Beat Interference Cancellation," *European Conference on Optical Communication (ECOC)*, pp. 1–3, 2016.

[92] S. Randel, D. Pilori, S. Chandrasekhar, *et al.*, "100-Gb/s Discrete-multitone Transmission Over 80-km SSMF Using Single-sideband Modulation with Novel Interference-cancellation Scheme," *European Conference on Optical Communication (ECOC)*, pp. 1–3, 2015.

[93] Z. Li, M. Sezer Erk1l1nç, R. Maher, *et al.*, "Two-Stage Linearization Filter for Direct-Detection Subcarrier Modulation," *IEEE Photonics Technology Letters*, vol. 28, no. 24, pp. 2838–2841, 2016.

[94] M. Lyu, W. Shi, and L. A. Rusch, "SiP Alternative to Enhanced KK for OFDM," *European Conference on Optical Communication (ECOC)*, pp. 1–3, 2018.

[95] Z. Tu, A. Wen, G. Yu, *et al.*, "A Wideband Photonic RF Receiver With Lower IF Frequency Enabled by Kramers–Kronig Detection," *IEEE/OSA Journal of Lightwave Technology*, vol. 37, no. 20, pp. 5309–5316, 2019.

[96] X. Chen, S. Chandrasekhar, S. Olsson, *et al.*, "Impact of O/E Front-End Frequency Response on Kramers-Kronig Receivers and its Compensation," *European Conference on Optical Communication (ECOC)*, pp. 1–3, 2018.

[97] H. Voelcker, "Demodulation of Single-Sideband Signals Via Envelope Detection," *IEEE Transactions on Communication Technology*, vol. 14, no. 1, pp. 22–30, 1966.

[98] Z. Wu, H. Jiang, X. Feng, *et al.*, "Demonstration of Cost-Effective Single-Photodetector Coherent Receiver for Free-Space Optical Communications," *Asia Communications and Photonics Conference (ACP)*, pp. 1–3, 2017.

Chapter 3

DC-Value Method

In the previous Chapter 2, we discussed state of the art short-reach systems with their enabling technologies and standards with the main focus on the short-reach optical links such as metro and access networks and datacenter networks (DCNs). Single sideband (SSB) transmission systems play a vital role in short-reach optical networks, however, their performance is limited by the signal-to-signal beating noise (SSBN). Several solutions are proposed to address the SSBN issue, however, they tend to suffer either local minimum convergence, high sampling-rate requirement, and sensitivity penalty problems.

In this chapter, a novel DC-Value method is proposed to reconstruct the missing phase information in the direct-detection (DD) optical communication system. The proposed method effectively alleviates the SSBN and its working principle is based on the reception of a minimum phase signal.

Section 3.1 presents an introduction about the minimum phase signal, the Kramers-Kronig (KK) algorithm, and the associated challenges to its implementation. In section 3.2, the proposed DC-Value method is explained in detail to recover the phase information of the signal from its magnitude information though necessary and sufficient conditions discussed in section 3.1. In section 3.3, the performance assessment of the proposed DC-Value method is carried out for the different modulation formats without noise. In section 3.4, the proposed method is analyzed in the presence of noise and compared results with the other state of the art phase reconstruction methods. Finally, section 3.5 presents the concluding remarks.

3.1 Introduction

This section describes the process of converting complex information signal into the minimum phase signal. In the subsequent sections, the KK and upsampling free KK methods are discussed. Finally, the implementation challenges of the KK algorithms are summarized.

3.1.1 Minimum Phase Signal

By definition, the minimum phase signal is a complex signal whose real and imaginary parts are Hilbert pairs of each other and the real part is non-negative. To understand the characteristics of the minimum phase signal, we start with the explanation of converting non-analytic

bandlimited complex information signal $E_s(t)$ into minimum phase incoming signal $E(t)$. Let us define $E_s(t)$ as a complex envelop of the band-limited information carrying signal confined within a bandwidth B. If the signal $E_s(t)$ is not an analytic signal then it can be made so by appropriate frequency translations. That is,

$$E_{ssb}(t) = E_s(t)e^{i\omega_B t} \tag{3.1}$$

where, $E_{ssb}(t)$ represents the analytical signal for $\omega_B \geq \pi B$. The analytical signal possesses single sideband (SSB) property and its real and imaginary parts are related by Hilbert transform relation,

$$E_{ssb,i}(t) = \mathcal{H}\{E_{ssb,r}(t)\} \tag{3.2}$$

$$E_{ssb,r}(t) = -\mathcal{H}\{E_{ssb,i}(t)\} \tag{3.3}$$

where, $\mathcal{H}\{\bullet\}$ represents the Hilbert transformation, and $E_{ssb,r}(t)$ and $E_{ssb,i}(t)$ are real and imaginary parts of $E_{ssb}(t)$, respectively. The analytical continuation of the signal $E_{ssb}(t)$ in the upper half of the complex z plane with $z = t+i\tau$ does not include any singularity for $\tau \geq 0$. From the definition of the inverse Fourier transform,

$$E_{ssb}(z) = \frac{1}{2\pi}\int_{-\infty}^{\infty} \tilde{E}_{ssb}(\omega)\ e^{i\omega z}\ d\omega \tag{3.4}$$

where, $\tilde{E}_{ssb}(\omega)$ represents the Fourier transform of $E_{ssb}(t)$. From the single sideband property of the analytic signal, we can write (3.4) as,

$$E_{ssb}(z) = \frac{1}{2\pi}\int_{0}^{\infty} \tilde{E}_{ssb}(\omega)\ e^{i\omega z}\ d\omega \tag{3.5}$$

and substituting the value of z,

$$E_{ssb}(z) = \frac{1}{2\pi}\int_{0}^{\infty} [\tilde{E}_{ssb}(\omega)\ e^{-\omega\tau}]\ e^{i\omega t}\ d\omega \tag{3.6}$$

That is, (3.6) will converge for any ω and $\tau \geq 0$. From (3.6), it is evident that analyticity follows from the single sideband nature of the $\tilde{E}_{ssb}(\omega)$, and single sideband can be obtained if the real and imaginary parts are related by Hilbert transform.

Necessary and sufficient condition for the minimum phase

The converse relationship also holds such that the real and imaginary parts will be a Hilbert pair if the signal is analytic and it vanishes at $z \to \infty$ with $\tau \geq 0$. Applying logarithmic to the signal $E_{ssb}(t)$,

$$\ln\{E_{ssb}(t)\} = \ln\{|E_{ssb}(t)|\} + i\phi(t) \tag{3.7}$$

where $\phi(t)$ is the phase information in radians. From the definition, if signal $E_{ssb}(t)$ satisfies the minimum phase condition then the real and imaginary parts of (3.7) are related by Hilbert transform,

$$\phi(t) = \mathcal{H}\{\ln|E_{ssb}(t)|\} \tag{3.8}$$

$$E_{ssb}(t) = |E_{ssb}(t)|e^{i\mathcal{H}\{\ln|E_{ssb}(t)|\}} \tag{3.9}$$

Equation (3.9) is legitimate if it obeys the following conditions, (i) the function $\ln\{E_{ssb}(z)\}$ must be analytic in the upper half of complex z plane, and (ii) $\ln\{E_{ssb}(z)\}$ must vanish when

$z \to \infty$ and $\tau \geq 0$. From the convergence property of the logarithmic, the function $\ln\{E_{ssb}(z)\}$ will be free from singularities if it does not possess zeros in the upper half of the complex z plane. This requirement can be fulfilled if a constant $|E_o|$ is added to the real part of the complex signal which ensures the non-negativity of the signal. Therefore, the revamped signal whose logarithm is analytic in the upper half of the complex z plane can be given as,

$$E(t) = |E_o| + E_{ssb}(t) \tag{3.10}$$

where $|E_o| > |E_{ssb}(t)|$ and $E(t)$ is called a minimum phase signal. The second constrain requires that the signal must vanish at the extremities of the upper half of the complex z plane. The proof of the second constraint can be viewed from the (3.10) as,

$$E(z) = |E_o|\left[1 + \frac{E_{ssb}(z)}{|E_o|}\right] \tag{3.11}$$

As $E(z)$ is stable (Fourier transformable), we can apply the initial value theorem,

$$\ln\{\tilde{E}(0)\} = \lim_{z\to\infty} \ln\{E(z)\} = \ln\{|E_o|\},\ for\ \tau \geq 0. \tag{3.12}$$

therefore,

$$\lim_{z\to\infty} \ln\left[\frac{E(z)}{|E_o|}\right] = 0,\ for\ \tau \geq 0. \tag{3.13}$$

Therefore, the necessary and sufficient condition for the $E(t)$ to be minimum phase is that $\tilde{E}(\omega)$ be SSB i.e. $\tilde{E}(\omega) = 0$ for $\omega < 0$ and $\tilde{E}(0) = |E_o|$. These conditions of the minimum phase signal can be used to develop the DC-Value algorithm (discussed in section 3.2) to reconstruct the minimum phase signal from its magnitude information.

3.1.2 Kramers-Kronig (KK) Method

As discussed earlier, the minimum phase condition of the signal implies that log-magnitude and phase are related by the Hilbert transform (commonly referred to as KK relation), and this requirement can be full filled by adding a constant DC value in the SSB complex signal [1]. Therefore, for a minimum-phase optical SSB signal, the phase information can be retrieved from its intensity by the KK relation. In the following subsections, the conventional KK algorithm, as well as the modified alternatives, are discussed.

3.1.2.1 Conventional KK Method

A typical block diagram of the conventional KK scheme is depicted in Fig. 3.1. A complex optical data $E_s(t)\ e^{i\omega_s t}$ is superimposed on a co-polarized reference optical carrier $E_o\ e^{i\omega_{E_o} t}$ with a real-valued amplitude E_o at the transmitter (Tx). In this regards, an optical signal, $E(t) = (E_o + E_s(t)e^{i\omega_Z t})e^{i\omega_{E_o} t}$, impinges on the DD receiver (Rx), where $\omega_Z = \omega_s - \omega_{E_o}$. In addition, the KK concept is based on the application of Hilbert transform to an analytic signal with known amplitude information only, in order to determine the corresponding phase. Moreover, if the spectrum of the signal, $E_{ssb}(t) = E_s(t)e^{i\omega_Z t}$, does not extend to negative frequencies, then it is analytic. Also, in accordance with the KK concept, the carrier has to be sufficiently large to fulfill the minimum-phase condition (i.e. $|E_s(t)| < E_o$) with a reasonably high degree of confidence. In reality, this indicates that the carrier to signal power

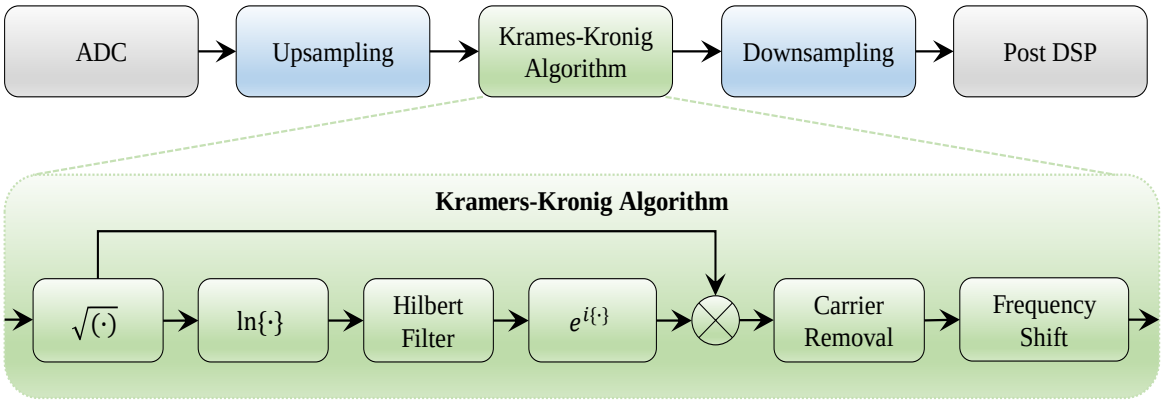

Figure 3.1: KK algorithm.

ratio (CSPR) must be larger than the signal peak to average power ratio (PAPR) to ensure an accurate digital signal processing (DSP)-based phase retrieval. It is noteworthy that an unlimited number of higher harmonics will be generated due to the associated nonlinearities of the operation in the KK algorithm. So, before executing the nonlinear operations, output data of the analog to digital converter (ADC) has to be sufficiently upsampled to inhibit aliasing errors [2]–[6]. The conventional KK algorithm retrieves the phase information from the intensity information via the Hilbert transform as follows,

$$\phi(t) = \mathcal{H}\left\{\ln\sqrt{I(t)}\right\} \tag{3.14}$$

where $\ln(\bullet)$ and $\mathcal{H}\{\bullet\}$ denote the natural logarithm operation and Hilbert transformation, respectively. Consequently, the recovered electrical field can be written as,

$$E(t) = \sqrt{I(t)}\ \mathrm{e}^{i\phi(t)} = |E_o| + E_s(t)\ \mathrm{e}^{i\omega_Z t} \tag{3.15}$$

The next process is the removal of the reference carrier. Also, the subsequent signal can then be shifted from the intermediate frequency, ω_Z, to the baseband. Subsequently, the recovered complex data signal can be written as,

$$E_s(t) = \left[\sqrt{i(t)}\ \mathrm{e}^{i\phi(t)} - |E_o|\right] e^{-i\omega_Z t} \tag{3.16}$$

Moreover, digital downsampling can also be implemented and further DSP like electrical equalization, carrier recovery, and demodulation process, etc. are applied in a similar fashion like tradition coherent (COH) receiver. In the following subsection, we discuss a number of modifications employed to get rid of the digital upsampling process in the conventional KK algorithm.

3.1.2.2 Upsampling Free KK Method

As aforementioned, the spectral broadening is as a result of nonlinear operations and a viable solution has to find a way of getting around their execution. This can be achieved by

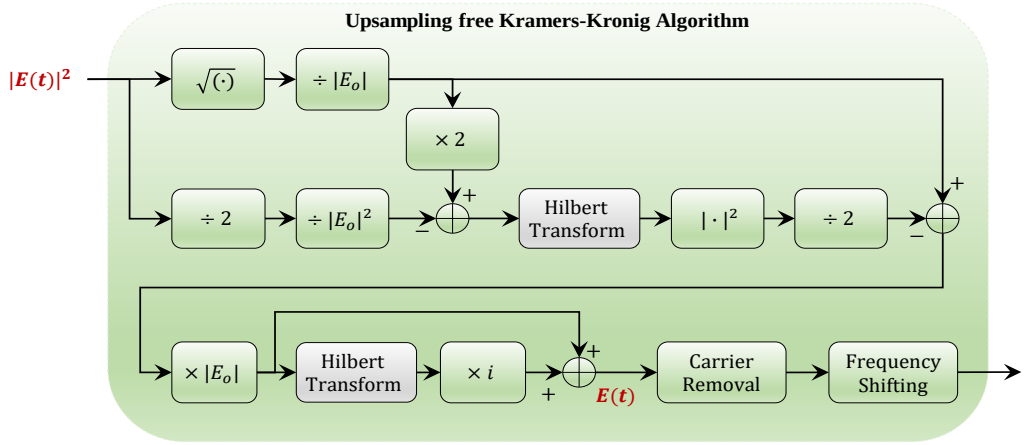

Figure 3.2: Upsampling free KK algorithm. $|E_o|$: Carrier amplitude

exploiting a DSP algorithm with digital upsampling free [7]. For instance, suitable mathematical approximations can be employed to get around the associated nonlinear operations of the conventional KK algorithm. In this context, see Fig. 3.2, the square root of $I(t)$ can be approximated to second-order binomial expansion. Furthermore, by exploiting the minimum-phase condition, the phase of the signal can also be approximated [4], [5]. Besides, the function, $\ln\sqrt{I(t)}$, can as well be approximated based on the second-order Taylor's expansion [4], [5]. Besides, the logarithm function that can be approximated, the exponential function can also be eliminated through the Cartesian form representation of the complex signal [3]. Thus, the real part of the signal can be expressed as [5],

$$|E_o| + E_s(t) \cong \sqrt{I(t)} - \frac{|E_o|}{2}\left\{\mathcal{H}\left[2\frac{\sqrt{I(t)}}{|E_o|} - \frac{1}{2}\frac{I(t)}{|E_o|^2}\right]\right\}^2 \tag{3.17}$$

It should be noted that the stated KK algorithm facilitates upsampling free operation at the expense high CSPR which consequently leads to receiver sensitivity degradation. It is noteworthy that some approaches may still comprise some nonlinear operations like square and square-root functions in the modification process. Nevertheless, a comparative study has established that the associated nonlinear operations of the upsampling free KK algorithm present negligible contribution to the spectral broadening.

3.1.3 Full DSP Procedure for KK Scheme

In this subsection, consideration is given to the required full DSP procedure when the KK algorithm is adopted. The demanded procedure depends mainly on the polarization order (i.e. single- or dual-polarization).

3.1.3.1 DSP for Single-Polarization KK Scheme

A typical single-polarization KK DSP subsystem is illustrated in Fig. 3.3a. The initial block is for the optoelectronic front-end compensation which is optional. This is followed by the KK optical field reconstruction through the KK algorithm. After the KK algorithm, the linear equalizer can be implemented for the chromatic dispersion (CD) compensation. After this

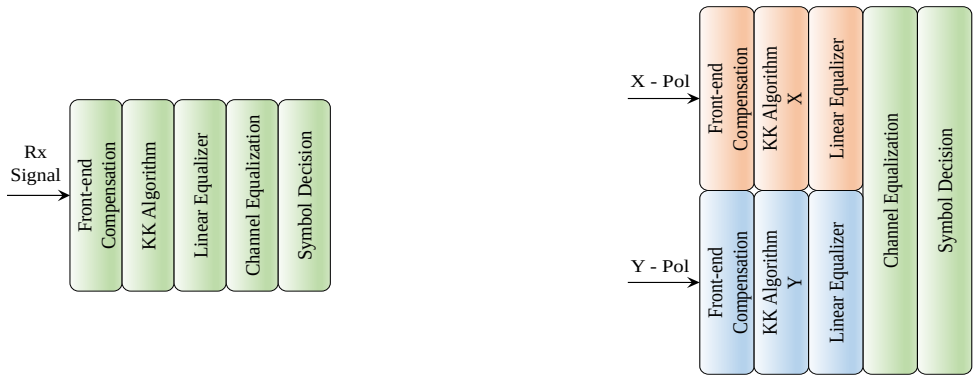

(a) **(b)**

Figure 3.3: Typical KK receiver DSP for (a) single-polarization, (b) dual-polarization

process, adaptive equalizers can be employed for the equalization of the dispersion compensated signal. This is an effort to compensate for channel distortions as usually adopted in the signal processing chain of a standard intradyne. So, after the channel equalization, decisions can then be made on symbol [8].

3.1.3.2 DSP for Dual-Polarization KK Scheme

The KK concept can be extended to a dual-polarization (DP) scheme by employing a polarization diversity setup at the Rx as shown in Fig. 3.3(b). In this context, the optical field in both polarizations can be autonomously recovered. Therefore, the two transmit signal polarizations can be separated with the aids of the KK algorithm and a standard 2×2 multiple input multiple output (MIMO) processing. It should be noted that, based on this implementation, the continuous wave (CW) tone generation at the Tx and its transmission in conjunction with the signal is impractical. So, to fulfill the KK condition, a separate CW tone is required at the Rx for both signal polarization. To realize this, a CW light source with an arbitrary input polarization has to be split into two orthogonal polarizations and with equal power [8], [9]. However, the main concern about this implementation is the availability of passive linear optical device that can realize the purpose.

3.1.4 Requirements and Challenges

As stated earlier, some technical challenges require significant attention for the effective implementation of the KK algorithm. Table 3.1 presents a number of modification efforts for addressing the technical challenges and their associated trade-offs. They are grouped by the matter that they tried to address. For instance, some schemes tried to address the required upsampling, while some focused on the demanded high CSPR. However, it has been observed that for perfect reconstruction, most of the efforts usually achieve their aims at the expense of additional penalties that are related to factors such as CSPR, complexity, latency, bandwidth, and cost.

Table 3.1: A Summary of Modified KK Algorithms

Ref.	Adopted technique	Advantages	Tradeoff
Digital upsampling			
[7]	DSP algorithm without digital upsampling	• fewer samples per symbol	• requires multiple iterations • incurs complexity • incurs latency
[2]	modified Hilbert filter in digital domain	• low-complexity	• high CSPR
[4], [5]	approximated functions	• less samples per symbol	• high CSPR
[3]	approximated functions and exponential function elimination	• less samples per symbol	• performance degradation at absolutely high SNR
[10]	DSP algorithm without digital upsampling	• lesser CSPR penalty	• requires multiple iterations
High CSPR			
[11]	flexible adaptive dispersion compensation	• low CSPR	• high iterative DSP • additional hardware • additional cost
[12]	hardware SSBN cancellation	• low-complexity,cost,CSPR • small footprint • MPC* not required	• requires iterative process
[13]	enhanced SSBN mitigation algorithm	• low CSPR • improved OSNR	• incurs spectral broadening
[14]	employs exponential operation	• low CSPR	• retrieves information-bearing signal • incurs spectral broadening
[15]	employs exponential operation	• low CSPR	• incurs spectral broadening • demands greater system bandwidth

***MPC:** Minimum Phase Condition

3.2 Self-Coherent DC-Value Method

The block diagram of the proposed DC-Value method is shown in Fig. 3.4. The complex envelope of the incoming SSB optical signal is $E(t) = E_o + E_{ssb}(t)$ (as discussed in (3.10)), where E_o is the complex amplitude of the optical carrier which ensures the DC-Value property, and $E_{ssb}(t)$ is the complex SSB signal. When the field is detected using a single photodetector, the generated photocurrent can be expressed as [5],

$$I(t) \propto \left(\underbrace{|E_o|^2}_{\text{DC}} + \underbrace{2\Re\{E_o E_{ssb}(t)\}}_{\text{carrier-signal}} + \underbrace{|E_{ssb}(t)|^2}_{\text{signal-signal}} \right) \tag{3.18}$$

$$\begin{aligned} |E(t)| =& \sqrt{|E_o|^2 + 2\Re\{E_o E_{ssb}(t)\} + |E_{ssb}(t)|^2} \\ =& \Re\left\{ \frac{E_o E_{ssb}(t)}{|E_o|} \right\} + |E_o| \left[1 + \frac{1}{2} \frac{|E_{ssb}(t)|^2}{|E_o|^2} - \frac{1}{8} \left(\frac{2\Re\{E_o E_{ssb}(t)\} + |E_{ssb}(t)|^2}{|E_o|^2} \right)^2 \right. \\ & \left. + \frac{1}{16} \left(\frac{2\Re\{E_o E_{ssb}(t)\} + |E_{ssb}(t)|^2}{|E_o|^2} \right)^3 - \dots \right] \end{aligned} \tag{3.19}$$

where, $\Re\{\bullet\}$ represents the real part of $\{\bullet\}$, the first term, $|E_o|^2$, is the DC component, the second term, $2\Re\{E_o E_{ssb}(t)\}$, is the carrier-signal beating, and the last term, $|E_{ssb}(t)|^2$, is the signal-signal beating. The photocurrent is then amplified using a trans-impedance amplifier (TIA) and filtered by a low pass filter. For simplicity, we consider the photodetector responsivity R_{pd} and the TIA gain G such that $R_{pd}G = 1$. Without loss of generality, we assume that E_o is real, i.e. the E_o phase is zero, and the phase of $E_{ssb}(t)$ is measured in relation to the phase of E_o. Note that both signals E_o and $E_{ssb}(t)$ are supposed to be generated in the transmitter from the same laser and within the laser coherence time. The power of the carrier E_o in relation to the power of the signal defines the CSPR. The CSPR is defined as,

$$\text{CSPR} = \frac{|\text{E}_\text{o}|^2}{\langle |\text{E}_\text{ssb}(\text{t})|^2 \rangle} \tag{3.20}$$

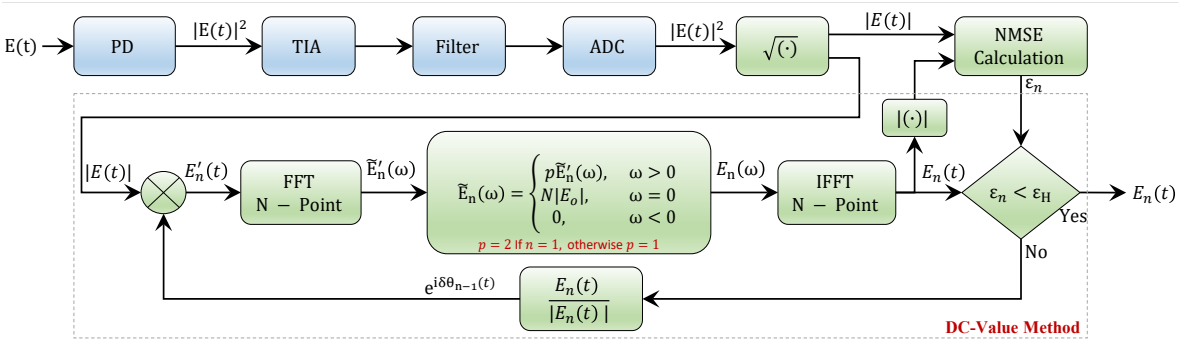

Figure 3.4: The schematic of the DC-Value method to reconstruct the full electric field of a minimum phase signal from its intensity information. A constant scaling factor p helps to speed up the convergence process. The process iterates continuously until the normalized mean squared error (NMSE), ε_n, between $|E(t)|$ and $|E_n(t)|$ becomes less than threshold error ε_H.

where, $\langle \bullet \rangle$ is an average operator. The current signal is then digitized using an ADC at the frequency that is not less than the Nyquist limit, i.e. 2B, where B is is the photocurrent bandwidth. Afterward, the square-root operation is carried out to obtain the amplitude $|E(t)|$ of the optical field. Taylor's series expansion of the nonlinear square root operation can be written as (3.19), showing the presence of the $\mathrm{Re}\{E(t)\}$ term and higher-order terms. As evident from (3.19), the impact of higher-order terms can be made less severe by increasing the tone power. After the square root operation, see Fig. 3.4, the amplitude information signal $|E(t)|$ is multiplied by a phase correction factor $e^{i\delta\theta_{n-1}(t)}$ which outputs the complex signal $E'_n(t)$, where n represents the iteration number. In the first iteration (for $n = 1$), the phase correction factor is assumed to be zero, i.e. $\delta\theta_0(t) = 0$. Next, the SSB and DC-Value properties of the minimum phase signal are imposed on the Fourier transformed signal $\tilde{E'}_n(\omega)$ to attain $\tilde{E}_n(\omega)$ as,

$$\tilde{E}_n(\omega) = \begin{cases} p\tilde{E'}_n(\omega), & \text{for } \omega > 0 \\ N|E_o|, & \text{for } \omega = 0 \\ 0, & \text{for } \omega < 0 \end{cases} \tag{3.21}$$

where, N represents the length of the fast Fourier transform (FFT), n represents the iteration number, and p denotes the scaling factor given by,

$$p = \begin{cases} 2, & \text{for } n = 1 \\ 1, & \text{for } n > 1 \end{cases} \tag{3.22}$$

The input signal, $E'_n(t)$, for the first iteration consists of a real-valued amplitude signal $|E(t)|$ (i.e. $\delta\theta_0(t) = 0$). The minimum phase condition imposed on the signal forces the negative frequency components to zero and it generates complex-valued signal $E_1(t)$ in the time domain (starts acquiring the phase information). As a consequence of forcing negative frequency components to zero, the signal $E_1(t)$ will have its real and imaginary parts amplitude scaled by a factor 0.5. Therefore, we set a scaling factor $p = 2$ to adjust the amplitude of the information signal in the first iteration. As shown in the next section, the scaling factor p used in the reconstruction process greatly speeds up the convergence process (see Fig. 3.8). After imposing a minimum phase condition, the inverse Fourier transform of the $\tilde{E}_n(\omega)$ is computed to obtain $E_n(t)$. The NMSE, ε_n, between $|E(t)|$ and $|E_n(t)|$ can be calculated as,

$$\mathrm{NMSE} = \frac{\int_{-\infty}^{\infty} \Big|\, |\mathrm{E(t)}| - |\mathrm{E_n(t)}| \,\Big|^2 \mathrm{dt}}{\int_{-\infty}^{\infty} \Big|\, \mathrm{E(t)} \,\Big| \mathrm{dt} \int_{-\infty}^{\infty} \Big|\, \mathrm{E_n(t)} \,\Big| \mathrm{dt}}, \tag{3.23}$$

If the value of the error ε_n is higher than the threshold error ε_H then the updated phase correction vector corresponding to $E_n(t)$ can be calculated as $e^{i\delta\theta_n(t)} = \frac{E_n(t)}{|E_n(t)|}$. This phase estimate $e^{i\delta\theta_n(t)}$ can be supplied as a piece of updated phase information for the subsequent iteration as shown in Fig.3.1. This process would repeat continuously until the NMSE, ε_n, reaches below the threshold ε_H. In subsequent section 3.2.1, we have shown that the NMSE, ε_n, between the known magnitude $|E(t)|$ and the estimated magnitude $|E_n(t)|$ is monotonically decreasing after each iteration and has lower bound to zero, therefore, the reconstruction process converges to a limit point.

3.2.1 Normalize Mean Squared Error (NMSE) Reduction

Consider an error function, E_n, as the mean squared error between known magnitude, $|E(t)|$, and the estimate magnitude, $|E_n(t)|$, on each iterations as,

$$E_n = \int_{-\infty}^{\infty} \Big| \, |E(t)| - |E_n(t)| \, \Big|^2 dt \tag{3.24}$$

Following [16], we show that the error function is a monotonically decreasing function. Consider the identity $|e^{[i\delta\theta_n(t)]}|^2 = 1$ to express (3.23) as,

$$\begin{aligned} E_n &= \int_{-\infty}^{\infty} \Big| \, |E(t)|e^{(i\delta\theta_n(t))} - |E_n(t)|e^{(i\delta\theta_n(t))} \Big|^2 dt \\ E_n &= \int_{-\infty}^{\infty} |E_n'(t) - \tilde{E}_n(t)|^2 dt \end{aligned} \tag{3.25}$$

From the Parseval's theorem (3.25) can be given in the frequency domain as,

$$E_n = \frac{1}{2\pi} \int_{-\pi}^{\pi} |\tilde{E'}_n(\omega) - \tilde{E}_n(\omega)|^2 d\omega \tag{3.26}$$

where $\tilde{E'}_n(\omega)$ and $\tilde{E}_n(\omega)$ are the FFT of $E_n'(t)$ and $\tilde{E}_n(t)$, respectively. From the minimum phase condition, it follows that, for $\omega > 0$,

$$|\tilde{E'}_n(\omega) - \tilde{E}_n(\omega)|^2 \geq |\tilde{E'}_n(\omega) - \tilde{E}_{n+1}(\omega)|^2 = 0 \tag{3.27}$$

and for $\omega \leq 0$,

$$|\tilde{E'}_n(\omega) - \tilde{E}_n(\omega)|^2 = |\tilde{E'}_n(\omega) - \tilde{E}_{n+1}(\omega)|^2. \tag{3.28}$$

Summing (3.27) and (3.28) over all ω, we get,

$$E_n = |\tilde{E'}_n(\omega) - \tilde{E}_n(\omega)|^2 \geq |\tilde{E'}_n(\omega) - \tilde{E}_{n+1}(\omega)|^2 \tag{3.29}$$

Therefore, from Parseval's theorem, and (3.29),

$$\begin{aligned} E_n &\geq \frac{1}{2\pi} \int_{-\pi}^{\pi} |\tilde{E'}_n(\omega) - \tilde{E}_{n+1}(\omega)|^2 d\omega \\ E_n &\geq \int_{-\infty}^{\infty} \Big| \, |E(t)| - |E_{n+1}(t)| \, \Big|^2 dt \\ E_n &\geq E_{n+1} \end{aligned} \tag{3.30}$$

Thus, E_n is a monotonically decreasing function.

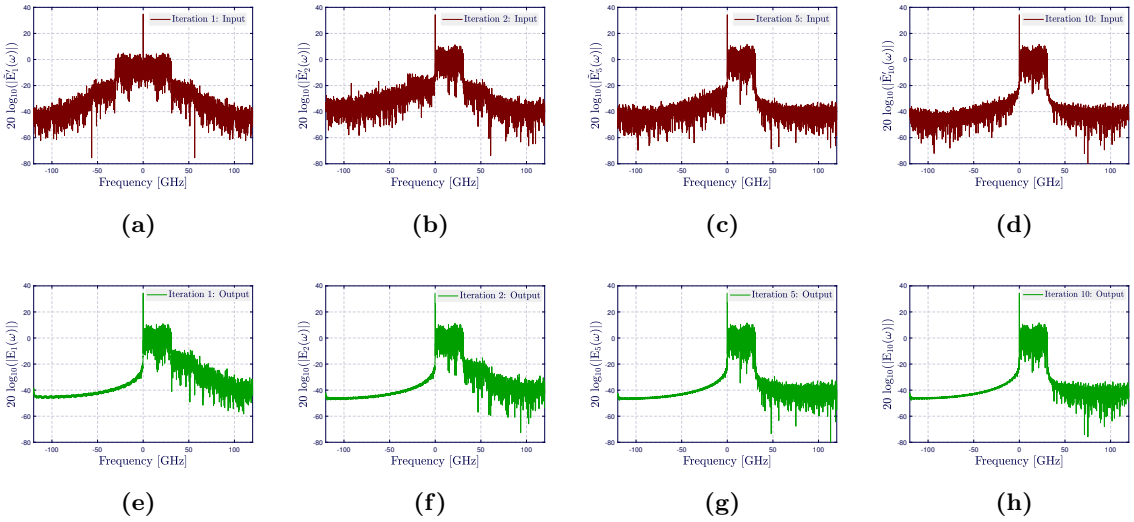

Figure 3.5: Magnitude spectrum of the input signal to the proposed method and output minimum phase signal after the execution of iteration 1, 2, 5, and 10 with the CSPR of 6 dB. Graphs (a), (b), (c) and (d) (top-panel) show the spectrum of the input signal $E'_n(t)$, and graphs (e), (f), (g), and (h) (bottom-panel) shows the spectrum of the recovered minimum phase signal $E_n(t)$ at the end of iteration number 1, 2, 5, and 10, respectively.

3.2.2 Convergence Process

The convergence process of the proposed DC-Value method is shown in Fig. 3.5, where the spectrum of the input $E'_n(t)$ and the recovered minimum phase signal $E_n(t)$ are displayed at the end of iteration number 1, 2, 5, and 10. For the assessment of the convergence process, the minimum phase signal $E(t)$ corresponding to 30 Gbaud 16QAM with 6 dB CSPR value is employed in the reconstruction process. For the first iteration, the input signal is $|E(t)|\ e^{i\delta\theta_0(t)} = |E(t)|$ (see Fig. 3.5(a)) since $e^{i\delta\theta_0(t)}$ is an unitary vector, and the corresponding output $E_1(t)$, is the first estimation of the minimum phase signal as shown in Fig. 3.5(e). Similarly, input and output corresponding to the second iteration can be given as $|E(t)|\ e^{i\delta\theta_1(t)}$ (where $e^{i\delta\theta_1(t)} = E_1(t)/|E_1(t)|$) and $E_2(t)$ as shown in Fig. 3.5(b) and Fig. 3.5(f), respectively.

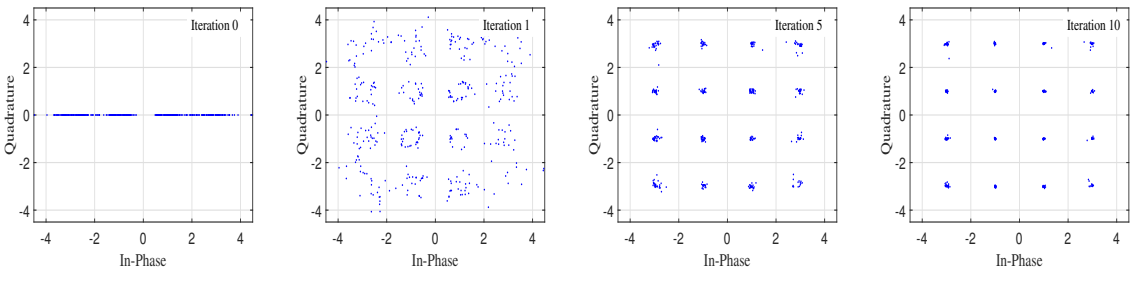

Figure 3.6: Recovered IQ constellations of the 30 Gbaud 16QAM signal by the proposed method after the execution of iteration numbers 0, 1, 5, and 10 with the CSPR of 6 dB. After 10 iterations the recovered constellation is very close to the ideal constellation.

Likewise, the input and output signals at the end of iteration 5 and 10 are shown in Fig. 3.5(c) and Fig. 3.5(g), and Fig. 3.5(d) and Fig. 3.5(h), respectively. The accuracy of the signal reconstruction process increases with the number of iterations and high CSPR value.

At the end, the recovered minimum phase signal $E(t)$ is passed through the DC remover and then downconverted to recover the 16QAM signal. Fig. 3.6 shows the constellation of the recovered 16QAM signal for iteration number 0, 1, 5, and 10. For iteration 1, the input does not contain any phase information i.e. $\delta\theta_0(t) = 0$, as shown in Fig. 3.6(a), and at the end of iteration 1, it starts recovering the phase information as shown in Fig. 3.6(b). As it is evident that error in the recovered signal is reduced in the subsequent iterations as shown in Fig. 3.6(c) and 3.6(d), which display the recovered signal constellation after iteration 5 and 10, respectively. It requires approximately 10 number of iterations to achieve close proximity to the ideal constellation with 6 dB CSPR.

Why we name this algorithm as DC-Value method?

The advantages offered by the proposed method depend on the accurate estimation of the $|E_o|$ component in (3.21) of the minimum phase condition (MPC). The $|E_o|$ is mere a constant DC term whose value depends on the amplitude carrier tone sitting at the edge of the information signal spectrum.

3.3 Performance Assessment Without Noise

In the following, we assess the performance of the proposed method without noise for different CSPR values and the number of iterations for the M-ary modulation formats. For the performance assessment of the method, single-channel 100 Gb/s QPSK and 16QAM, signals with 20% overhead (120 Gb/s) are employed, respectively. At the transmitter side, the complex signals are generated using a raised cosine pulse shaping filter with 0.05 roll-off factor. The complex signal is then multiplied by $e^{i2\pi ft}$, i.e. it is upconverted, to generate SSB signal $E_s(t)$, where $f \geq B/2$ and B is the bandwidth of the signal. Next, the DC value is added to the SSB signal ensuring that the real part of the SSB signal becomes non-negative, which generates a minimum phase signal $E(t)$ in the digital domain. The desired CSPR value can be adjusted either by varying the DC value or signal power. At the receiver side, the signal is detected using the DD technique and then processed to recover the full electric field of the minimum phase signal $E(t)$ as discussed in section 3.2. The recovered minimum phase signal $E(t)$ is passed through DC remover and then downconverted by $e^{-i2\pi ft}$ to recover the information signal. The error vector magnitude (EVM) metric is employed to provide a quantitative measure of the recovered signal by the proposed method. The EVM can be estimated as,

$$\mathrm{EVM}_{RMS} = \sqrt{\frac{\sum_{k=1}^{N}((I_k - \tilde{I}_k)^2 + (Q_k - \tilde{Q}_k)^2)}{\sum_{k=1}^{N}(I_k^2 + Q_k^2)}} \tag{3.31}$$

where, I_k and Q_k represent the in-phase and quadrature samples of the k^{th} transmitted symbol, respectively, and $\tilde{I}_k$ and $\tilde{Q}_k$ represent the in-phase and quadrature samples of the k^{th} recovered symbol, respectively, and N represents the length of the sequence. For the

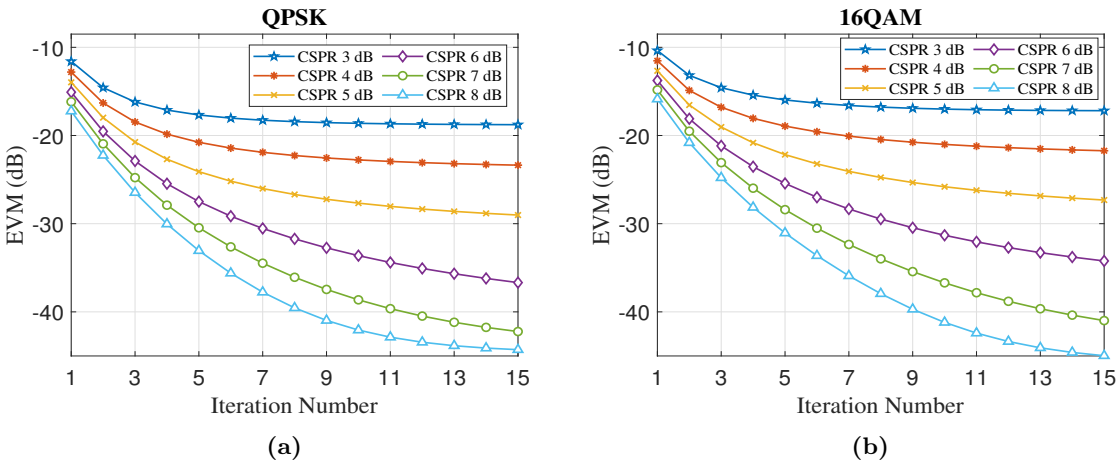

Figure 3.7: EVM versus iteration number of the recovered signal considering different CSPR values, for (a) QPSK, and (b) 16QAM signals. Each curve was obtained by varying the DC value to obtain desired CSPR values as shown in the legends.

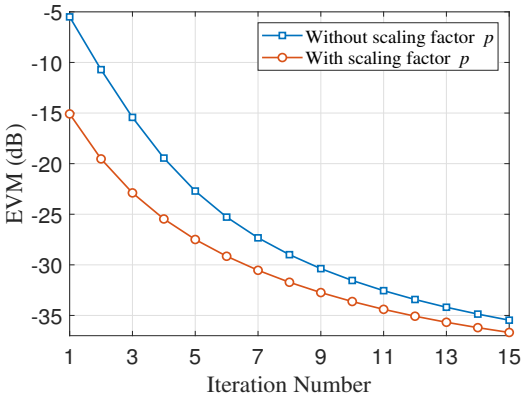

Figure 3.8: Comparison of EVM without and with a scaling factor p for the QPSK signal.

performance assessment, CSPR values of 3 dB, 4 dB, 5 dB, 6 dB, 7 dB, and 8 dB are employed and the reconstruction process is iterated for 15 iterations to recover the minimum phase signal. The EVM of the recovered QPSK and 16QAM signals after the execution of each iteration for different CSPR values are displayed in Fig. 3.7(a) and Fig. 3.7(b), respectively. It is shown that the EVM value improves after execution of each iteration, providing global minimum convergence. Without noise, the reconstruction process improves with the increase of the CSPR and the number of iterations. In the following, we discuss the impact of the inclusion of the scaling factor. Fig. 3.8 shows the EVM values of the recovered signal by the proposed method with and without scaling factor p. The figure shows that the implementation of the scaling factor provides approximately 6 dB, 4.5 dB, and 2.5 dB EVM gains for iteration numbers 4, 5, and 8, respectively. This shows that there is a considerable increase in the EVM gain with a low number of iterations with the implementation of the scaling factor. Alternatively, the employed scaling factor helps in enhancing the system convergence by reducing the required numbers of iterations n by 2. That is, instead of n iterations we need $n-2$ iterations. For simplicity, we present the results that are based on the QPSK

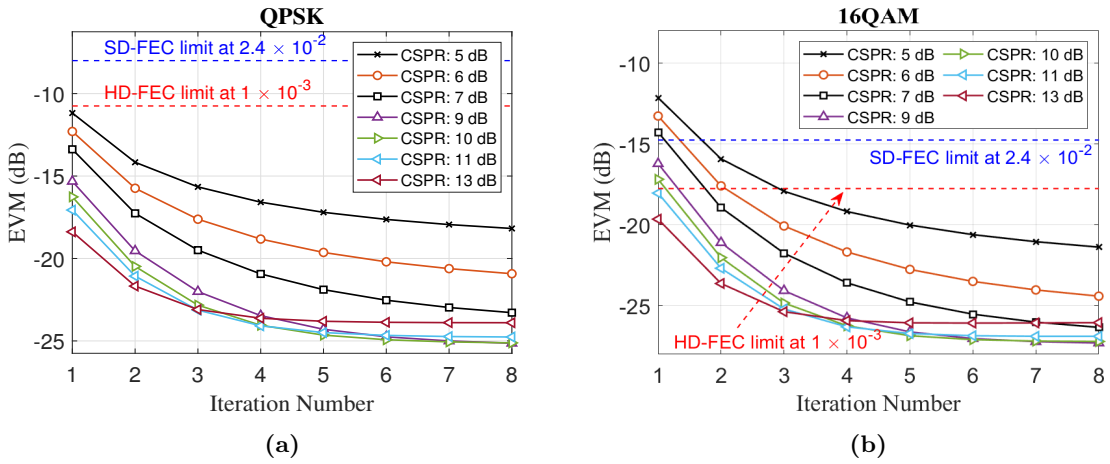

Figure 3.9: EVM of the recovered signal using the DC-Value method after 20 km of SSMF with 3 dBm transmitted power. Blue and red dashed lines show the corresponding soft-decision-FEC (SD-FEC) and hard-decision-FEC (HD-FEC) limits, respectively.

implementation. However, it should be noted that the offered advantages of the scaling factor are also applicable to other modulation formats too. It should also be noted that the scaling factor p is only different from 1 in the first iteration, therefore the condition for global minimum convergences is always satisfied, see subsection 3.2.1.

3.4 Performance Assessment in Presence of Noise

This section shows the simulation analysis of the proposed method in the presence of noise using an in-house C++/MATLAB simulator, named NetXpto-LinkPlanner, developed by the researchers and Ph.D. students of the Instituto de Telecomunicações over the years. At the transmitter, the signal is modulated using a Mach-Zehnder IQ modulator operating in its linear regime. For optical signal transmission, we chose a standard single-mode fiber (SSMF) with an attenuation of 0.2 dB/km, the chromatic dispersion of 17 ps/nm/km, and nonlinear coefficient γ = 0.0014 $\mathrm{W^{-1}m^{-1}}$. Inside the fiber, the waveform evolution is calculated by using the split-step Fourier method with a step-size of 1 km, taking into consideration that we are operating in a quasi-linear regime. Also, we limit the launch power to 3 dBm for a quasi-linear operation regime. As we have considered short-reach links, the polarization mode dispersion (PMD) effects are negligible [17]. Since no optical pre-amplifier is used prior to photodetection, the incident optical power on the photodetector is low and the shot noise contribution is negligible, thus making the system performance essentially limited by the thermal noise. For the analysis, we have considered the input-referred noise current spectral density of 30 $\mathrm{pA}/\sqrt{\mathrm{Hz}}$ [17] and an ADC with 8-bit vertical resolution. Notice that, the ADC noise is also negligible considering the thermal noise in the receiver.

Fig. 3.9 shows the EVM of the recovered QPSK and 16QAM signals after 20 km of SSMF for different CSPR values. It shows that SSBN becomes more severe and degrades the quality of the recovered signal at low CSPR ratios. Contrarily, very high CSPR would deteriorate the signal to noise ratio (SNR) (sensitivity penalty) at the receiver end, which limits the system performance. Fig. 3.9 shows that irrespective of the modulation formats, EVM is decreasing

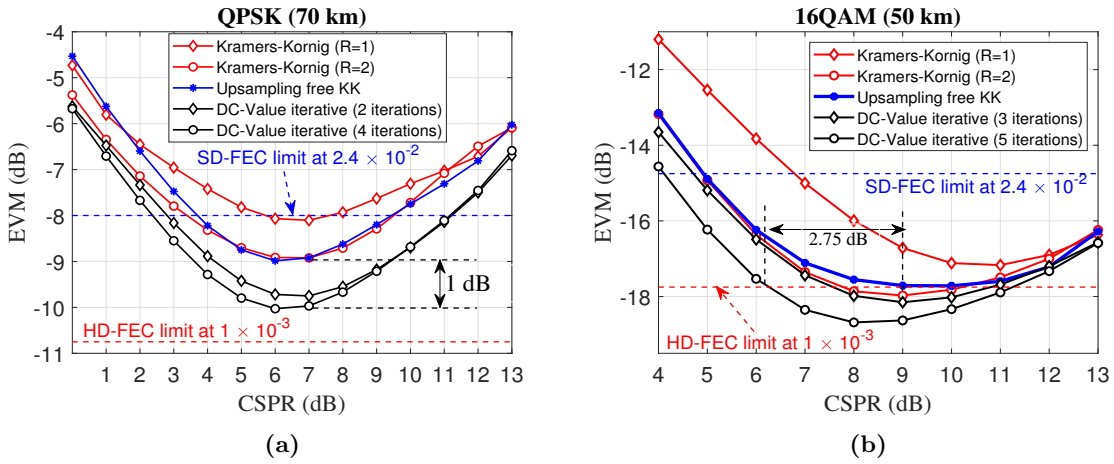

Figure 3.10: EVM of the recovered signal for the (a) QPSK (70 km), and (b) 16QAM (50 km) signals with 3 dBm transmitted power. R denotes the upsampling factor used in the KK method. Blue and red dashed lines show the corresponding SD-FEC and HD-FEC limits, respectively.

after each iteration. The iterative method based on the linear filtering discussed in [18] works by calculating SSBN terms and subtracting them from the detected signal. However, due to the inaccuracy of the SSBN approximation caused by the introduction of additional distortion by the linear filters, this method has the drawback of limited effectiveness. It is shown that KK provides better SSBN compensation effectiveness over iterative linear filtering methods [18]. Therefore, we present a comparative analysis of the proposed DC-Value method with the KK [7] and the upsampling free KK [4] methods. Fig. 3.10 shows the EVM of the recovered signal by the KK, the upsampling free KK, and the proposed DC-Value methods for the QPSK and 16QAM signals after 70 km and 50 km SSMF, respectively. We compare the obtained results of the KK (R = 1 and R = 2) [7] , upsampling free KK [4], and the proposed DC-Value method. Fig. 3.10(a) shows that ~1 dB EVM gain is achieved over KK (R = 2) and upsampling free KK (R = 1) after the 4 iterations. Similarly, in 16QAM (see Fig. 3.10(b)), the DC-Value method requires ~2.75 dB less CSPR to surpasses the accuracy of the KK (R = 2) and upsampling free KK with 3 iterations.

3.4.1 Computational Complexity Analysis

In this subsection, we analyze the computational complexity of the proposed method and present a comprehensive comparison with the KK [7] and the iterative linear filter [18] methods. Considering a DSP chip low clock frequency, f_{clock}, parallelization is employed to realize a high sampling frequency, f_s. The degree of parallelization is determined by the $N = \lceil f_s/f_{clock} \rceil$, where $\lceil \bullet \rceil$ is the ceiling operator. Considering the ADC with an 8-bit resolution, it requires 4 kbits memory to fill each look-up-table (LUT) with 2-byte floating-point number ($2^8 \times 2^4$). For an efficient FFT implementation, we set the degree of parallelization to $N = 2^m$, where $m > 1$. The KK requires digital signal upsampling and downsampling, which can be realized by an N_s tap finite impulse response (FIR) filter. The Hilbert transformation in the KK method can be implemented using an FIR filter having N_h taps. This Hilbert filter requires $N_h/2$ real-valued adders and $N_h/2$ real-valued multipliers [3]. Fig. 3.11(a) shows the schematic of the hardware implementation for the proposed DC-Value method. First, a serial-to-parallel (S2P)

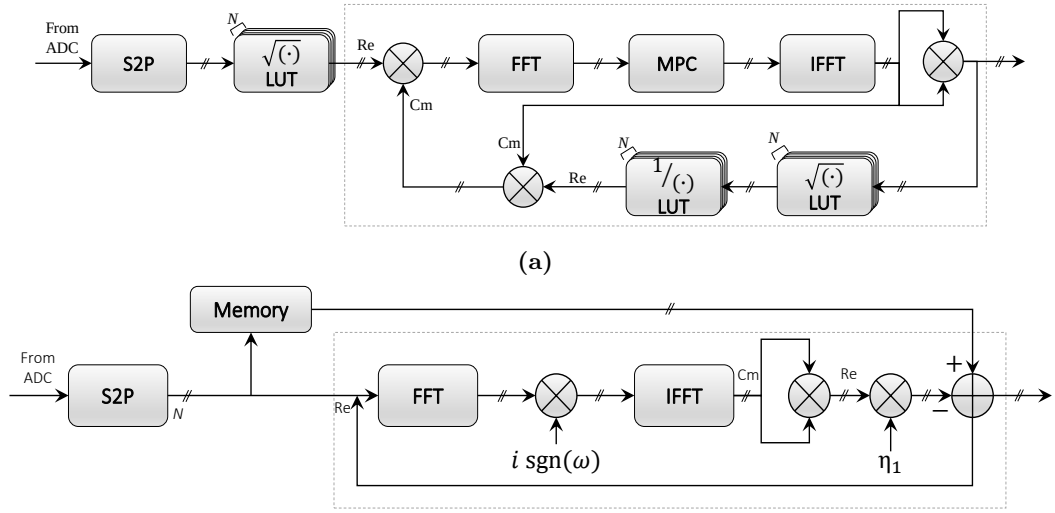

Figure 3.11: Hardware implementation scheme of (a) DC-Value method, (b) iterative linear filter. S2P: Serial-to-parallel, MPC: Minimum phase condition, SF: Sideband filter Re: Real signal, Cm: Complex signal, N: Number of points (Parallelization), dotted boxes show the iterations.

Table 3.2: Computational Complexity Comparison

	Kramers-Kronig [7]	**Iterative linear filter [18]**	**DC-Value [18]**
Multiplier	$(3N_s + N_h/2 + 2)\mathrm{R}N$	$(4N\log_2 N + 3N)k$	$(4N\log_2 N + 6N)k$
Adder	$(3N_s + N_h/2)\mathrm{R}N$	$(4N\log_2 N + N)k + N$	$(4N\log_2 N + N)k$
Memory	$16\mathrm{R}N^{\dagger}$	$8N^{\varrho}$	$12N^{\dagger}$

*k: Number of iterations; *R: Upsampling factor; †: kbits; $^{\varrho}$: bits

process is carried out to realize the parallelization, followed by a square-root operation. Next, the magnitude is multiplied with the complex phase correction factor which requires $2N$ real multiplications. Following that, FFT is calculated requiring $\frac{N}{2}\log_2 N$ complex multiplications (i.e. 4 real multiplications and 2 real additions) and $N\log_2 N$ complex additions (i.e. 2 real additions). For the minimum phase condition, the scaling factor implementation can be implemented by 1-bit shift operation. Afterward, inverse fast Fourier transform (IFFT) requires the same complexity as FFT. Next, the phase correction factor is calculated by taking $|(\bullet)|^2$ (i.e. $2N$ real multiplications and N addition), followed by a square-root, an inverse, and a multiplication (i.e $2N$ real multiplication) operation. Similarly, we estimate the complexity of the iterative linear filter method shown in Fig. 3.11(b). In iterative linear filter method, the sideband filter includes a multiplication by 2 operation which can be implemented by 1-bit shift operation. The estimated computational complexity comparison of three methods (the KK [7], the iterative linear filter [18], and the proposed DC-Value method) is presented in Table 3.2.

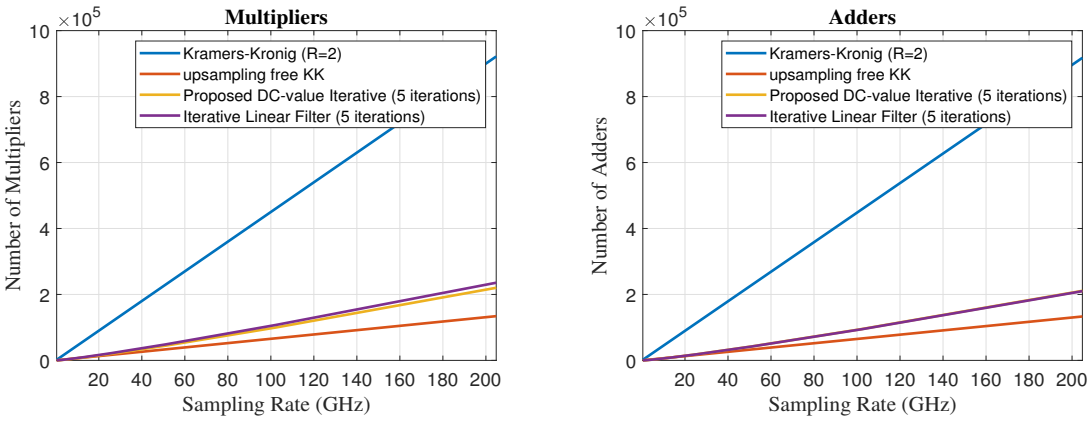

Figure 3.12: Computational complexity required in terms of (a) number of multipliers, and (b) number of adders, by different phase reconstruction. 5 iterations are considered for iterative methods.

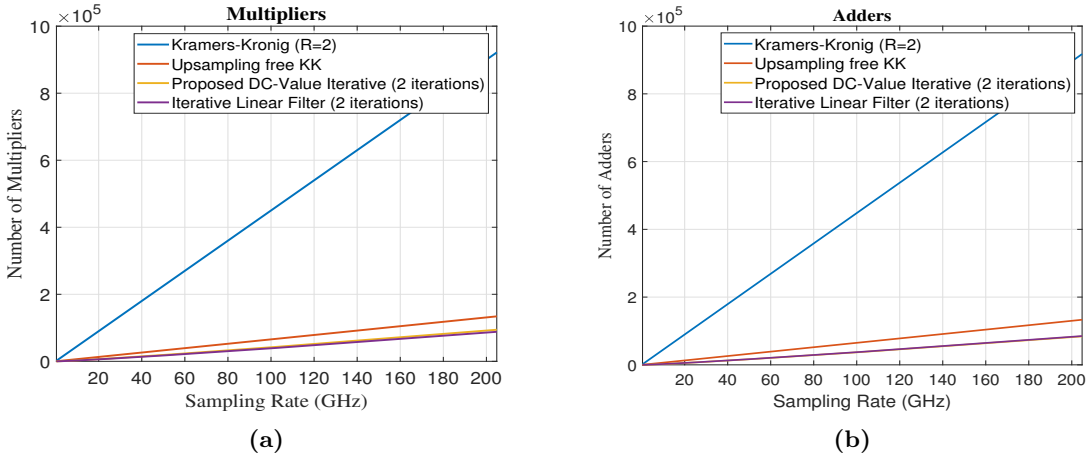

Figure 3.13: Computational complexity required in terms of (a) number of multipliers, and (b) number of adders, by different phase reconstruction. 2 iterations are considered for iterative methods.

The required computational complexity increases linearly with the sampling frequency f_s since a higher degree of parallelization N is required to to realize high f_s when f_{clock} is fixed. Considering both N_h and N_s with 128 taps, R = 2, k = 5, and f_{clock} = 200 MHz, the computational power required in terms of number of multipliers and adders by the different phase reconstruction methods is shown in Fig. 3.12. Considering N = 256, it shows that the KK method requires ~10^5 real-valued adders and multipliers, where this number would be reduced to ~4.5×10^4 for both iterative linear filter method and proposed DC-Value method, respectively. Similarly, by considering k = 2, the number of multipliers and adders operations required would be reduced to ~1.7×10^4 as shown in Fig 3.13. Despite the FFT/IFFT pairs are involved, the proposed method exhibits low latency since it requires less number of multipliers and adders operation when compared with the KK algorithm. Also, the proposed DC-Value method enables higher accurate reconstruction with low CSPR requirement (no extra receiver sensitivity penalty unlike [3]) without the need for digital upsampling.

3.5 Final Remarks

In this chapter, using the SSB and DC-Value properties of the minimum phase signal, we have proposed a novel DC-Value method that reconstructs the full electric field minimum phase signal from its amplitude information in direct detection optical systems. The proposed reconstruction technique does not contain nonlinear operations. This ensures an upsampling free reconstruction process at low tone power (low CSPR) operation. Moreover, we have shown that a constant scaling factor p used in the iterative process speeds up the convergence process. Also, we have performed a simulation analysis of a 100 Gb/s (120 Gb/s system with 20% overhead). Results show that the proposed technique provides ~1 dB EVM gain when compared with the KK method for a QPSK signal after 70 km of SSMF transmission. Besides, regarding the 16QAM signal, the proposed technique requires ~2.75 dB lesser tone power to surpass the accuracy of the other two methods, with as low as 3 iterations. The presented results show that the proposed technique presents salient features that can facilitate effective field reconstruction, making it a promising technique in the direct detection based optical communication systems.

References

[1] A. Oppenheim and R. Schafer, "Digital Signal Processing," *Pearson*, 1975.

[2] C. Füllner, M. M. H. Adib, S. Wolf, *et al.*, "Complexity Analysis of the Kramers–Kronig Receiver," *IEEE/OSA Journal of Lightwave Technology*, vol. 37, no. 17, pp. 4295–4307, 2019.

[3] T. Bo and H. Kim, "Toward Practical Kramers-Kronig Receiver: Resampling, Performance, and Implementation," *IEEE/OSA Journal of Lightwave Technology*, vol. 37, no. 2, pp. 461–469, 2019.

[4] T. Bo and H. Kim, "Kramers-Kronig Receiver Without Digital Upsampling," *Optical Fiber Communications Conference and Exhibition (OFC)*, pp. 1–3, 2018.

[5] T. Bo and H. Kim, "Kramers-Kronig Receiver Operable Without Digital Upsampling," *Optics Express*, vol. 26, no. 11, pp. 13 810–13 818, 2018.

[6] R. K. Patel, I. A. Alimi, N. J. Muga, *et al.*, "Optical Signal Phase Retrieval With Low Complexity DC-Value Method," *IEEE/OSA Journal of Lightwave Technology*, vol. 38, no. 16, pp. 4205–4212, 2020.

[7] A. Mecozzi, C. Antonelli, and M. Shtaif, "Kramers-Kronig Coherent Receiver," *Optica*, vol. 3, no. 11, pp. 1220–1227, 2016.

[8] X. Chen, C. Antonelli, S. Chandrasekhar, *et al.*, "Kramers–Kronig Receivers for 100-km Datacenter Interconnects," *IEEE/OSA Journal of Lightwave Technology*, vol. 36, no. 1, pp. 79–89, 2018.

[9] W. Shieh, H. Khodakarami, and D. Che, "Invited Article: Polarization Diversity and Modulation for High-speed Optical Communications: Architectures and Capacity," *APL Photonics*, vol. 1, no. 4, pp. 040–801, 2016.

[10] A. Mecozzi, C. Antonelli, and M. Shtaif, "Kramers-Kronig receivers," *Advances in Optics and Photonics*, vol. 11, no. 3, pp. 480–517, 2019.

[11] L. Blech, Y. Eldar, C. Antonelli, *et al.*, "The Enhanced Kramers Kronig Receiver," *Optical Fiber Communications Conference and Exhibition (OFC)*, pp. 1–3, 2018.

[12] M. Lyu, W. Shi, and L. A. Rusch, "SiP Alternative to Enhanced KK for OFDM," *European Conference on Optical Communication (ECOC)*, pp. 1–3, 2018.

[13] C. Sun, D. Che, H. Ji, *et al.*, "Towards Low Carrier-to-Signal Power Ratio for Kramers-Kronig Receiver," *Optical Fiber Communications Conference and Exhibition (OFC)*, pp. 1–3, 2019.

[14] S. An, Q. Zhu, J. Li, *et al.*, "Modified KK Receiver with Accurate Field Reconstruction at Low CSPR Condition," *Optical Fiber Communications Conference and Exhibition (OFC)*, pp. 1–3, 2019.

[15] S. An, Q. Zhu, J. Li, *et al.*, "Accurate Field Reconstruction at Low CSPR Condition Based on a Modified KK Receiver with Direct Detection," *IEEE/OSA Journal of Lightwave Technology*, pp. 485–491, 2019.

[16] T. Quatieri and A. Oppenheim, "Iterative Techniques for Minimum Phase Signal Reconstruction from Phase or Magnitude," *IEEE Transactions on Acoustics, Speech, and Signal Processing*, vol. 29, no. 6, pp. 1187–1193, 1981.

[17] J. K. Perin, A. Shastri, and J. M. Kahn, "Design of Low-Power DSP-Free Coherent Receivers for Data Center Links," *IEEE/OSA Journal of Lightwave Technology*, vol. 35, no. 21, pp. 4650–4662, 2017.

[18] Z. Li, M. S. Erkılınç, K. Shi, *et al.*, "SSBI Mitigation and the Kramers–Kronig Scheme in Single-Sideband Direct-Detection Transmission With Receiver-Based Electronic Dispersion Compensation," *IEEE/OSA Journal of Lightwave Technology*, vol. 35, no. 10, pp. 1887–1893, 2017.

Chapter 4

Experimental Validation of the DC-Value Method

The minimum phase signal based reception offers a suitable self-coherent (SCOH) solution for short-reach optical networks. In particular, the Kramers-Kronig (KK) and the DC-Value methods are state of the art signal reconstruction techniques which enable the minimum phase signal based SCOH transceiver. The analysis shows that the DC-Value method can address the higher sampling-rate requirement and sensitivity problems of the KK methods. Nevertheless, the DC-Value method still needs extensive validation.

In this chapter, an experimental setup and validation of the DC-Value method is presented for the short-reach optical link scenario. It includes the algorithm implementation details and performance analysis carried out employing advanced modulation formats like QPSK and 16QAM. It also presents a comparative performance assessment of the novel DC-Value method with the other state of the art signal reconstruction methods such as KK and upsampling-free KK methods.

This chapter comprises seven sections. Section 4.1 presents a general architecture of the minimum phase based SCOH transceiver. In section 4.2, the implementation details of signal reconstruction algorithms are discussed. In section 4.3, the details of the experimental setup are presented. In section 4.4, the experimental setup optimization process is presented considering the resource requirement and the transmission reach. In section 4.5, the performance analysis and discussion of the obtained experimental data is presented. Section 4.6 presents an advanced computational analysis of signal reconstruction algorithms. Finally, section 4.7 presents the concluding remarks.

4.1 General Architecture of the DC-Value Method Transceiver

In this section, we present a general architecture for the minimum phase signal based SCOH DC-Value transceiver. The underlying idea is that the signal should satisfy a minimum phase condition upon detection. This can be achieved by an SSB signal transmission with a high enough carrier to signal power ratio (CSPR) value. Here, we discuss two different techniques to generate an SSB signal with desired CSPR value. The first technique is the digital method, in which the carrier is inserted into the complex baseband signal in the transmitter digital

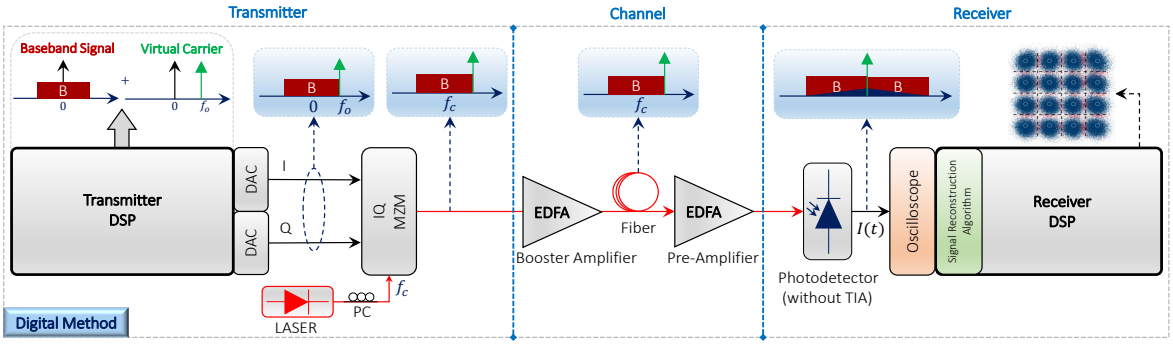

Figure 4.1: The general architecture of the minimum phase signal based SCOH DC-Value transceiver with a digital method to generate an optical single sideband (SSB) signal [1]–[5].

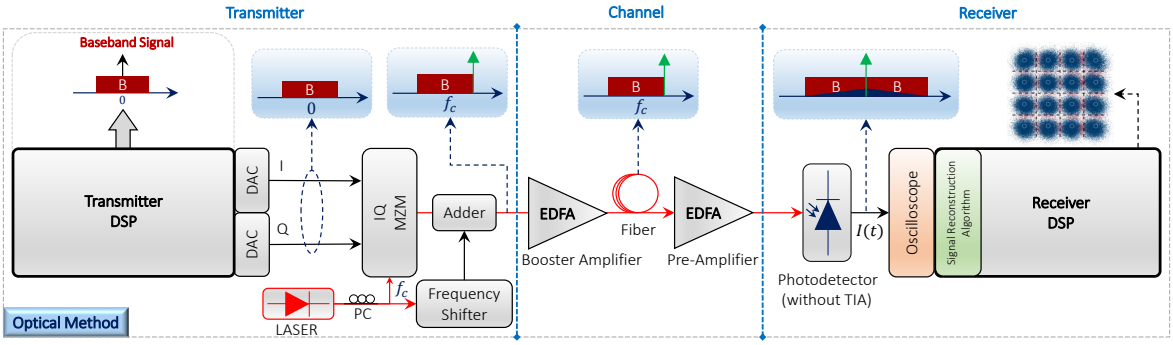

Figure 4.2: The general architecture of the minimum phase signal based SCOH DC-Value transceiver with an optical method to generate an optical SSB signal [1]–[5].

signal processing (DSP) stage. The second technique is the optical method, in which the carrier is inserted in the optical domain. In the following, we present a brief discussion about the general architecture of the SCOH transceiver in consideration of the digital and optical methods.

This transceiver architecture for the digital method is shown in Fig. 4.1. The complex baseband signal with bandwidth B can be generated at the transmitter side employing advanced modulation formats such as QPSK and QAM. Following that, a virtual carrier at a frequency of $f_o = \frac{B}{2}$ is added with a high enough power (notice that $f_o = -\frac{B}{2}$ is equally possible). Following that, the signal is passed through the digital to analog converter (DAC) and then optically modulated using an IQ Mach–Zehnder modulator (IQ-MZM). The IQ-MZM generates an SSB optical signal which is launched to an optical fiber after an optical amplification. The incoming signal is first amplified at the receiver end using an optical pre-amplifier and detected using a signal photodetector. The signal is then captured using a real-time oscilloscope and processed offline using a receiver DSP. In the receiver DSP, first, the full optical field of the signal is reconstructed using a signal reconstruction algorithm (such as the KK method, upsampling-free KK method, or DC-Value method) and then applied to the standard coherent receiver post-DSP for the symbol detection.

This transceiver architecture for the optical method is shown in Fig. 4.2. In this case, the complex baseband signal is first modulated using an IQ-MZM like in a standard coherent

transmitter. Further, a continuous wave (CW) tone at frequency $f_c + \frac{B}{2}$ is generated from the laser source using a frequency shifter. The power of a CW tone can be varied to achieve desired CSPR value. The output of an IQ-MZM and frequency shifter output is added using an adder (i.e. an optical coupler) that generates an SSB signal with the desired CSPR value. The rest of part channel and receiver are the same as we discussed in the digital method.

4.2 Implementation of the Signal Reconstruction Algorithms

So far, we have seen that there are three state of the art signal reconstruction techniques namely KK, upsampling-free KK, and the DC-Value method that can be used to reconstruct full minimum phase signal in the digital domain. These algorithms require the implementation of several techniques such as the Hilbert filter and minimum phase condition (MPC) in the signal reconstruction process. In this section, we present in-depth implementation details of those signal reconstruction algorithms in reference to the transmitted signal characteristics.

Consider $E(t)$ is the complex envelope of the SSB optical signal as

$$E(t) = E_o \, e^{i2\pi f_o t} + E_s(t) \tag{4.1}$$

where, $E_s(t)$ is the complex information signal, $E_o \, e^{i2\pi f_o t}$ represents a virtual carrier complex tone added digitally with amplitude E_o and frequency f_o. As mentioned earlier, the virtual carrier with negative f_o, i.e. $E_o \, e^{-i2\pi f_o t}$, that coincides with the left-edge of the information signal spectrum is equally possible. Any of these techniques can be employed to generate an SSB signal which acts as a minimum phase signal upon detection (see Fig. 4.3). The amplitude E_o of a digitally added complex tone can be varied to attain the desired CSPR. Therefore, to experimentally validate the signal reconstruction algorithms, it is required to generate a SSB signal with a carrier residing at the edge of the information spectrum with sufficiently high power (as mentioned in (4.1)). Here, we have used a positive carrier frequency residing at the right-edge of the information spectrum throughout this whole experimental analysis. It should be noted that when the negative carrier frequency is employed in an SSB signal, it requires modifications in the implementation of the signal reconstruction algorithms which

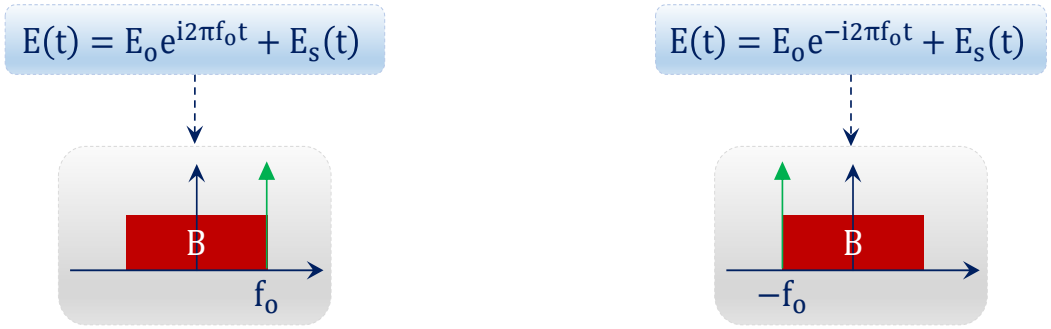

Figure 4.3: Spectrum representation of the SSB signal satisfying minimum phase condition upon direct-detection (DD) with (a) positive (coincides right-edge of the spectrum) and (b) negative (coincides left-edge of the spectrum) carrier frequency. Signal reconstruction algorithms implementation need to be modified based on the position of the carrier frequency.

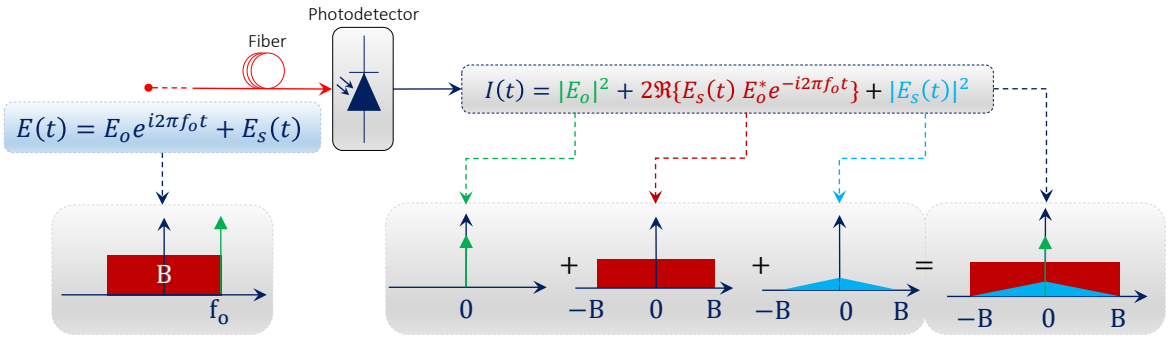

Figure 4.4: Spectrum representation of the components of the received minimum phase signal employing a single photodetector. Here, we have used a positive carrier frequency throughout the experimental analysis.

are discussed in the subsequent sections.

When the field $E(t)$ is detected using a single photodetector, the following photocurrent will be generated,

$$I(t) \propto R_{pd}|E(t)|^2 = R_{pd}\Big(\underbrace{|E_o|^2}_{\text{DC}} + \underbrace{2\Re\{E_s(t)\; E_o^* e^{-i2\pi f_o t}\}}_{\text{carrier-signal}} + \underbrace{|E_s(t)|^2}_{\text{signal-signal}}\Big) \tag{4.2}$$

where, R_{pd} represents the responsivity of the photodetector, and $\Re\{\bullet\}$ represents the real part of $\{\bullet\}$. The first term in (4.2) is the DC component (carrier-carrier beating), the second term is the desired carrier-signal beating, and the last term is the inherent signal-to-signal beating noise (SSBN) (see Fig. 4.4 for spectrum details). The current signal $I(t)$ is then sampled using an analog to digital converter (ADC) and supplied to the signal reconstruction algorithms to reconstruct the missing phase information. In the following subsections, we present a discussion of the implementation procedure of all signal reconstruction algorithms.

4.2.1 Implementation of the Kramers-Kronig Methods

The receiver DSP that exploits the conventional KK algorithm is shown in Fig. 4.5. Rather than considering SSBN terms as a perturbation that should be eliminated as in the case of other linearization approaches, the KK algorithm reconstructs the optical phase of the transmitted SSB signal based on its detected intensity via the Hilbert transform. This way it can

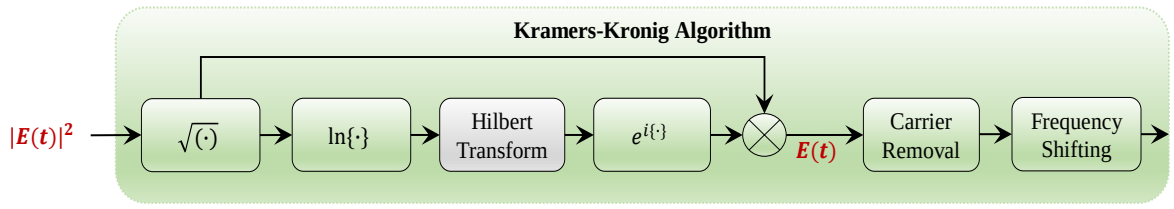

Figure 4.5: The algorithmic flow of the conventional KK method.

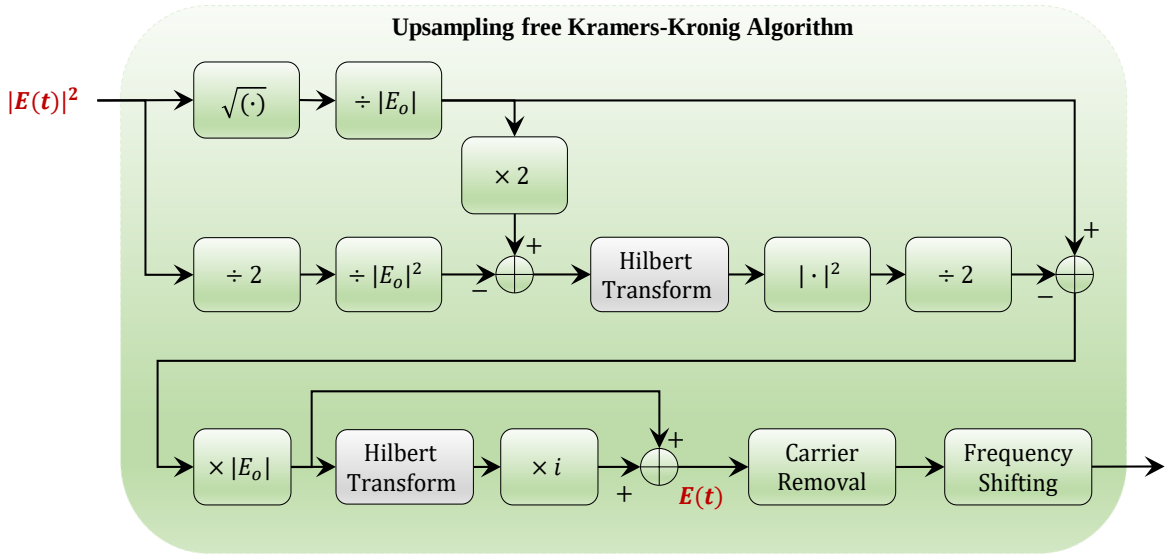

Figure 4.6: The algorithmic flow of the modified upsampling-free KK method.

effectively eliminates the SSBN perturbation.

It is noteworthy that out of all the linearization schemes being considered, the KK algorithm offers the best performance [6]. Nonetheless, as discussed earlier, one of the related technical challenges of the conventional KK scheme implementation is the requirement for the DSP block to function at a sampling rate that is faster than the one stipulated by Nyquist. This challenge is associated with certain required nonlinear operations like exponential and logarithm functions [7], [8]. This sampling rate problem in the conventional KK can be addressed by exploiting an upsampling-free KK algorithm as shown in Fig. 4.6 [8], [9].

It should be noted that both conventional and upsampling-free KK algorithms require the Hilbert transform operation. The Hilbert transform can be implemented either by transfer function or impulse response and its implementation needs to be modified based on the position of the optical carrier in the SSB signal. Therefore, from the algorithms implementation stand point, it is necessary to understand the Hilbert transform such that we can effectively utilize them in the KK algorithms. In Appendices A and B, we present a discussion about the Hilbert transformation and derive its impulse response that can be employed in the KK algorithms.

4.2.2 Implementation of the DC-Value Method

The working principle of the DC-Value method is based on iteratively imposing the SSB and DC-Value properties of the minimum phase signal, referred to as MPC, in the Fourier domain. The algorithmic flowchart is shown in Fig. 4.7, where MPC is imposed on the Fourier transformed signal $\tilde{E'}_n(\omega)$ to attain the next estimate of the minimum phase signal $\tilde{E}_n(\omega)$

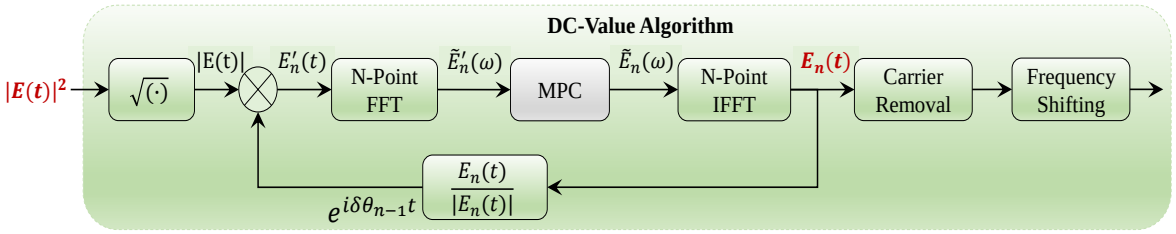

Figure 4.7: The algorithmic flow of the DC-Value method.

as [7],

$$\underbrace{\tilde{E}_n(\omega) = \begin{cases} p\tilde{E'}_n(\omega), & \text{for } \omega > 0 \\ N|E_o|, & \text{for } \omega = 0 \\ 0, & \text{for } \omega < 0 \end{cases}}_{\text{If negative } f_o \text{ virtual carrier added, i.e. } E_o e^{-i2\pi f_o t}} \qquad \underbrace{\tilde{E}_n(\omega) = \begin{cases} 0, & \text{for } \omega > 0 \\ N|E_o|, & \text{for } \omega = 0 \\ p\tilde{E'}_n(\omega), & \text{for } \omega < 0 \end{cases}}_{\text{If positive } f_o \text{ virtual carrier added, i.e. } E_o e^{i2\pi f_o t}} \tag{4.3}$$

where N represents the FFT length, an integer n is the iteration number, and p denotes the scaling factor given by,

$$p = \begin{cases} 2, & \text{for } n = 1 \\ 1, & \text{for } n > 1 \end{cases} \tag{4.4}$$

The process is repeated iteratively until desired accuracy achieved in the reconstruction of the minimum phase signal $E_n(t)$.

4.3 Experimental Setup for the DC-Value Method

In this section, we present the optical transmission test-bed to validate the proposed SCOH DC-Value method. It comprises a transmitter capable of transmitting advanced modulation format, a standard single-mode fiber (SSMF) link, and a single photodiode-based DD receiver with the associated DSPs for signal reconstruction. As already discussed, either digital or optical methods can generate an SSB signal for minimum phase-based SCOH transmission. However, the optical method presents an additional optical complexity as it requires a frequency shifter and an optical coupler. On the other hand, the digital method can leverage the DSP techniques to generate an SSB signal without additional optical complexity. Therefore, we use the digital method for the transmission throughout this whole experimental analysis.

Transmitter

At the transmitter side, see Fig. 4.8(a), a single-channel 30 Gbaud QPSK and 24 Gbaud 16QAM signals are generated using a root raised cosine (RRC) pulse shaping filter with 0.1 roll-off factor, respectively. Following that, a complex tone $E_o e^{2\pi f_o t}$, at a frequency of f_o = 16.5 GHz (considering 0.1 RRC roll-off factor, 1.1×30 Gbaud/2 = 16.5 GHz), is added to the 30 Gbaud QPSK signal, $E_s(t)$, in the digital domain (similarly, complex tone at f_o = 13.2 GHz is added to the 24 Gbaud 16QAM signal). The desired CSPR is obtained by varying the amplitude E_o of the complex tone. After transmitter digital signal processing

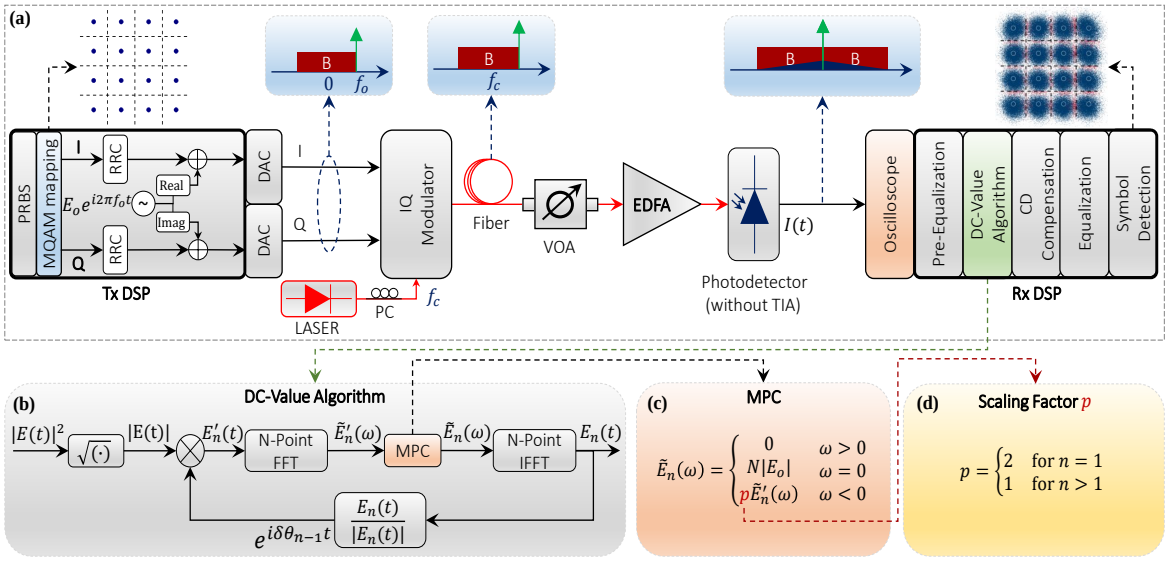

Figure 4.8: The experimental setup used for a virtual carrier assisted SCOH transceiver employing the DC-Value method. **Tx-DSP:** Transmitter DSP, **PRBS:** Psuedo-Random Bit Sequence, **RRC:** Root Raised Cosine, **DAC:** Digital to Analog Converter, **IQ MZM:** IQ Mach-Zehnder Modulator, **PC:** Polarization Controller, **VOA:** Variable Optical Attenuator, **EDFA:** Erbium-Doped Fiber Amplifier, **TIA:** Trans-Impedance Am plifier, **CD:** Chromatic Dispersion, **Rx-DSP:** Receiver DSP.

(Tx-DSP), the Keysight M8194A arbitrary waveform generator (AWG) containing 120 GSa/s DAC is used to generate the signal. The output of the DAC is modulated at 1550 nm using a single polarization IQ-MZM. The output of the IQ-MZM signal is directly launched to the SSMF.

Receiver

Following SSMF, the optical signal is amplified by an erbium-doped fiber amplifier (EDFA) and detected using a low-cost 40 GHz single photodetector without trans-impedance amplifier (TIA). The photodetector output is then sampled by a 100 GSa/s Tektronix real-time oscilloscope (RTO) with 33 GHz bandwidth. Finally, the experimental data captured by the RTO is processed offline using MATLAB software.

In the DC-Value method, first, a square-root operation is carried out to obtain the magnitude $|E(t)|$ of the optical field and multiplied by a phase correction factor $e^{i\delta\theta_{n-1}(t)}$ which outputs the signal $E'_n(t)$. In the first iteration ($n = 1$), the phase correction vector is assumed to be zero, i.e. $\delta\theta_0(t) = 0$. Next, the MPC is imposed (see Fig. 4.8(c)) on the Fourier transformed signal $\tilde{E'}_n(\omega)$ to attain $\tilde{E}_n(\omega)$ as discussed in (4.3). The scaling factor p used in the MPC greatly speeds up the convergence process (see Fig. 4.10). After imposing MPC, the inverse fast Fourier transform (IFFT) of the $\tilde{E}_n(\omega)$ is computed to obtain the first estimate of the minimum phase signal $E_1(t)$. The phase correction vector corresponds to $E_1(t)$ and can be calculated as $e^{i\delta\theta_1(t)} = \frac{E_1(t)}{|E_1(t)|}$. This phase estimation is then supplied as an updated phase correction vector for the subsequent iteration ($n = 2$). This process continues until the desired accuracy is reached. For noiseless scenario, when $n \to \infty$, it provides near perfect

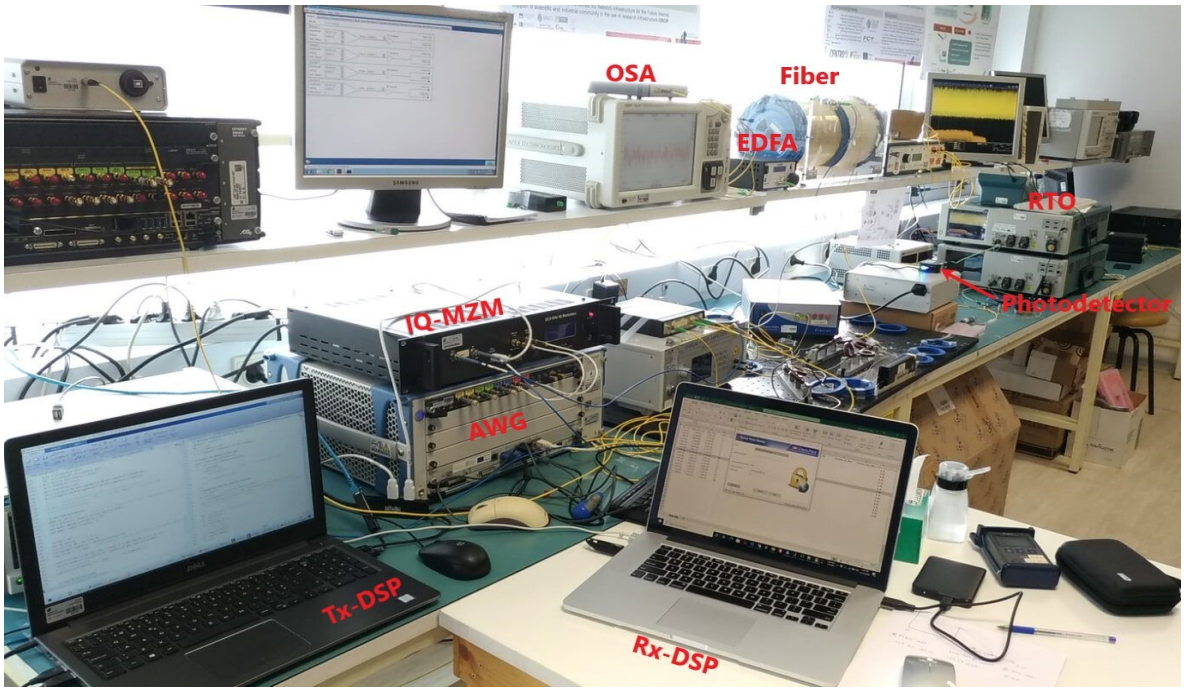

Figure 4.9: Experimental Setup.

reconstruction of the minimum phase signal i.e. $E_n(t) \rightarrow E_o + E(t)\ e^{-i2\pi f_o t}$. In practice, the algorithm saturates after several iterations (see Fig. 4.10) depending on the level of noise incurred from the photodetector.

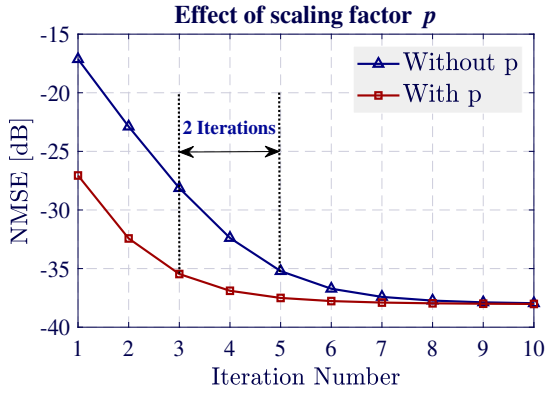

Figure 4.10: Effect of employing scaling factor p in the DC-Value method. Results correspond to the 30 Gbaud QPSK signal after 80 km SSMF.

Also, the normalized mean squared error (NMSE) between the known magnitude $|E(t)|$ and the estimated magnitude $|E_n(t)|$ is monotonically decreasing after each iteration and has a lower bound to zero (see Fig. 4.10), therefore, the reconstruction process converges [7]. Afterwards, the reconstructed minimum phase signal $E_n(t)$ is passed through the DC remover and then upconverted by multiplying $e^{i2\pi f_o t}$. Finally, the chromatic dispersion compensation and equalization can be carried out before symbol recovery.

4.4 Experimental Setup Optimization

In this section, we present an optimization of the opto-electronics components used in the experimental setup. The setup is optimized considering the required opto-electronics components and transmission reach. We start with the analysis of the back-to-back scenario and assess the experimental results.

4.4.1 Back-to-Back Analysis

The diagram displayed in Fig. 4.11 presents the experimental setup employed for the back-to-back analysis. At the transmitter side, a signal that satisfies the minimum phase condition upon detection corresponding to 30 Gbaud QPSK is generated with the help of a virtual carrier. For the assessment process, the CSPR values ranging from 3 to 15 dB are employed in the transmission process by varying the amplitude of the virtual carrier, respectively. The output voltage swing of the AWG (or DAC) is set to 200 mV_{pp}. Here V_{pp} stands for peak to peak voltage. At the transmitter side, the optical signal generated by the IQ-MZM is directly connected to the variable optical attenuator (VOA). The attenuation of the VOA is set to 0 dB in the back-to-back analysis. The output of the VOA is connected to the optical EDFA to boost the power of the optical signal before detection. Since the maximum allowed input power to the photodetector is ~10 dBm, the EDFA is operated in constant power mode such that it produces a constant ~3 dBm power at the output.

At the receiver end, following a single photodetector, the signal captured by RTO is used for offline processing to assess the system performance. The pre-equalization block refers to compensating for the non-flat response of the photodetector (discussed comprehensively in the section 4.4.3). Subsequently, three signal reconstruction techniques namely KK, up-sampling free KK, and DC-Value methods are employed for the signal reconstruction process respectively and followed by the post-DSP for symbol detection. The performance of all three signal reconstruction techniques are compared using a bit error rate (BER) metric as a function of CSPR. Results shown in Fig. 4.12 presents the performance analysis of the proposed SCOH transceiver setup considering this back-to-back configuration. Here, 2 samples per symbol DSP is employed for assessment purpose. It is shown that the proposed DC-Value

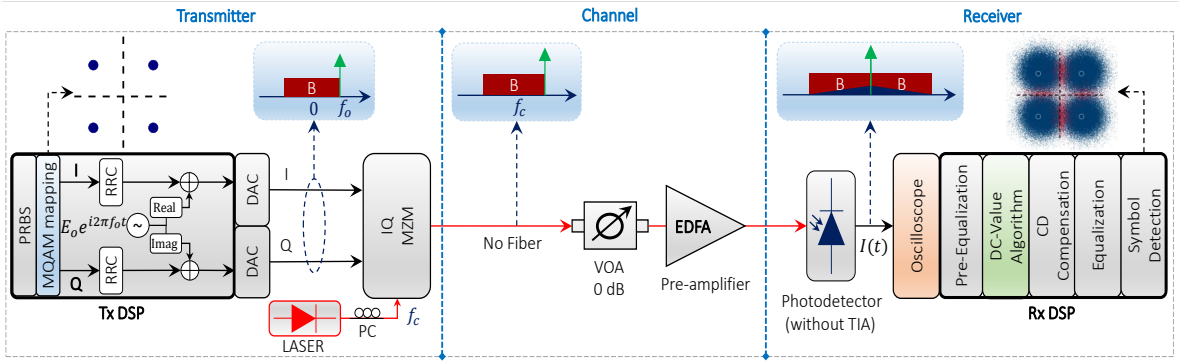

Figure 4.11: Experimental setup for the back-to-back analysis employing 30 Gbaud QPSK signal. The optical EDFA used in the setup helps to boost the optical power before detection. The maximum limit of the input optical power to the photodetector is ~10 dBm.

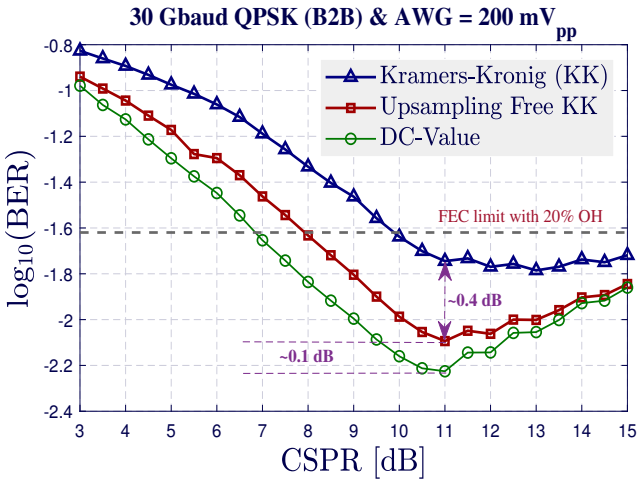

Figure 4.12: Experimental results of back-to-back analysis employing 30 Gbaud QPSK signal. For the assessment, 2 samples per symbol DSP employed in the signal reconstruction process (FEC limit @ 2.4×10^{-2} with 20% overhead [10]).

method outperforms both KK methods in terms of reconstruction accuracy and required CSPR. The DC-Value method provides approximately ~0.4 dB BER improvement when compared to the conventional KK method. Also, the DC-Value method provides ~0.1 dB BER improvement when compared to the upsampling free KK method.

4.4.2 Power Budget Analysis

This section presents a power budget analysis of the given setup considering the short-reach applications scenario. In the last section 4.4.1, we explained that only one optical EDFA employed before detection. In this regard, the placement of an EDFA, whether used as a booster amplifier or pre-amplifier, plays an essential role in the network. Here, we present an analysis that considers an EDFA as a booster amplifier and pre-amplifier, respectively, and calculated power budget in both scenarios.

EDFA as a Booster Amplifier

In this configuration, we place an EDFA at the transmitter side followed by an IQ-MZM as shown in Fig. 4.13. To calculate the power budget, the VOA is employed in the experimental setup that helps to attenuate the signal power by varying its attenuation. First, the output power of a booster amplifier is set to ~3 dBm, and it is connected to the VOA. In the experiment, a 30 Gbaud QPSK signal is employed for the assessment. Here, we vary the attenuation of the VOA from 1 to 10 dB with a step size of 1 dB. Results shown in Fig. 4.14 present the given setup's power budget analysis considering an EDFA as a booster amplifier in the link. Results show that the booster amplifier with ~3 dBm output power provides a ~4.5 dB attenuation budget that loosely translates into 22.5 km transmission reach with an SSMF. Further, the power budget can be improved 3 dB by increasing the booster amplifier output power to ~6 dBm. The increased booster output power can extend reach up to 37.5 km

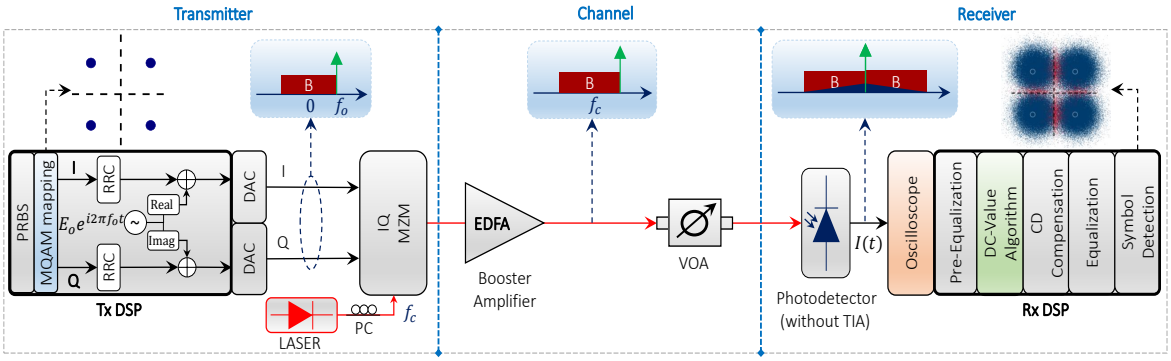

Figure 4.13: Experimental setup for the power budget analysis considering an EDFA as a booster amplifier. In the analysis, 30 Gbaud QPSK signal was employed for the assessment.

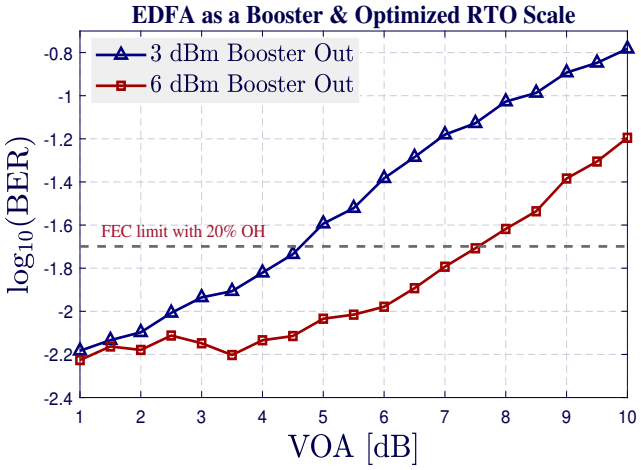

Figure 4.14: Experimental results of power budget analysis considering an EDFA as a booster amplifier. The analysis carried out considering a constant ~3 dBm and ~6 dBm output power from the booster amplifier, respectively (FEC limit @ 2.4×10^{-2} with 20% overhead).

considering an SSMF. Here, We limit the maximum power output of the booster to 6 dBm considering the nonlinear optical fiber channel.

EDFA as a Pre-Amplifier

In this configuration, we place an EDFA at the receiver side followed by a VOA, as shown in Fig. 4.15. The attenuation of a VOA can be varied to calculate the power budget of the given configuration. At the transmitter side, signal launched power can be adjusted by carefully increasing the modulation depth of the IQ-MZM. The modulation depth can be increased by increasing the AWG peak-to-peak output voltage. It should be noted that the pre-amplifier is operated in the constant power mode, and its output power is set to ~3 dBm. In the beginning, the output voltage of the AWG is set to 200 mV_{pp} and applied to the IQ-MZM to generate an optical signal. The output of the IQ-MZM is supplied to the VOA and then connected to a pre-amplifier. The attenuation of the VOA is varied from 1 to 20 dB, respec-

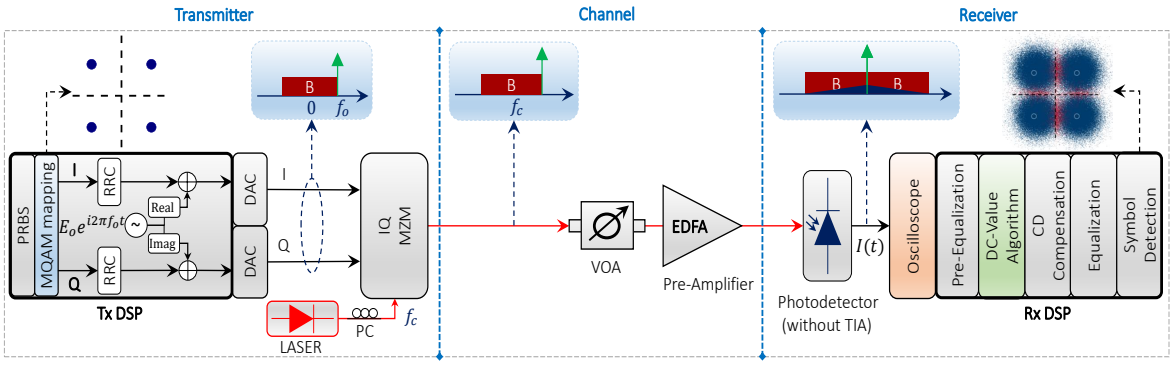

Figure 4.15: Experimental setup for the power budget analysis considering an EDFA as a pre-amplifier. The launch power is adjusted by increasing modulation depth of an IQ-MZM.

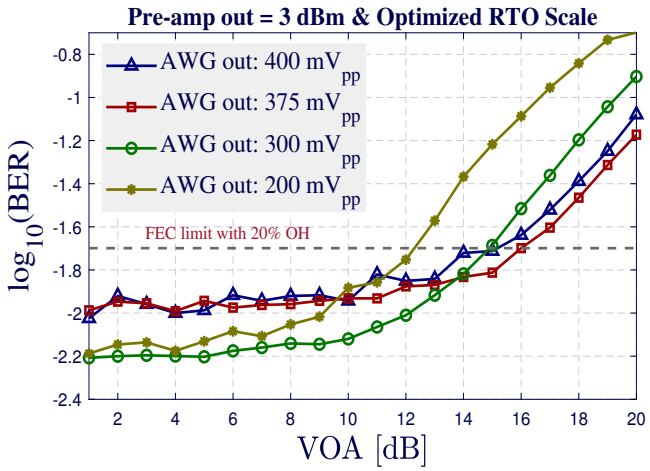

Figure 4.16: BER versus VOA attenuation in dB. The analysis carried out considering a constant ~3 dBm output power from the pre-amplifier (FEC limit @ 2.4×10^{-2} with 20% overhead).

tively and assess the system performance using the BER metric. Further, the output voltage of an AWG is increased to 300 mV_{pp}, and the whole process is repeated to assess the system performance. Similarly, the system performance is measured by increasing AWG output to 375 mV_{pp} and 400 mV_{pp}, respectively.

Results shown in Fig. 4.16 presents the power budget analysis considering an EDFA as a pre-amplifier. The trend in Fig. 4.16 shows that the carefully increased modulation depth provides better system performance until IQ-MZM operated in a highly nonlinear regime. The system provides 12 dB power budget for 200 mV_{pp} AWG output, which translates into 60 km transmission reach considering an SSMF. The increased value of AWG output to 300 mV_{pp} and 375 mV_{pp} provide approximately 15 and 16 dB power budget (around 75 km and 80 km), respectively. Further increasing AWG output drives the IQ-MZM in a nonlinear regime and degrades the system performance. Looking at the system performance, we use an EDFA as a pre-amplifier throughout this whole experimental analysis.

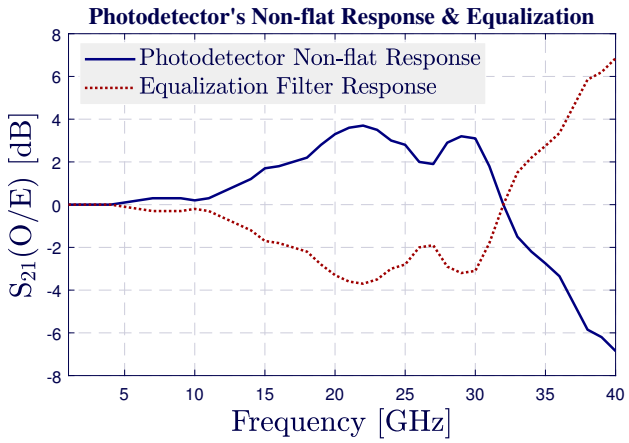

Figure 4.17: The optical to electrical (O/E) S_{21} response of the photodetector and it's equalization in the digital domain.

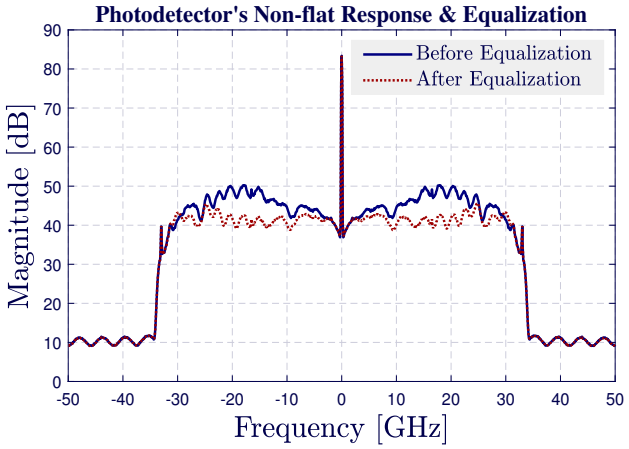

Figure 4.18: Photodetector output signal before and after equalization.

4.4.3 Photodetector's Non-flat Response Equalization

At the receiver end, the Optilab PD-40-M photodetector is employed in the experimental setup for signal detection. It is a 40 GHz bandwidth PIN receiver module utilized in the experimental analysis. The PD-40-M can accept input power up to 10 mW and provides optical to RF conversion out to the frequency range around 40 GHz. The optical to electrical (O/E) S_{21} response of the given photodetector is displayed in Fig. 4.17 (S_{21} data is provided by the manufacturer). Here, we use an equalization filter in the digital domain that compensates for the non-flat S_{21} response of the photodetector. Results shown in Fig. 4.18 present the magnitude spectrum of the signal before and after applying the equalization filter. The effectiveness of the equalization depends on the bandwidth of the signal. For the given Optilab PD-40-M photodetector, equalization may improve overall system performance if we use higher than 24 GHz bandwidth.

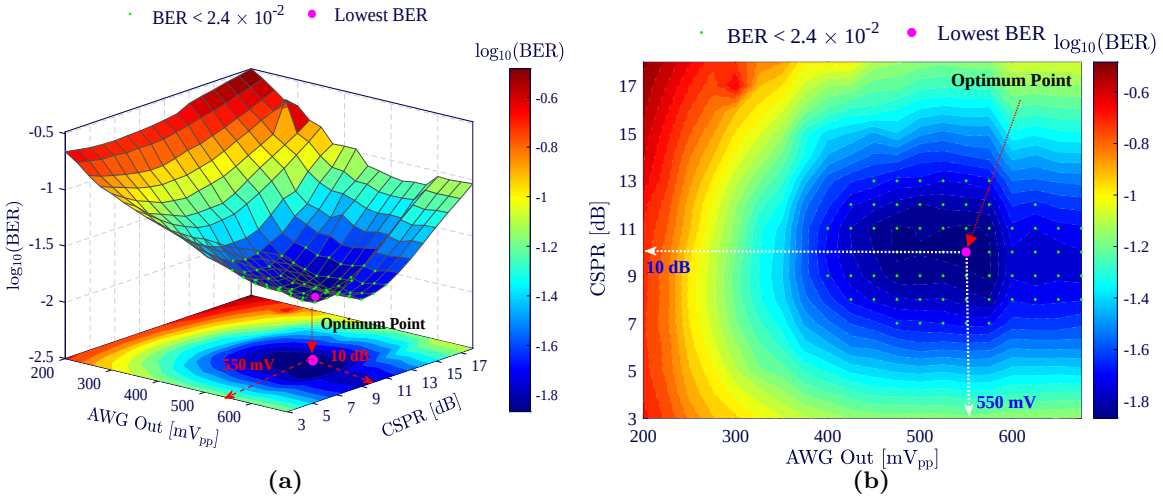

Figure 4.19: After transmission of 80 km SSMF, performance analysis of 30 Gbaud QPSK as a function of CSPR and modulation depth employing DC-Value method (a) 3D view (b) 2D view.

4.5 Results and Discussion

Here, we discuss the obtained results from the experimental setup presented in section 4.3. In the beginning, the experimental setup is optimized as discussed in section 4.4, and then collected experimental data employing an advanced modulation format signal transmission. For the given SCOH experimental setup, the signal must satisfy the minimum phase condition upon reception, and it can be achieved by adding a virtual carrier. The amplitude of the virtual carrier can be varied to attain a desired CSPR value in the transmission. Here, in this experimental analysis, we vary the CSPR values from 3 to 18 dB and measure the system performance, respectively. In the experiment, the transmission of advanced modulation formats such as QPSK and 16QAM are employed for the performance assessment. In the following, we present the obtained results for QPSK and 16QAM transmission.

QPSK: 30 Gbaud

Since no booster amplifier is employed in the link, the launch power is adjusted by carefully increasing the modulation depth (by increasing AWG peak-to-peak output voltage) of the IQ-MZM. For 30 Gbaud QPSK transmission, the AWG output is varied from 200 mV_{pp} to 675 mV_{pp} with a step size of 25 mV_{pp}. Fig. 4.19 shows the analysis of $\log_{10}$(BER) with respect to modulation depth and CSPR after 80 km SSMF (2 spans of 40 km each). This analysis helps in identifying an optimum value of the CSPR and AWG peak-to-peak output. It should be noted that the attenuation of the VOA is set to 0 dB. The obtained results as a function of CSPR and modulation depth are plotted in Fig. 4.19. The results shown in Fig. 4.19 indicate that the system performance gets deteriorated at both extreme points of CSPR and modulation depth. If CSPR is too low, then system performance is limited by SSBN perturbation. On the contrary, too high CSPR tends to induce receiver sensitivity penalty. Likewise, lowering the modulation depth results in low launched power which degrades the optical signal to noise ratio (OSNR) at the output of pre-amplifier. Also, pre-amplifier saturates in case of very low optical is received at the receiver end, and limits the

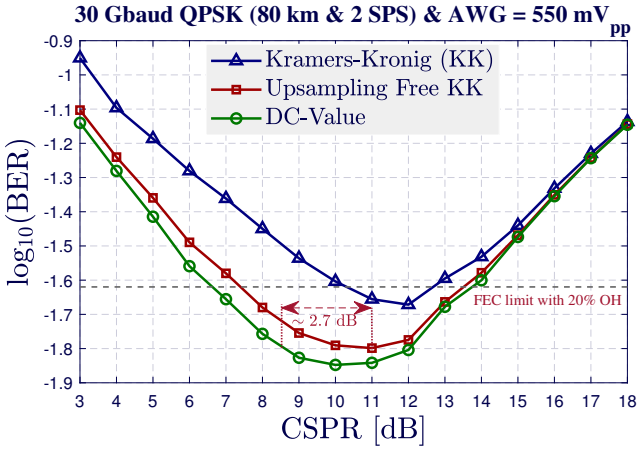

Figure 4.20: System performance as a function of CSPR at an optimum AWG operating point of 550 mV_{pp} employing three signal reconstruction methods. (FEC limit @ 2.4×10^{-2} with 20% overhead).

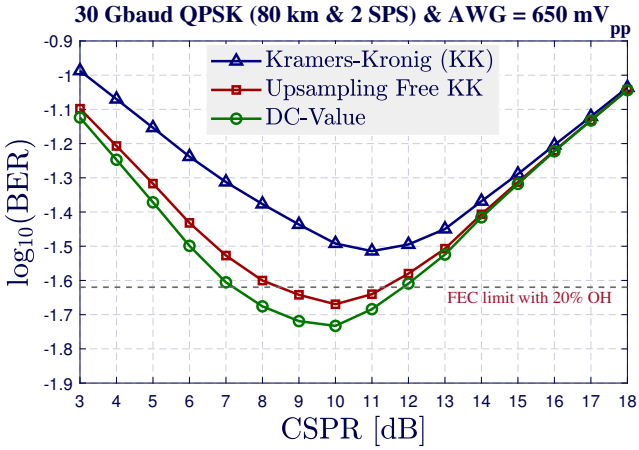

Figure 4.21: System performance as a function of CSPR for an increased modulation depth to 650 mV_{pp} employing three signal reconstruction methods. (FEC limit @ 2.4×10^{-2} with 20% overhead).

system performance. On the other hand, too high modulation depth causes an IQ-MZM to operate in a highly nonlinear regime which produces nonliterary in the system. Results shown in Fig. 4.19 demonstrate that the optimum operating point lies around AWG = 550 mV_{pp}, with a CSPR of ~10 dB. Further increasing the AWG output voltage (greater than 550 mV_{pp}) causes the modulation nonlinearities to act as a dominant source of noise and degrade the system performance [11].

Fig. 4.20 displays the performance of three different signal reconstruction methods, namely KK, upsampling-free KK [9], and the proposed DC-Value [7] (with 5 iterations) at the optimum AWG operating point of 550 mV_{pp} and 2 samples per symbol (SPS) DSP. Results in Fig. 4.20 show that the proposed DC-Value method requires ~2.7 dB less CSPR to achieve the same accuracy as an upsampling-free KK method and provides ~13% BER improvement. Further, when we increase the modulation depth higher than 550 mV_{pp}, the modulation non-

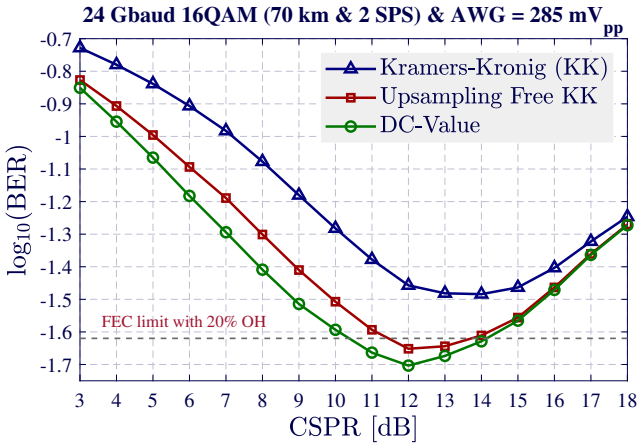

Figure 4.22: Performance of 24 Gbaud 16QAM system $\log_{10}$(BER) vs CSPR after 70 km (FEC limit @ 2.4×10^{-2} with 20% overhead).

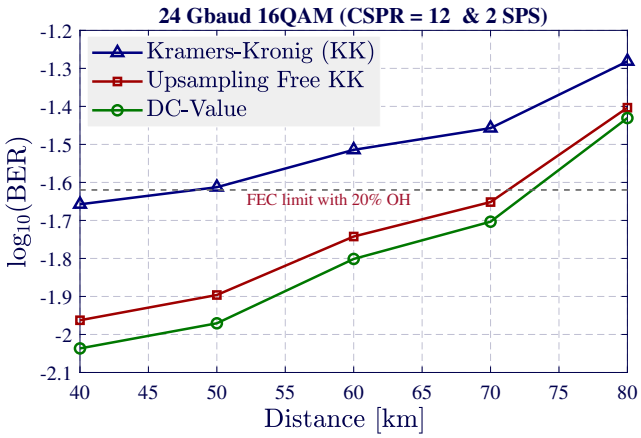

Figure 4.23: Performance of 24 Gbaud 16QAM system $\log_{10}$(BER) vs Distance at the optimum point (AWG = 285 mV_{pp} & CSPR = 12 dB) (FEC limit @ 2.4×10^{-2} with 20% overhead).

linearities become a dominant source of noise and degrade the system performance. Results shown in Fig. 4.21 display the system performance for AWG operating at 650 mV_{pp}. It shows that the overall system performance is degraded by modulation nonlinearities for all three signal reconstruction methods proportionally.

16QAM: 24 Gbaud

For 24 Gbaud 16QAM transmission, a VOA is employed after 40 km SSMF (1 span) to mimic the extended length of the SSMF. Following a similar approach, the optimum operating point in the case of 24 Gbaud 16QAM transmission lies around 285 mV_{pp}, with a CSPR of ~12 dB. Fig. 4.22 displays the performance of all three signal reconstruction methods for the 24 Gbaud 16QAM transmission after 70 km. It shows that the DC-Value method requires ~1 dB less CSPR to achieve the same accuracy as the upsampling-free KK method, while

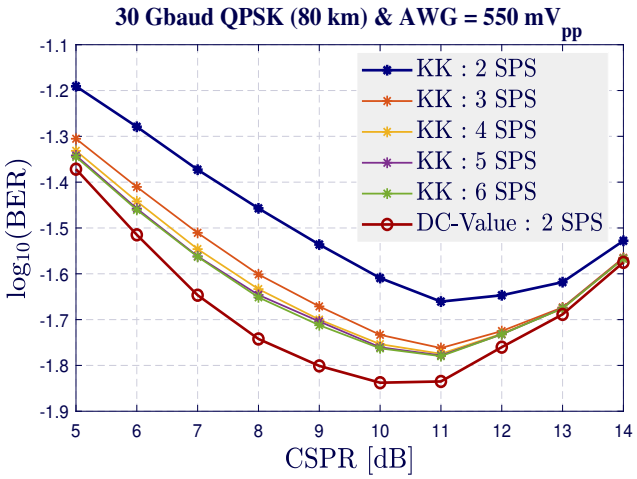

Figure 4.24: Analysis of the effect of SPS in the signal reconstruction methods. For KK method, the value of SPS varied from 2 to 6 in the analysis, while the DC-Value method is operated at fixed Nyquist sampling rate, i.e. 2 SPS.

the conventional KK method cannot support 70 km reach. Fig. 4.23 displays the system performance as a function of distance for the optimum operating conditions (285 mV_{pp} & CSPR = 12 dB). Results show that the conventional KK method can support up to 50 km reach at 2 SPS, while the upsampling-free KK and DC-Value method can extend this reach up to 70 km, with DC-Value being the most accurate signal reconstruction method, i.e. a 13.5% lower BER.

4.6 Advanced Analysis

This section presents an advanced analysis of the signal reconstruction algorithms. The conventional KK method requires higher SPS to accommodate the spectral broadening caused by nonlinear functions. To the contrary, the upsampling free KK and the DC-Value method can be operated at the Nyquist sampling rate (i.e. 2 SPS) without incurring an extra penalty in signal reconstruction. Here, we present the effect of SPS in the signal reconstruction process.

4.6.1 Effects of Samples Per Symbol

Fig. 4.24 shows the BER as a function of CSPR over various SPS values considering the conventional KK and the DC-Value methods. The value of SPS is varied from 2 to 6 with the step size of 1 in the KK method. Results shown in Fig. 4.24 present that the BER improves with an increase in the value of SPS. At a CSPR value of ~11 dB, which is approximately an optimum value, it is shown that the KK method improves performance by ~0.1 dB when SPS increases to 4. The performance of the KK saturates at 4 SPS, and no further gain is observed in the system performance when SPS is higher than 4.

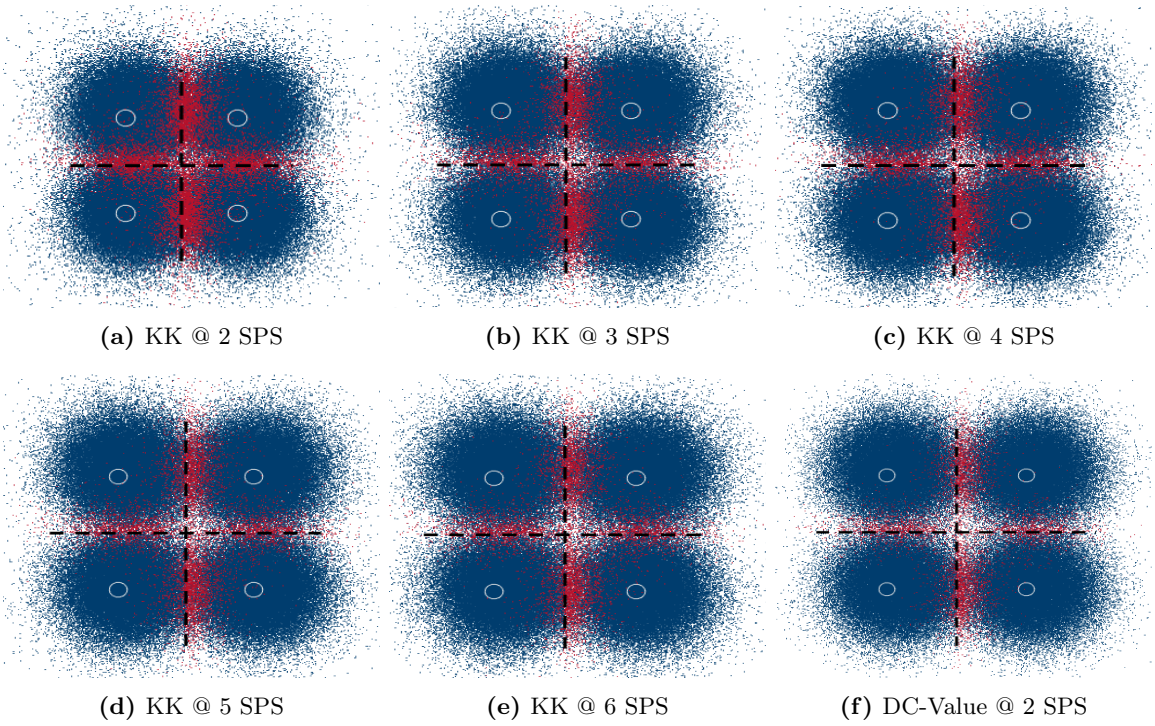

(a) KK @ 2 SPS **(b)** KK @ 3 SPS **(c)** KK @ 4 SPS

(d) KK @ 5 SPS **(e)** KK @ 6 SPS **(f)** DC-Value @ 2 SPS

Figure 4.25: Constellation of the recovered symbol of 30 Gbaud QPSK signal after transmission of 80 km. The results corresponds to ~11 dB CSPR in Fig. 4.24.

Further, results shown in Fig. 4.25 present the recovered constellations for the varying SPS in the KK reconstruction method and fixed 2 SPS for the DC-Value method. Constellations shown here correspond to an optimum CSPR value of ~11 dB for both KK and DC-Value methods. The result shown in Fig. 4.25(a) presents the recovered constellation employing the KK method with 2 SPS DSP in the signal reconstruction process. Fig. 4.25(a) shows that the recovered signal contains BER = 2.46×10^{-2} and Q = 5.88 dB. The performance tends to improve by increasing SPS in the KK reconstruction process. Results show that the performance improves up to 4 SPS and it saturates around afterwards. At 4 SPS, the BER = 1.76×10^{-2} and Q = 6.47 dB were observed in the KK reconstruction process. On the other hand, the DC-Value method can be operated at Nyquist sampling rate (i.e. 2 SPS) and it provides improved performance when compared to the KK method operating at higher SPS. The result shown in Fig. 4.25(f) presents the recovered constellation employing the DC-Value method. Fig. 4.25(f) shows that the recovered signal holds BER = 1.42×10^{-2} and Q = 6.78 dB. Overall, the DC-Value method can be operated at the Nyquist sampling rate without incurring much penalties, while the KK method tends to require digital upsampling in the reconstruction process.

4.7 Final Remarks

In this chapter, we presented an experimental setup for the validation of the proposed SCOH DC-Value method. To reduce implementation complexity and cost, we opted for the virtual

carrier assisted system where a virtual carrier tone is added in the digital domain. Also, we explained the implementation of the state of the art signal reconstruction methods like KK, upsampling-free KK, and the proposed DC-Value method. The experiment results show that the proposed DC-Value method can be operated at the Nyquist sampling rate, unlike the conventional KK method. Also, the experimental results show that the DC-Value method outperforms the upsampling-free KK method, enabling a significant reduction of CSPR (2.7 dB with QPSK and 1 dB with 16QAM). Additionally, the effect of SPS is analyzed where results show that the DC-Value method can be operated at the Nyquist sampling rate (i.e. 2 SPS) without incurring much penalties, while the KK method tends to require digital upsampling (around 4 to 5 SPS) in the reconstruction process.

References

[1] D. Che, Q. Hu, and W. Shieh, "Linearization of Direct Detection Optical Channels Using Self-Coherent Subsystems," *IEEE/OSA Journal of Lightwave Technology*, vol. 34, no. 2, pp. 516–524, 2016.

[2] X. Zhou, J. Huo, K. Zhong, *et al.*, "Single Channel 50 Gbit/s Transmission Over 40 km SSMF Without Optical Amplification and In-Line Dispersion Compensation Using a Single-End PD-Based PDM-SSB-DMT System," *IEEE Photonics Journal*, vol. 9, no. 5, pp. 1–11, 2017.

[3] Y. Zhu, M. Jiang, and F. Zhang, "Direct Detection of Polarization Multiplexed Single Sideband Signals with Orthogonal Offset Carriers," *Optics Express*, vol. 26, no. 12, pp. 15 887–15 898, 2018.

[4] D. Lu, X. Zhou, J. Huo, *et al.*, "Theoretical CSPR Analysis and Performance Comparison for Four Single-Sideband Modulation Schemes With Kramers-Kronig Receiver," *IEEE Access*, vol. 7, pp. 166 257–166 267, 2019.

[5] X. Zhang, C. Zhang, C. Chen, *et al.*, "Digital Chromatic Dispersion Pre-management for SSB Modulation Direct-detection Optical Transmission Systems," *Optics Communications*, vol. 427, pp. 551–556, 2018.

[6] Z. Li, M. S. Erkılınç, K. Shi, *et al.*, "SSBI Mitigation and the Kramers–Kronig Scheme in Single-Sideband Direct-Detection Transmission With Receiver-Based Electronic Dispersion Compensation," *IEEE/OSA Journal of Lightwave Technology*, vol. 35, no. 10, pp. 1887–1893, 2017.

[7] R. K. Patel, I. A. Alimi, N. J. Muga, *et al.*, "Optical Signal Phase Retrieval With Low Complexity DC-Value Method," *IEEE/OSA Journal of Lightwave Technology*, vol. 38, no. 16, pp. 4205–4212, 2020.

[8] T. Bo and H. Kim, "Kramers-Kronig Receiver Operable Without Digital Upsampling," *Optics Express*, vol. 26, no. 11, pp. 13 810–13 818, 2018.

[9] T. Bo and H. Kim, "Towards Practical Kramers-Kronig Receiver: Resampling, Performance, and Implementation," *IEEE/OSA Journal of Lightwave Technology*, pp. 461–469, 2018.

[10] F. P. Guiomar, S. B. Amado, A. Carena, *et al.*, "Fully Blind Linear and Nonlinear Equalization for 100G PM-64QAM Optical Systems," *Journal of Lightwave Technology*, vol. 33, no. 7, pp. 1265–1274, 2015.

[11] A. Mecozzi, C. Antonelli, and M. Shtaif, "Kramers-Kronig Coherent Receiver," *Optica*, vol. 3, no. 11, pp. 1220–1227, 2016.

Chapter 5

Impact of Carrier Contribution Factor in the DC-Value Method

The DC-Value method provides an upsampling free phase reconstruction process at low carrier to signal power ratio (CSPR) [1]. The underlying idea of the DC-Value method is to iteratively impose the minimum phase condition (MPC) [1], [2]. The signal reconstruction accuracy of the DC-Value method depends on the accurate estimation of the carrier contribution factor (CCF) used in the MPC. Notice that, the estimation of the CCF is simpler in the case of DC-coupled photodetectors. However, the DC component at the output of the photodetector causes unwanted bias offset to the subsequent circuits [3]. Also, the DC component degrades the signal quality when automatic gain control (AGC) is employed at the receiver [4], [5]. In this context, the AC-coupled photodetectors alleviate the aforementioned problems and also allow to use of the full scale of the analog to digital converter (ADC) that translates into an improved signal to quantization noise ratio (SQNR). Therefore, the AC-coupled photodetectors tend to become the preferred choice in high-speed optical communication systems [5], despite, making the CCF estimation more challenging.

Here, we present an accurate CCF estimation technique that does not require any iterative process and it is compatible with both DC and AC-coupled photodetectors. We also discuss an experimental validation of the proposed technique. We show that by applying this method, the CCF estimation error falls below 1% for CSPR as low as 9 dB. Also, the experimental results confirm that the optimum bit error rate (BER) value can be found within ±5% offset of the estimated CCF value [6].

This chapter comprises four sections. In section 5.1, we analyze the impact of the CCF in the DC-Value method. In section 5.2, we present a novel procedure to estimate the CCF. In section 5.3, we present experimental results obtained by the proposed method. Section 5.4 presents a brief discussion about various factors and their related impact on self-coherent (SCOH) transceiver. The major concluding remarks are presented in section 5.5.

5.1 The Carrier Contribution Factor (CCF)

Consider the complex envelope of the incoming MPC optical signal as [1],

$$E(t) = E_o\, e^{i(2\pi f_o t+\phi)} + E_s(t), \tag{5.1}$$

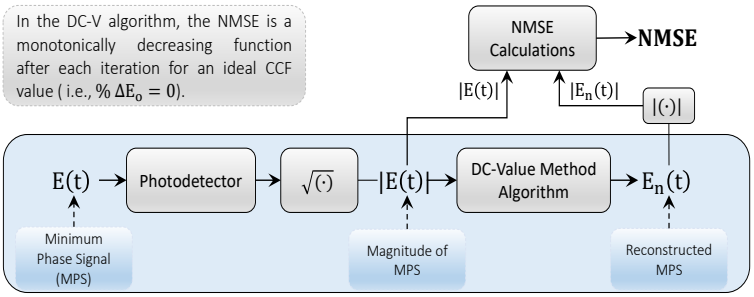

Figure 5.1: Schematic diagram of the normalized mean squared error (NMSE) calculation between available minimum phase signal (MPS) magnitude, $|E(t)|$, and the DC-Value method estimated MPS magnitude, $|E_n(t)|$.

where, $E_o\, e^{(i2\pi f_o t+\phi)}$ represents a carrier tone with an amplitude E_o, frequency f_o, and phase ϕ that coincides with the right edge of the information spectrum, and $E_s(t)$ is the complex information signal. When the field is detected using a DC-coupled photodetector, the following photocurrent will be generated,

$$I(t) = R_{pd}\left(|E_o|^2 + 2\,\Re\{E_s(t)\;{E_o}^* e^{-i(2\pi f_o t+\phi)}\} + |E_s(t)|^2\right), \tag{5.2}$$

where, R_{pd} is the responsivity of the photodetector, and $\Re\{\bullet\}$ represents the real part of $\{\bullet\}$. The first term in (5.2) is the carrier-carrier beating DC component (the square-root of the first term, $|E_o|$, is refereed as the CCF), the second term is the desired carrier-signal beating, and the last term is the inherent signal-to-signal beating noise (SSBN). Recall that the working principle of the proposed DC-Value method is based on iteratively imposing the single sideband (SSB) and DC-Value properties of the minimum phase signal, referred to as the MPC [1]. The MPC can be imposed on the Fourier transformed signal $\tilde{E}'_n(\omega)$, as it is done in [1], to attain the subsequent estimate of the minimum phase signal $\tilde{E}_n(\omega)$ in iteration n (refer to Fig. 5.8 for the algorithm),

$$\tilde{E}_n(\omega) = \begin{cases} 0, & \text{for } \omega > 0 \\ N|E_o|, & \text{for } \omega = 0 \\ p\tilde{E}'_n(\omega), & \text{for } \omega < 0 \end{cases} \tag{5.3}$$

where N represents the fast Fourier transform (FFT) length, and p denotes the scaling factor, assuming the value $p = 2$ for $n = 1$, and $p = 1$ for $n > 1$.

5.1.1 Impact of the CCF

The NMSE is an important parameter to characterize signal reconstruction accuracy in the DC-Value method. It is mathematically shown in section 3.2.1 that the NMSE function between the known magnitude, $|E(t)|$, and the estimated magnitude, $|E_n(t)|$ (see Fig. 5.1),

$$\text{NMSE} = \frac{\int_{-\infty}^{\infty} \Big|\, |\mathrm{E(t)}| - |\mathrm{E_n(t)}| \,\Big|^2 \mathrm{dt}}{\int_{-\infty}^{\infty} \Big|\, \mathrm{E(t)} \,\Big| \mathrm{dt} \int_{-\infty}^{\infty} \Big|\, \mathrm{E_n(t)} \,\Big| \mathrm{dt}}, \tag{5.4}$$

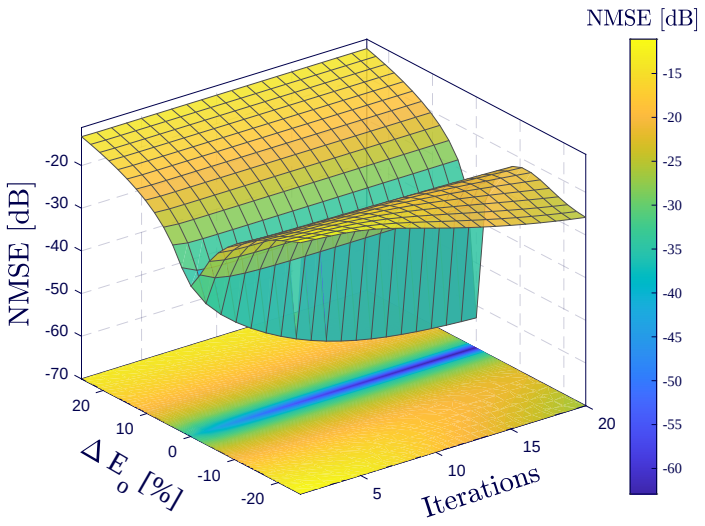

Figure 5.2: Impact of the CCF estimation error ΔE_o in signal reconstruction using the DC-Value method. Here, CSPR of 12 dB was considered in the numerical analysis.

is a monotonically decreasing function after each iteration in the DC-Value method. The monotonically decreasing NMSE function shows the convergence of the DC-Value method, which leads to an accurate reconstruction of the minimum phase signal. An accurate reconstruction improves overall system performance in terms of BER and computation complexity as it requires less iterations in the DC-Value method, and propagates low distortions to the post-digital signal processing (DSP). However, this result assumes that the receiver is able to retrieve the CCF value perfectly. In order to take into account the error in the CCF estimation at the receiver, the MPC can be re-written as,

$$\tilde{E}_n(\omega) = \begin{cases} 0, & \text{for } \omega > 0 \\ N(|E_o| \pm \Delta E_o), & \text{for } \omega = 0 \\ p\tilde{E'}_n(\omega), & \text{for } \omega < 0 \end{cases} \tag{5.5}$$

where ΔE_o is the estimation error of the CCF. The estimation error ΔE_o can violate the MPC property and limits the signal reconstruction accuracy. Also, it should be noted that the signal reconstruction accuracy varies with the amount of the CCF error estimation at the receiver end. Indeed, if the CCF estimation error is too high then no significant gain is obtained using the DC-Value method when compared with the other state of the art phase recovery methods. Indeed, this can justify the limited accuracy observed in the recently proposed experimental results for the time-domain implementation of the DC-Value method [7], where the DC-Value method provides a limited improvement when compared to KK methods.

Next, we quantify the impact of the CCF estimation error ΔE_o in the signal reconstruction process using the DC-Value method. For the purpose of assessment of the CCF impact, let's consider a 24 Gbaud 16QAM DC-Value system with a CSPR of 12 dB. The electric field is detected using a single photodetector and full signal reconstructed using a DC-Value method algorithm. Results shown in Fig. 5.2 presents the NMSE between the known MPS magnitude, $|E(t)|$, and the DC-Value method estimated MPS magnitude, $|E_n(t)|$, as a function of

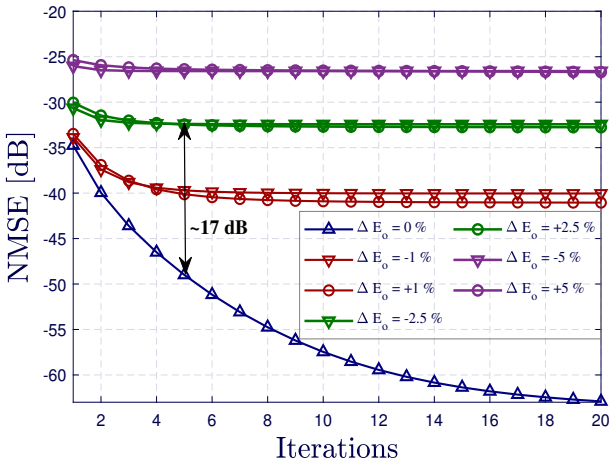

Figure 5.3: Impact of the CCF estimation error ΔE_o on the NMSE as a function of iteration number.

ΔE_o for 20 iterations. In the signal reconstruction process, we varied the CCF error, ΔE_o, from -25 to +25% and analyze its impact on the NMSE.

The analysis shows that for ΔE_o = 0%, the NMSE converges to zero, as it was expected. We can also see that if ΔE_o increases then the NMSE becomes nearly independent of the number of iterations, preventing a proper convergence of the DC-Value method, thus resulting in a limited reconstruction accuracy. Results shown in Fig. 5.3 confirm that the NMSE is monotonically decreasing for the ΔE_o = 0%. For an estimation error greater than ±2.5%, a 17 dB NMSE penalty is observed in the numerical analysis for 5 iterations. Results presented in Fig.5.4 show that for an SNR of 30 dB, a BER threshold of 10^{-3} can be assured after 10 iterations if the CCF estimation error ΔE_o falls within approximately ±5% range. Further, we have performed extensive simulation for other similar systems and the obtained results are analogous, i.e. the CCF must be estimated within a ±5% error to fully exploit the advantages of the DC-Value method. In the subsequent section, we show an accurate method to estimate the CCF for the DC-Value method compatible with both DC and AC-coupled photodetectors.

5.2 The CCF Estimation Method

In a DC-coupled photodetector, the photocurrent generated upon direct-detection can be written from (5.2) as (considering responsivity R_{pd} = 1),

$$I(t) = |E_o|^2 + 2\ \Re\{E_s(t)\ E_o{}^* e^{-i(2\pi f_o t+\phi)}\} + |E_s(t)|^2. \tag{5.6}$$

The DC-coupled photocurrent contains nonzero DC component contributed from the carrier-carrier beating, $|E_o|^2$, and the signal-signal beating, $|E_s(t)|^2$. The carrier-signal beating does not contain any non-zero DC component as it has zero mean value. Thus, the DC component in (5.6) can be written as,

$$\langle I(t)\rangle = |E_o(t)|^2 + \langle |E_s(t)|^2\rangle, \tag{5.7}$$

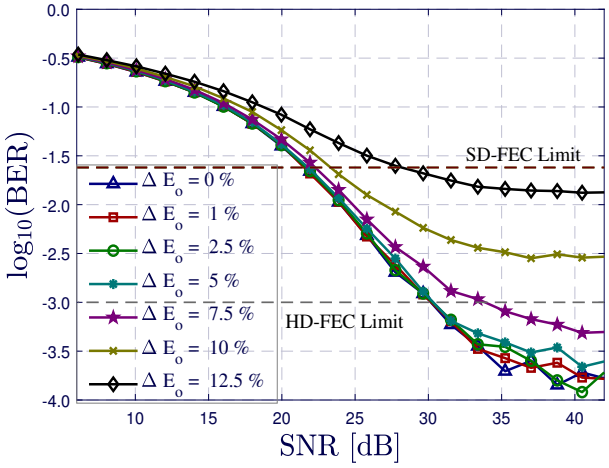

Figure 5.4: Impact of the CCF estimation error ΔE_o on the BER as a function of signal to noise ratio (SNR). For higher negative value of ΔE_o (usually less than -5%), the CCF value reduces significantly and the signal no longer follows the minimum phase condition in the phase reconstruction process which results in highly degraded system performance. Therefore, we have considered only positive ΔE_o values in the analysis to assess the performance.

therefore,

$$\langle I(t)\rangle = P_c + \langle P_s(t)\rangle, \tag{5.8}$$

where $P_c = |E_o|^2$, $P_s(t) = |E_s(t)|^2$ and $\langle\bullet\rangle$ indicates an average operator. To make the notations simpler in the CCF estimation process, we can rewrite (5.6) as,

$$I(t) = P_c + P_s(t) + 2\sqrt{P_c P_s(t)}\,\cos(\phi). \tag{5.9}$$

Notice that the photodetector sensitivity is assumed as $R_{pd} = 1$ for simplicity. In practice, the value of responsivity may differ from 1, nevertheless, the proposed CCF estimation method is insensitive to responsivity value.
In the case of AC-coupled photodetector, the DC component given by (5.8) gets filtered out by the DC block. Therefore, for the AC-coupled photodetector the current is given by,

$$I_{AC}(t) = I(t) - \langle I(t)\rangle. \tag{5.10}$$

Putting (5.8) and (5.9) in (5.10), we can rewrite it as,

$$I_{AC}(t) = P_s(t) + 2\sqrt{P_c P_s(t)}\,\cos(\phi) \;-\; \langle P_s(t)\rangle. \tag{5.11}$$

In case of sufficiently large CSPR (usually higher than 8 dB), we can assume that (refer to Fig. 5.5 for the approximation error),

$$\langle I_{AC}^2(t)\rangle \approx 2P_c\langle P_s(t)\rangle. \tag{5.12}$$

Now considering $\langle P_s(t)\rangle = P_c/\text{CSPR}$ in the (5.12),

$$\langle I_{AC}^2(t)\rangle \approx 2P_c\langle P_s(t)\rangle = 2P_c^2/\text{CSPR}. \tag{5.13}$$

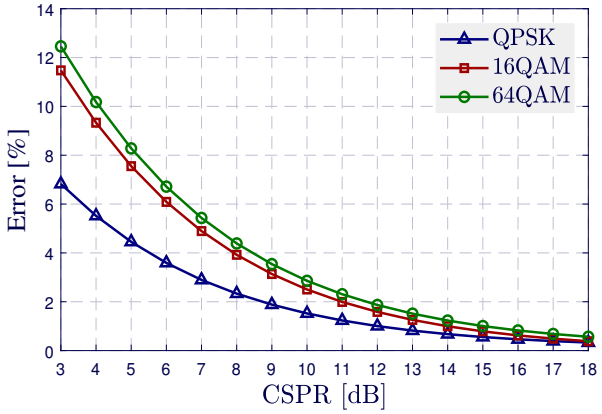

Figure 5.5: Approximation error in $\langle I_{AC}^2(t)\rangle$ when (5.12) is used. Usually, an optimum CSPR value usually lies higher than 8 dB which ensures low approximation errors in (5.12).

Therefore,

$$P_c^2 = \langle I_{AC}^2(t)\rangle \frac{\text{CSPR}}{2},$$

$$P_c = \sqrt{\langle I_{AC}^2(t)\rangle \frac{\text{CSPR}}{2}}. \tag{5.14}$$

From (5.14), the estimated CCF value, $\hat{E}_o$, can be written as,

$$\hat{E}_o = \sqrt{P_c} \approxeq \left(\langle I_{AC}^2(t)\rangle \frac{\text{CSPR}}{2}\right)^{\frac{1}{4}}. \tag{5.15}$$

Equation (5.15) can be used to formulate the MPC in the DC-Value method. In a similar way, considering $P_c = \text{CSPR}\ \langle P_s(t)\rangle$ in (5.12), we obtain,

$$\langle P_s(t)\rangle = \sqrt{\langle I_{AC}^2(t)\rangle \frac{1}{2\ \text{CSPR}}}. \tag{5.16}$$

Therefore, from (5.11), (5.14) and (5.16), the photocurrent with its recovered DC component can be written as,

$$I(t) \approxeq I_{AC}(t) + \sqrt{\langle I_{AC}^2(t)\rangle \frac{\text{CSPR}}{2}}(1 + 1/\text{CSPR}). \tag{5.17}$$

The photocurrent represented by (5.17) can be used as an input to the signal reconstruction algorithms (such as Kramers-Kronig (KK) or DC-Value methods) to reconstruct the full optical field. Further, the CCF estimation error in percentage can be written as,

$$\%\Delta E_o = \frac{|E_o| - \hat{E}_o}{|E_o|} \times 100, \tag{5.18}$$

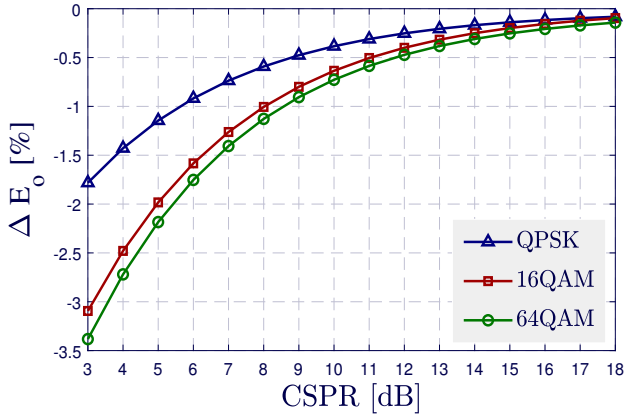

Figure 5.6: Numerical analysis of the CCF estimation error ΔE_o in % using (5.18) with respect to CSPR for different modulation formats. The analysis shows that the CSPR is not a relevant factor for the CCF estimation as the ΔE_o lies below 3.5% for the given CSPR range.

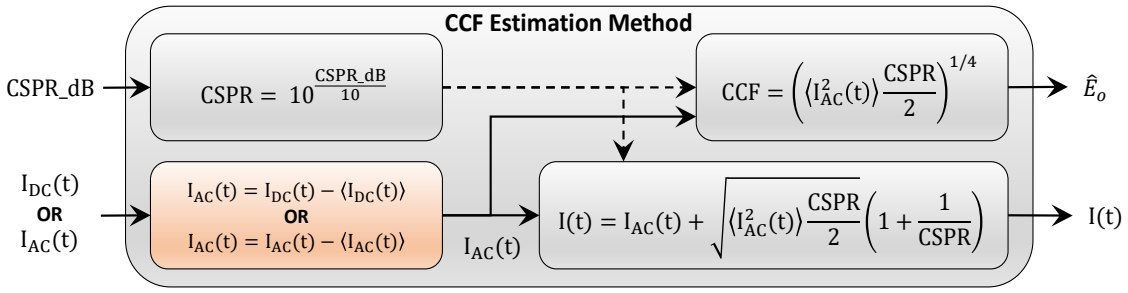

Figure 5.7: The algorithmic flow of DC component recovery and estimation of the CCF compatible with both DC and AC-coupled photodetectors, i.e. $I_{AC}(t)$ or $I_{DC}(t)$ as an input.

The results in Fig. 5.6 show the numerical analysis of the CCF estimation accuracy of the purposed method as function of the CSPR. The analysis shows that the CSPR is not a relevant factor for the CCF estimation as the ΔE_o lies below 3.5% for the given CSPR range. The results in the Fig. 5.6 shows that less than 1% error can be ensured for the CSPR value as low as 8.5 dB for the given QPSK, 16QAM, and 64QAM modulation formats.

To summarize, the algorithmic flow shown in Fig. 5.7 presents the proposed method of DC component recovery and estimation of the CCF. In practice, the known value of CSPR, and the photodetected current signal are supplied to the CCF estimation algorithm. First, the signal is passed through the DC remover and followed by a DC component recovery estimation (as per (5.17)) to calculate the photocurrent with its recovered DC component. Similarly, by using the known value of CSPR and output of the DC remover, the estimation of the CCF can be carried out (as per (5.15)) before employing the DC-Value method.

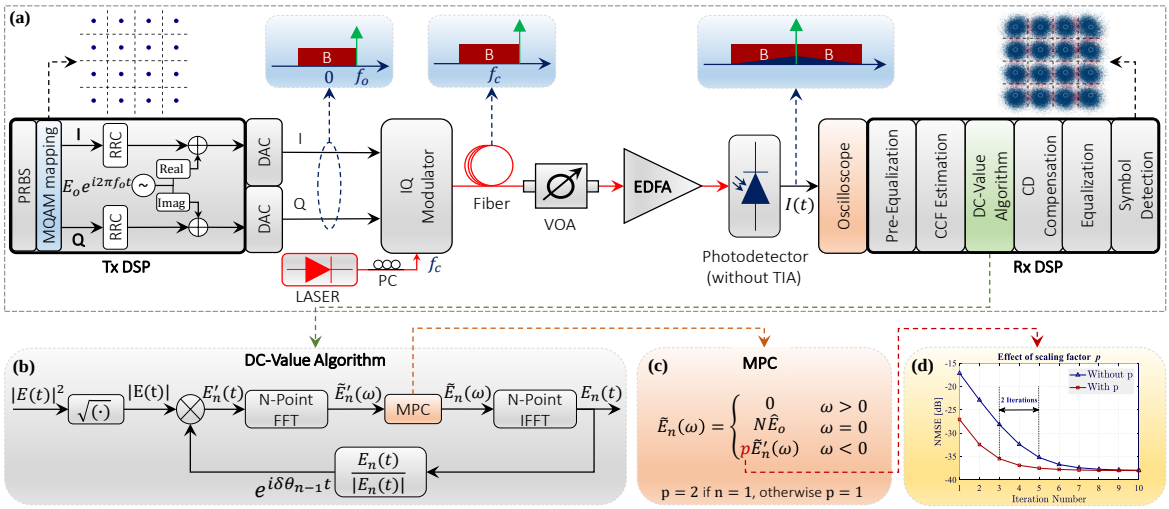

Figure 5.8: Experimental setup of a SCOH transceiver employing DC-Value method. Here, virtual carrier added in the digital domain to reduce optical complexity. As mentioned earlier, only one optical amplifier employed (as a preamplifier) in the transmission link to reduce cost.

5.3 Experimental Validation

In this section, we experimentally validate the proposed CCF estimation method and its impact on the overall system performance. We start this section by describing the experimental setup in detail.

5.3.1 DC-Value Transceiver Experimental Setup

At the transmitter side, see Fig. 5.8(a), a single-channel 24 Gbaud 16QAM signal is generated using a root raised cosine (RRC) pulse shaping filter with 0.1 roll-off factor. Following that, a complex tone $E_o e^{2\pi f_o t}$, at frequency f_o = 13.2 GHz (considering 0.1 RRC roll-off factor, 1.1× 24 Gbaud/2 = 13.2 GHz), is added to the 24 Gbaud 16QAM signal, $E_s(t)$, in the digital domain. The digitally added complex tone coincides with the right edge of the information signal spectrum to generate an SSB information signal. The amplitude E_o of the complex tone should be kept sufficiently higher than information signal (usually higher than 9 to 10 dB) to satisfy the MPC condition upon photodetection. The desired CSPR is obtained by varying the amplitude E_o of the complex tone.

After transmitter digital signal processing (Tx-DSP), in our case, a Keysight M8194A arbitrary waveform generator (AWG) containing 120 GSa/s digital to analog converter (DAC) is used to generate the signal. It should be noted that no pre-equalization was employed at the transmitter end. The output of the DAC is modulated at 1550 nm using a single polarization IQ Mach–Zehnder modulator (IQ-MZM). The output of the IQ-MZM signal is directly launched to the standard single-mode fiber (SSMF). It should be noticed that the digitally added carrier tone could make the IQ-MZM bias control circuitry unstable due to its very high amplitude and makes it difficult to lock the IQ-MZM bias conditions. To circumvent this problem, first the bias conditions are locked using only the information signal without digitally added carrier tone and then after locking bias conditions, we can digitally add carrier

tone to generate the SSB signal. Following the SSMF, the optical signal is amplified by an erbium-doped fiber amplifier (EDFA) and detected using a low-cost 40 GHz single photodetector without trans-impedance amplifier (TIA). The photodetector output is then sampled by a 100 GSa/s Tektronix real-time oscilloscope (RTO) with 33 GHz bandwidth. Finally, the experimental data captured by the RTO is processed offline using MATLAB software.

In the receiver digital signal processing (Rx-DSP), first, pre-equalization is carried to compensate the non-flat response of the photodetector. Following that, the proposed CCF estimation technique is applied to estimate the CCF and recover the DC component of the photodetected signal. Next, the signal is passed to the DC-Value method to recover the missing phase information. Moreover, the transmitter response is compensated by an adaptive equalizer after the signal reconstruction process. Also, it should be noted that no digital upsampling or downsampling is required in the DC-Value method.

In the DC-Value method, first, a square-root operation is carried out to obtain the magnitude $|E(t)|$ of the optical field and multiplied by a phase correction factor $e^{i\delta\theta_{n-1}(t)}$ which outputs the complex signal $E'_n(t)$. In the first iteration ($n = 1$), the phase correction vector is assumed to be zero, i.e. $\delta\theta_0(t) = 0$. Next, the MPC is imposed (see Fig. 5.8(c)) on the Fourier transformed signal $\tilde{E'}_n(\omega)$ to attain $\tilde{E}_n(\omega)$ as discussed in (5.3). The scaling factor p used in the MPC greatly speeds up the convergence process (see Fig. 5.8(d)). It is worth noticing that the scaling factor p improves the convergence speed because the input signal, $E'_n(t)$, for the first iteration consists of a real-valued amplitude signal $|E(t)|$, i.e. $\delta\theta_0(t) = 0$ as discussed in Chapter 3. It shows that the implementation of the scaling factor p requires two less iterations to achieve the same accuracy without scaling factor. After imposing MPC, the inverse fast Fourier transform (IFFT) of the $\tilde{E}_n(\omega)$ is computed to obtain the first estimate of the minimum phase signal $E_1(t)$. The phase correction vector corresponds to $E_1(t)$ and can be calculated as $e^{i\delta\theta_1(t)} = \frac{E_1(t)}{|E_1(t)|}$. This phase estimated is then supplied as an updated phase correction vector for the subsequent iteration ($n = 2$). This process continues until the desired accuracy is reached.

Also, the NMSE between the known magnitude $|E(t)|$ and the estimated magnitude $|E_n(t)|$ is monotonically decreasing after each iteration (see Fig. 5.8(d)), therefore, the reconstruction process converges as discussed earlier in section 5.1. Afterwards, the reconstructed minimum phase signal $E_n(t)$ is passed through the DC remover and then upconverted by multiplying it with $e^{i2\pi f_o t}$. Finally, the chromatic dispersion compensation and equalization can be carried out before symbol recovery.

5.3.2 Performance Analysis

In this subsection, we present the experimental analysis of the impact of the CCF (estimated by proposed method discussed in section 5.2, and referred as $\hat{E}_o$) on the overall system BER performance in the DC-Value method. To analyze the impact of $\hat{E}_o$, we first calculate the $\hat{E}_o$ value using (5.15) as discussed previously in the section 5.2, and add an offset error δ_o in the estimated $\hat{E}_o$ ranging from -25 to +25% with the step size of 0.55 % to assess its impact on

the overall system performance. The $\hat{E}_{o,\text{offset}}$ can be given as,

$$\hat{E}_{o,\text{offset}} = \hat{E}_o\left(1 + \frac{\delta_o}{100}\right). \tag{5.19}$$

Results shown in Fig. 5.9 present the impact of δ_o on the overall BER performance for the different CSPR values for 24 Gbaud 16QAM signal after 40 km SSMF. The dotted red line in Fig. 5.9 represents the estimated $\hat{E}_o$ value by the proposed CCF estimation method (with no added offset, i.e. $\delta_o = 0\%$). The surface between two dotted yellow lines represent the range between ±5% offset. For CSPR values ranging from 3 to 18 dB, we change the offset value δ_o as discussed above and calculate the BER performance of the system.

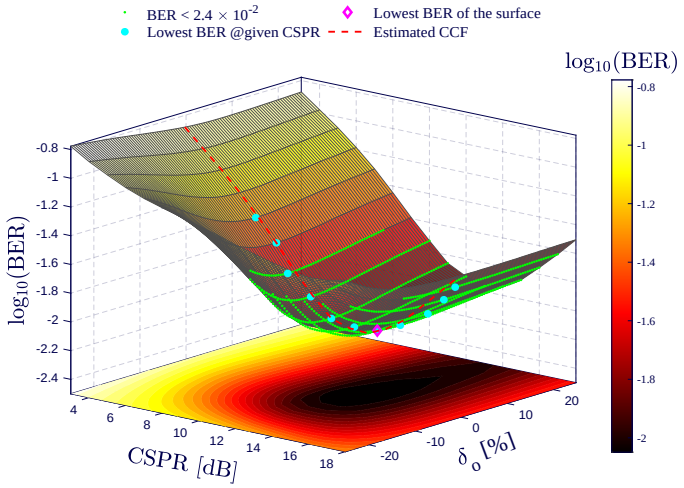

(a)

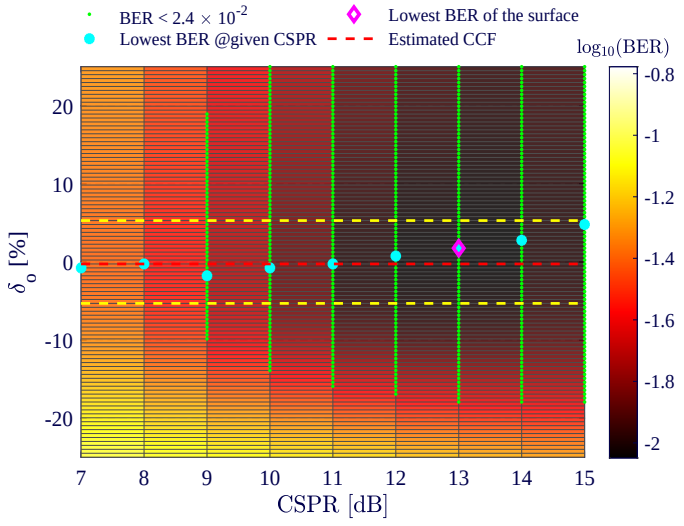

(b)

Figure 5.9: Performance analysis in terms of BER for the 24 Gbaud 16QAM signal after 40 km SSMF as function of CSPR and estimated $\hat{E}_o$ offset δ_o, (a) 3D view, and (b) 2D view (Zoomed portion between CSPR of 7 to 15 dB).

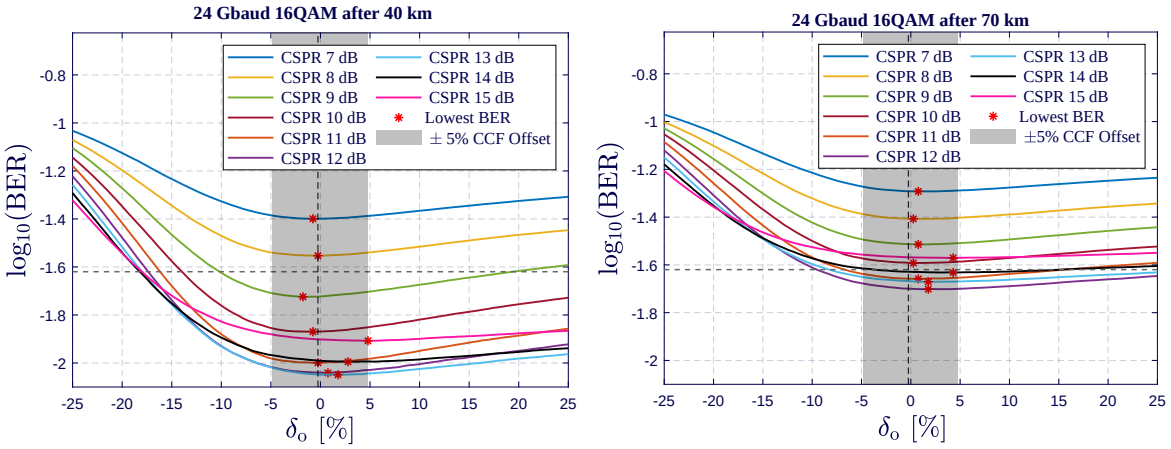

(a) **(b)**

Figure 5.10: Analysis of the impact of $\hat{E}_o$ estimation error on the system performance after transmission of (a) 40 km, and (b) 70 km. Here, virtual carrier assisted 24 Gbaud 16QAM signal used for the performance assessment. Results shows that the lowest BER can be assured in the DC-Value method when the $\hat{E}_o$ estimation falls below ±5%.

For each CSPR value, we find the lowest achievable BER in the given range of δ_o and it is represented as blue dots in the graph. Also, small green dots shown in the results represent valid BER values considering the soft-decision-FEC (SD-FEC) threshold of 2.4×10^{-2}. It shows that the value of BER becomes valid for the CSPR ≥ 9 dB considering the same SD-FEC threshold. The major highlight of Fig. 5.9 is that the lowest BER lies between ±5% of the estimated $\hat{E}_o$ value which shows the higher CCF estimation accuracy of the proposed method.

Nevertheless, Fig.5.9 shows that the estimation error δ_o increases for CSPR higher than ~12 dB. This peculiar behaviour arises from the limited DAC resolution (recall we add carrier virtually), and the Mach-Zehnder modulator as it starts operating in a nonlinear regime, which effectively changes the CSPR at the transmitter end. The proposed method requires the knowledge of the CSPR at the receiver end to recover the DC component. Additionally, it should be noted that the actual CSPR may change due to the impairments caused by transmission and optoelectronic components. Therefore, starting from the known value of CSPR at the transmitter, the DC-Value method can be used as a tool to improve the CSPR estimation at the receiver by proper adjustments of the offset δ_o such that the NMSE becomes a monotonically decreasing function as we discussed earlier in Fig. 5.3.

Results shown in Fig. 5.10(a) presents the $\log_{10}$(BER) as a function of δ_o for the 24 Gbaud 16QAM signal received after 40 km SSMF. The shaded gray area in Fig. 5.10(a) represents the ±5% range of δ_o. It is shown that the optimum BER value can be found in the close proximity of the estimated $\hat{E}_o$ value by the proposed CCF estimation method. Additionally, ~0.2 dB penalty in terms of Q factor is observed for the $\delta_o \geq 10$ % for CSPR of 11 dB. Similarly, the analysis of the received signal after 70 km SSMF shown in Fig. 5.10(b) represents the identical result like Fig. 5.10(a) such that the optimum BER values for the given CSPR lie within ±5% range of δ_o. Another important observation is that after 13 dB CSPR value, an optimum value of $\log_{10}$(BER) is found a little bit far from the $\hat{E}_o$ value. The possible reason

behind this could be that the digitally added carrier tone makes the IQ-MZM bias controller unstable when a very high power tone (usually higher than 13 dB observed in our experiment) is inserted in the signal. In this situation, the actual CSPR value of the optical signal differs from the virtual carrier added digital signal. Also, it should be noticed that slightly higher CSPR can help reduce the phase jump [8].

5.4 Related Impact on SCOH Transceiver

In this subsection, the associated impacts of different factors such as optoelectronic front-end, laser related effect, chromatic dispersion (CD), and IQ imbalance on the MPS based subsystem (i.e. KK, upsampling free KK and DC-Value iterative method) are discussed.

5.4.1 Opto-Electronic Front-End

The KK receivers have demonstrated high potential for full-optical field reconstruction in one polarization by employing a single photodetector such as the heterodyne detection. However, unlike heterodyne detection, the required CSPR is much more relaxed. Furthermore, the signal distortions imposed by fiber propagation (i.e., chromatic dispersion) occurred prior to the square law detection can be compensated after optical field reconstruction [9]. Nonetheless, the KK reconstruction algorithm is susceptible to the signal distortion that occurs between square law detection and KK processing [10]. Therefore, for an effective optical field reconstruction, the squared magnitude of the optical field has to be fed into the KK algorithm without further distortions that might emanate from the digitization processing and optical to electrical (O/E) conversion. In a practical receiver, this is not usually the case, and distortion is normally induced by the O/E conversion frontend transfer function. In general, the receiver has bandwidth limitations and the residual phase and magnitude responses of its associated components such as transimpedance amplifier, photodetector, and ADC. It should be noted that if the electrical distortion is not compensated, it can bring about residual SSBN and can equally affect the optical field reconstruction [9], [10].

Moreover, the impact of receiver bandwidth limitations on the KK algorithm has been studied, and it has been numerically demonstrated that even with moderate receiver bandwidth limitations, a significant optical signal to noise ratio (OSNR) penalty can be induced. Similarly, it has been experimentally demonstrated that adaptive equalizer employment prior to the KK processing can alleviate the O/E frontend bandwidth limitation impact on the KK field reconstruction and subsequently enhance the system performance [9], [10]. Furthermore, the impact of the magnitude and phase distortions has been considered, and it has been revealed that the magnitude response presents a much more stringent impact compared with the phase response. However, in the course of KK detection, a slight phase response can induce an ~0.5 dB penalty [10]. An abrupt change in the amplitude or phase can also result in a more severe penalty. In general, for an effective optical field reconstruction, the phase and magnitude distortions that might have occurred within the signal bandwidth have to be compensated prior to the KK algorithm's application [10].

5.4.2 Laser Related Effects

Additionally, it has been demonstrated that the KK implementation is sensitive to laser detuning from the center of the channel [11]. Moreover, it has been demonstrated experimentally that in spite of the SCOH direct detection nature, laser phase noise has a severe impact on the KK transmission performance, owing to its interactions with both fiber chromatic dispersion and a strong optical carrier. In that work, the system performance with distributed feedback and fiber lasers was compared at 11 dB CSPR. The presented results demonstrated a considerable performance gain for fiber laser employment. The gain was due to the low linewidth and frequency stability of the fiber laser. This resulted in a lower performance penalty by the interaction of dispersion and phase noise during propagation [12]. This implies that the employment of a low-quality laser with a high linewidth can bring about substantial degradation in the transmission performance. In [13], by considering the equalization-enhanced phase noise (EEPN) and phase-to-amplitude noise conversion, the impact of laser phase noise on direct detection transmission with the KK scheme was analyzed.

5.4.3 Fiber Dispersion

The KK algorithm can effectively mitigate SSBN, and it can digitally compensate the chromatic dispersion. In [14], the impacts of the chromatic dispersion on both KK and SSBN iterative cancellation receivers were investigated. Both receivers can effectively accomplish field recovery and with a comparable spectral efficiency (SE). However, the KK algorithm depends on the minimum-phase condition to reconstruct the optical field. Based on this, it demands a suitably high CSPR [14].

In addition, it has been demonstrated that the optimal CSPR value for the KK scheme increases with an increase in the transmission distance. This is owed to an increase in the chromatic dispersion-induced peak to average power ratio (PAPR) that violates the minimum-phase condition [15]. As a result of this, the field cannot be accurately recovered, resulting in transmission performance degradation. Therefore, the OSNR sensitivity of the KK algorithm depends on the chromatic dispersion. On the other hand, the IC receiver has no limitation on the minimum-phase condition. Consequently, it demonstrates high robustness against chromatic dispersion irrespective of the CSPRs. Therefore, the IC receiver is insensitive to chromatic dispersion, while the KK subsystem is sensitive to it. To be robust against chromatic dispersion, a relatively high CSPR is required by the KK scheme, resulting in an increment in the optimal CSPR [14]. Although the KK algorithm is sensitive to chromatic dispersion, for short-reach applications, polarization mode dispersion is not a main limiting factor [16].

5.4.4 IQ Imbalance

The effective implementation of the KK algorithm depends mainly on the SSB modulated signal. In an IQ modulator (IQM), for the perfect generation of an SSB signal, the I port and Q port are driven via the double sideband (DSB) upconverted signal and its related Hilbert transform, respectively. In this regard, an SSB signal will be generated through the seamless cancellation of one sideband by the combination of the Hilbert transform pairs. Furthermore, to fulfill the minimum-phase condition, it is imperative to add a strong continuous wave (CW)

optical carrier to the signal [17].

It is noteworthy that the IQM is most efficient when biased at null. This means better electrical spectrum efficiency as it generates two sidebands. This implies an improved power efficiency. Therefore, any configuration that deviates from this will suffer either electrical spectrum efficiency or power efficiency degradation. Furthermore, the practical challenges of the IQM implementation to generate the optical SSB signal are timing misalignment, amplitude imbalance, and IQ phase mismatch between the I and the Q components of the signal. Likewise, these factors will significantly affect the suppression ratio of the optical sideband. Consequently, the resulting IQ imbalance of the modulator causes the minimum-phase condition violation and generates interfering DSB distortion components in the optical spectrum. These result in the performance degradation of the KK system. Moreover, the subsequent limitation of the IQ imbalance on the back-to-back performance is owed to the minimum-phase condition, while its associated degradation in the transmission performance is due to dispersion-induced RF power fading [17].

5.5 Final Remarks

The CCF is an important parameter in the DC-Value method and it used to form the MPC for the DC-Value method algorithm. Using the knowledge of CSPR value, we proposed a novel CCF estimation method compatible with both DC and AC-coupled photodetector for the DC-Value self-coherent transceiver. We present the analysis and impact of the CCF in the DC-Value method and show that the CCF estimation error should be no more than ±5% to ensure better system performance. The numerical analysis shows that the CCF estimation is quite insensitive to the CSPR value. In practice, results shows that the optimum CSPR value usually lies around 12 to 13 dB and we can ensure less than 1% CCF estimation error by the proposed method. Also, we performed experimental analysis of 24 Gbaud 16QAM signal transmission and employed proposed method to estimate the CCF.

References

[1] R. K. Patel, I. A. Alimi, N. J. Muga, *et al.*, "Optical Signal Phase Retrieval With Low Complexity DC-Value Method," *IEEE/OSA Journal of Lightwave Technology*, vol. 38, no. 16, pp. 4205–4212, 2020.

[2] R. K. Patel, F. P. Guiomar, M. A. Fernandes, *et al.*, "Virtual Carrier Assisted Self-Coherent Detection Employing DC-Value Method," *Optical Fiber Communications Conference and Exhibition (OFC)*, pp. 1–3, 2021.

[3] K. Hara, S. Kimura, H. Nakamura, *et al.*, "New AC-Coupled Burst-Mode Optical Receiver Using Transient-Phenomena Cancellation Techniques for 10 Gbit/s-Class High-Speed TDM-PON Systems," *IEEE/OSA Journal of Lightwave Technology*, vol. 28, no. 19, pp. 2775–2782, 2010.

[4] E. Sackinger, "Broadband Circuits for Optical Fiber Communication," *John Wiley & Sons, Inc.*, 2005.

[5] T. Bo and H. Kim, "DC Component Recovery in Kramers-Kronig Receiver Utilizing AC-Coupled Photo-Detector," *IEEE/OSA Journal of Lightwave Technology*, vol. 38, no. 16, pp. 4307–4314, 2020.

[6] R. K. Patel, F. P. Guiomar, M. A. Fernandes, *et al.*, "Impact of the Carrier Contribution Factor in the Self-coherent DC-value Method," *Optics Express*, vol. 29, no. 25, pp. 41 234–41 245, 2021.

[7] W. Wang, D. Zou, Z. Li, *et al.*, "Optical Single Sideband Signal Reconstruction Based on Time-Domain Iteration," *IEEE/OSA Journal of Lightwave Technology*, pp. 1–1, 2021.

[8] S. T. Le, K. Schuh, M. Chagnon, *et al.*, "1.6 Tb/s Virtual-Carrier Assisted WDM Direct Detection Transmission Over 1200 km," *IEEE/OSA Journal of Lightwave Technology*, vol. 37, no. 2, pp. 418–424, 2019.

[9] X. Chen, S. Chandrasekhar, S. Olsson, *et al.*, "Impact of O/E Front-End Frequency Response on Kramers-Kronig Receivers and its Compensation," *European Conference on Optical Communication (ECOC)*, pp. 1–3, 2018.

[10] X. Chen, C. Antonelli, S. Chandrasekhar, *et al.*, "Kramers–Kronig Receivers for 100-km Datacenter Interconnects," *IEEE/OSA Journal of Lightwave Technology*, vol. 36, no. 1, pp. 79–89, 2018.

[11] S. Ohlendorf, R. Joy, S. Pachnicke, *et al.*, "Flexible PAM in DWDM Transmission with Kramers-Kronig DSP," *European Conference on Optical Communication (ECOC)*, pp. 1–3, 2018.

[12] K. Schuh and S. T. Le, "180 Gb/s 64QAM Transmission Over 480 km Using a DFB Laser and a Kramers-Kronig Receiver," *European Conference on Optical Communication (ECOC)*, pp. 1–3, 2018.

[13] S. T. Le, K. Schuh, and H. Nguyen Tan, "A Closed-Form Expression for Direct Detection Transmission Systems With Kramers-Kronig Receiver," *IEEE Photonics Technology Letters*, vol. 30, no. 23, pp. 2048–2051, 2018.

[14] C. Sun, D. Che, and W. Shieh, "Comparison of Chromatic Dispersion Sensitivity between Kramers-Kronig and SSBI Iterative Cancellation Receiver," *Optical Fiber Communication Conference and Exhibition (OFC)*, W4E.4, 2018.

[15] C. Sun, D. Che, H. Ji, *et al.*, "Towards Low Carrier-to-Signal Power Ratio for Kramers-Kronig Receiver," *Optical Fiber Communications Conference and Exhibition (OFC)*, pp. 1–3, 2019.

[16] C. Sun, D. Che, R. Schmid, *et al.*, "Polarization Mode Dispersion Impacts on Kramers-Kronig Receiver," *Opto-Electronics and Communications Conference (OECC)*, pp. 1–2, 2018.

[17] T. Bo and H. Kim, "Performance Analysis of Kramers–Kronig Receiver in the Presence of IQ Imbalance," *IEEE Photonics Technology Letters*, vol. 30, no. 24, pp. 2171–2174, 2018.

Chapter 6

Probabilistic Shaping with the DC-Value Method

In the previous chapters, we investigated several self-coherent (SCOH) techniques such as Kramers-Kronig (KK), upsampling free KK, and DC-Value method employing conventional coded uniform modulation schemes such as QAM and QPSK for the performance assessment. The flexibility of such systems is limited since they are only coarsely adaptable. Also, conventional coded modulation schemes show a gap to Shannon capacity that can be addressed only by using modulation formats having a Gaussian-like shape. Probabilistic shaping can effectively address the limitations of conventional coded modulation schemes.

This chapter presents the experimental results of the SCOH DC-Value method with an adaptive rate probabilistic constellation shaping (PCS) modulation. It shows the limitation of conventional uniform modulation format and explains the advantages of using PCS modulation. It also explains the standard architecture to generate the PCS modulation in the transmission.

This chapter comprises four sections. Section 6.1 presents a general concept of probabilistic shaping. In section 6.2, the architecture and the implementation details of probabilistic shaping are discussed. In section 6.3, the details of the experimental setup, the performance analysis and discussion of the obtained experimental data are presented. Finally, section 6.4 presents the concluding remarks.

6.1 Concept of Probabilistic Shaping

While the evolution of higher-order modulation has improved both wavelength capacity and spectral efficiency, the conventional QAM imposes several limitations. The first limitation relates to the maximum reach. As modulation order increases, the constellation points get closer together for the same average power, making them less tolerant to noise and fiber impairments. Also, there exists a trade-off between sensitivity to noise. The increased power provides higher tolerance to noise (refer to Fig. 6.1). Nevertheless, it also increases the nonlinearities. On the other hand, the decreased power helps reduce nonlinearities, but conversely, it reduces the noise tolerance level.

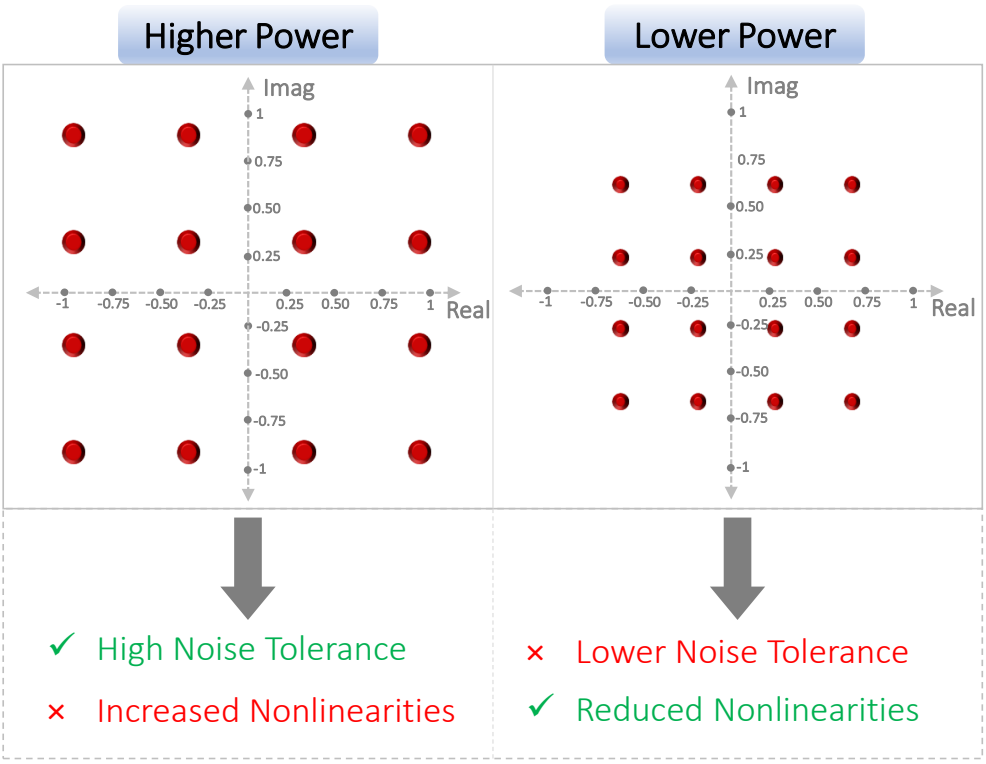

Figure 6.1: Noise tolerance vs nonlinearities.

The PCS is an advanced modulation format technique that addresses the limitations of conventional QAM modulation. As mentioned earlier, the conventional coded modulation schemes show a gap to Shannon capacity that can be overcome only by using modulation formats that have a Gaussian-like shape. PCS can help close the capacity gap [1]. In conventional modulation format, each constellation point has the same probability. In other words, outer constellation points with higher energy/power have the same probability as inner constellation points with lower energy/power. On the other hand, the PCS uses the lower energy/power inner constellation more frequently than higher energy/power outer constellation points. It enables PCS to deliver several benefits such as snhanced granularity, improved noise tolerance, and baud rate flexibility.

In other words, as opposed to standard QAM constellations, which are typically composed of independent and identically distributed (IID) symbols, the concept of PCS lies on the assignment of a given probability distribution function to its constellation symbols, thereby controlling both the entropy and average transmitted signal energy [2]. In practice, this probability distribution can be achieved by the Maxwell-Boltzmann distribution function. Subsequently, the basic theory of the Maxwell-Boltzmann distribution and its offered benefits are discussed.

6.1.1 The Maxwell-Boltzmann distribution

The Maxwell-Boltzmann distribution maximizes bit rate for a fixed average energy [3]. In other words, the Maxwell-Boltzmann distribution minimizes the required average energy for a fixed bit rate. It should be noted that the given constellation must be able to support the given bit rate or the given average energy such that these values are themselves constrained. The Maxwell-Boltzmann distribution causes a constellation point, r, with energy, $\|r\|^2$, to be selected with a probability of [3],

$$p(r) \propto e^{-\lambda \|r\|^2} \tag{6.1}$$

where, the parameter $\lambda \geq 0$ governs the trade-off between bit rate and average energy. More precisely, the optimal distribution is given as,

$$p(r) \propto \frac{e^{-\lambda \|r\|^2}}{Z(\lambda)}, \qquad \lambda \geq 0 \tag{6.2}$$

where the partition function $Z(\lambda)$ is chosen to normalize the distribution, i.e.,

$$Z(\lambda) \triangleq \sum_{r \in \Omega} e^{-\lambda \|r\|^2}, \qquad \lambda \geq 0 \tag{6.3}$$

where, Ω is a constellation alphabet. For finite constellations, setting $\lambda = 0$ yields a uniform probability signaling scheme in which all constellation points are selected with uniform probability. Therefore, $\lambda = 0$ leads a "classical" fixed-rate signaling scheme to appear as a special case. Also, it should be noted too that, with a Maxwell-Boltzmann distribution, outer points (points with large energy) are never selected more often than inner points (points with small energy). An equivalence class of the points of Ω all having the same energy is called a *shell* of the constellation. With a Maxwell-Boltzmann distribution, the points of a *shell* are selected equally often [3].

When the Maxwell-Boltzmann distribution is applied to set the probability of appearance of each constellation symbol in additive white Gaussian noise (AWGN) channels, it has been shown that PCS can provide a reduction of transmitted power by up to 1.53 dB [2], [4]. This effect is commonly referred to in the literature as the PCS shaping gain, and it has been the main driver behind its rapid adoption in optical fiber systems. In addition, the recent development of implementable fixed-length distribution matcher (DM) [5] to set the PCS symbol probabilities, also provides another key advantage in terms of enhanced flexibility and granularity for controlling the transmitted net bit rate [6].

6.1.2 Working Principle

The functional block that performs rate-adaptive shaping is the DM, which transforms uniformly distributed input information bits to the Maxwell-Boltzmann distributed output symbols. The DM is the key component in the PCS (see Fig. 6.2). At a high level, the DM takes a uniform bit sequence of ones and zeros with equal probability and convert these into symbols with a desired distribution. A reverse DM converts these symbols back to the original stream at the receiver end.

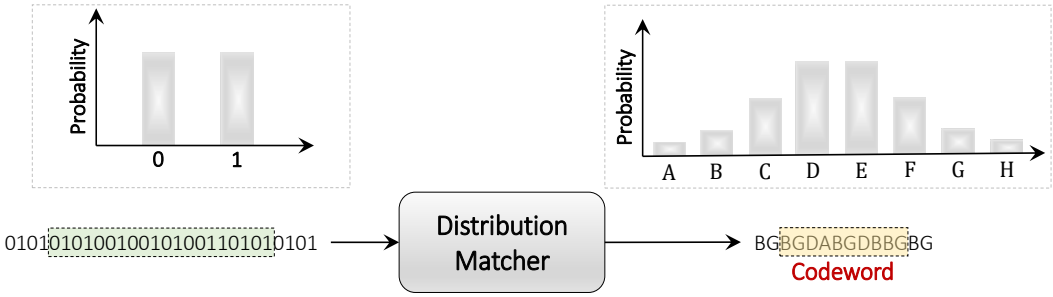

Figure 6.2: Working of a DM (adapted from [7]).

Number	Binary	Symbols
0	0000	DD
1	0001	DE
2	0010	DA
3	0011	DB
4	0100	DH
5	0101	BG
6	0110	GF
7	0111	FE
8	1000	CF
9	1001	CC
10	1010	EC
11	1011	ED
12	1100	EA
13	1101	EB
14	1110	EH
15	1111	GF

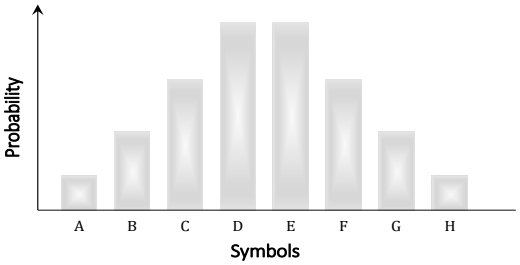

Figure 6.3: Example of bits to symbol mapping and symbol distribution (adapted from [7]).

To explain how the DM might work with a simple example, we take four bits (0 to 15) and convert these into two symbols from eight possible symbols, letters A to H, as shown in Fig. 6.3. Considering this bits to symbols combination, we will likely see a lot more "D"s and "E"s and a lot fewer "A"s or "H"s regardless of the incoming bitstream. Notice that bits are not mapped to individual symbols; instead, a string of bits is mapped to a combination of symbols. The mapping helps create the desired distribution. The example shown in Fig. 6.3 is using 6 bits (two 3-bit symbols) to transmit 4-bits worth of data. Therefore, the net data rate becomes two-thirds compared to uniform modulation with all symbols having equal probability.

An Illustrative Example

This example presents an illustration of the probabilistic shaping when the Maxwell-Boltzmann distribution was applied to constellation points. Here, an example of a 64QAM constellation is presented for various values of λ in the range of 0 to 1. Considering a given modulation format, the maximum shaping gain is observed around $\lambda = 1$. Nevertheless, as mentioned earlier in (6.1), the λ can have any arbitrary value greater than equal to 0. An equivalence class of the points of constellation all having the same energy is called a *shell* of the con-

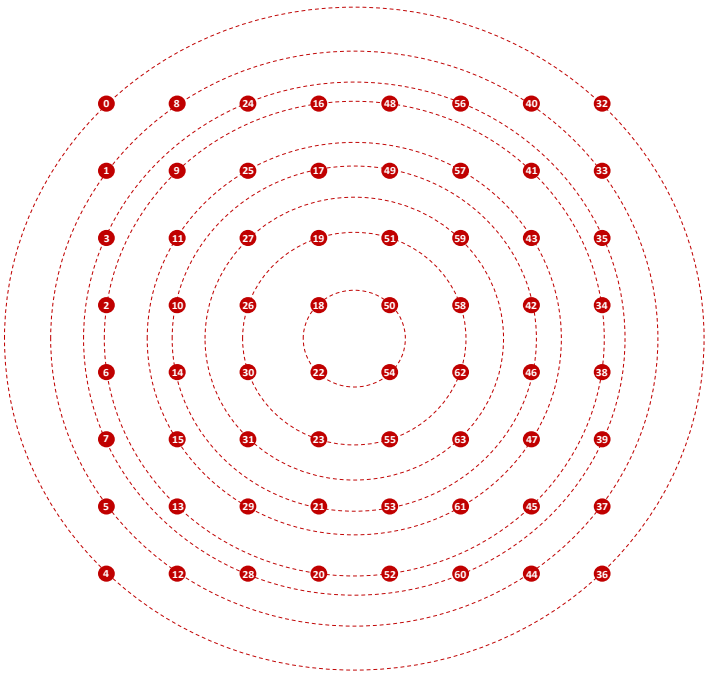

Figure 6.4: An illustrative example of 64QAM constellation mapping (gray coding scheme) template. For $\lambda = 0$, all constellation points lie in the same *shell* (classical uniform modulation scheme).

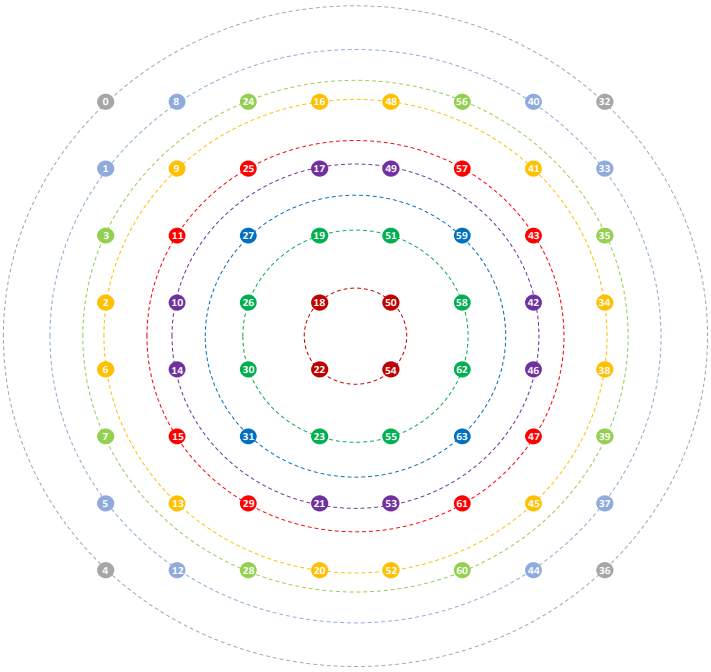

Figure 6.5: An illustrative example of 64QAM constellation mapping (gray coding scheme) template. It generates 9 different energy *shell* (refer to dotted circle) when applied the Maxwell-Boltzmann distribution with $\lambda > 0$.

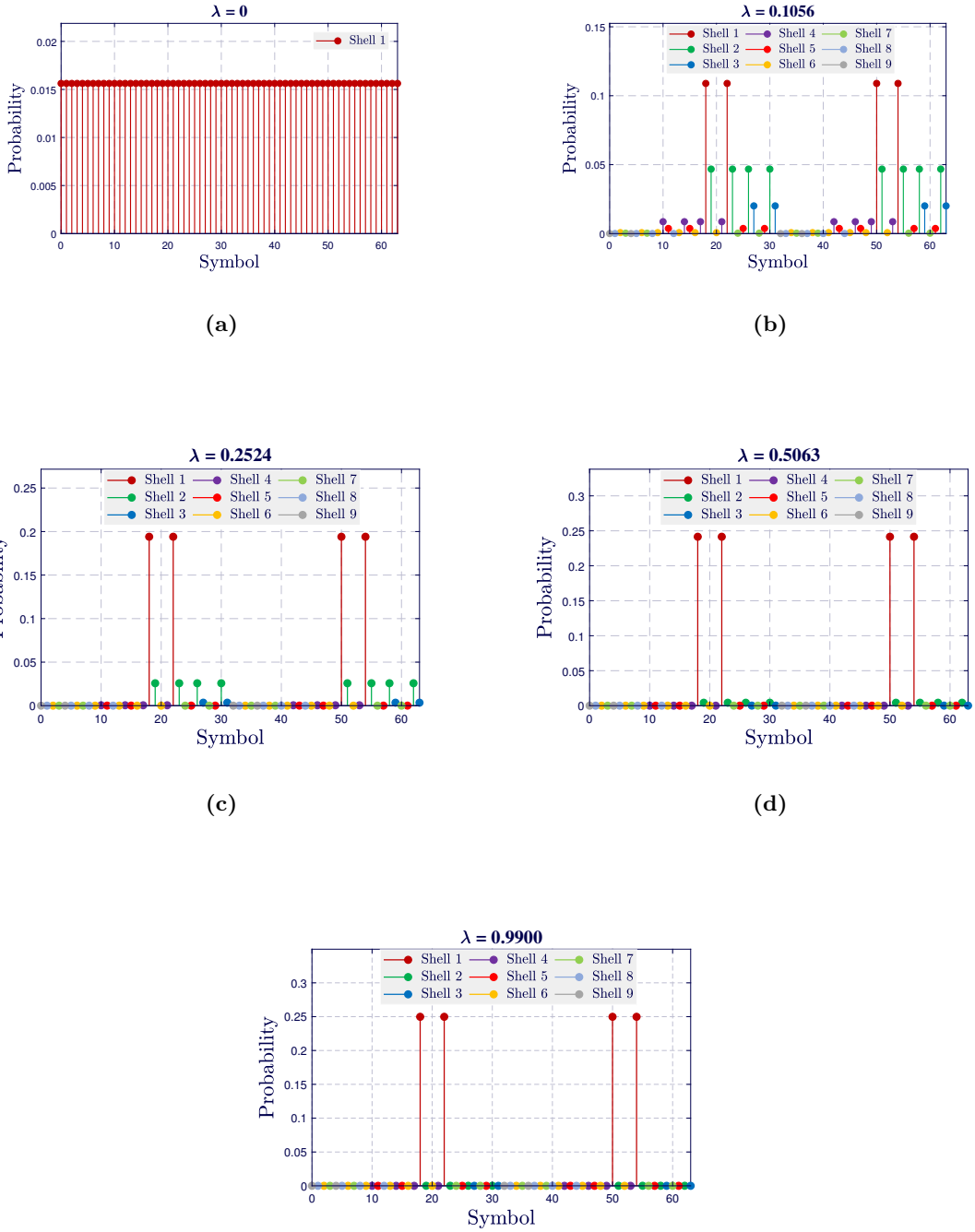

Figure 6.6: Probability of constellation points appearance when the Maxwell-Boltzmann distribution applied to 64QAM constellation template with (a) $\lambda = 0$, (b) $\lambda = 0.1056$, (c) $\lambda = 0.2524$, (d) $\lambda = 0.5063$, and (e) $\lambda = 0.99$.

stellation points. Fig. 6.4 presents various *shells* of the 64QAM constellation template in a dotted circle. Notice that, using the Maxwell-Boltzmann distribution, of 9 distinct shell that exists in a 64QAM template. Also, setting $\lambda = 0$ causes all constellation points to lie in the same *shell* with a uniform probability, yielding a "classical" fixed-rate and uniform signaling scheme to appear as a special case. In the following, we have shown 9 different *Shells* for the given 64QAM template with their respective member symbol:

$shell_1 = [18, 22, 50, 54]$

$shell_2 = [19, 23, 26, 30, 51, 55, 58, 62]$

$shell_3 = [27, 31, 59, 63]$

$shell_4 = [10, 14, 17, 21, 42, 46, 49, 53]$

$shell_5 = [11, 15, 25, 29, 43, 47, 57, 61]$

$shell_6 = [2, 6, 9, 13, 16, 20, 34{,}38, 41, 45, 48, 52]$

$shell_7 = [3, 7, 24, 28, 35, 39, 56, 60]$

$shell_8 = [1, 5, 8, 12, 33, 37, 40, 44]$

$shell_9 = [0, 4, 32, 36]$

It should be noted that power level of $shell_1 < shell_2 < shell_3 < shell_4 < shell_5 < shell_6 < shell_6 < shell_8 < shell_9$. Subsequently, we plot the probability distribution for the 64QAM constellation points for different values of λ. Results shown in Fig. 6.6a corresponds to setting $\lambda = 0$, which shows a classical uniform signaling scheme where all constellation points have the same probability. Next, Fig. 6.6b to 6.6d present the probability distribution for $\lambda = 0.1056$, $\lambda = 0.2524$, and $\lambda = 0.5063$, respectively. Note that, when shaping parameter λ increases, the probability of higher power constellation points decreases accordingly. When the value of shaping parameter λ approaches 0.99, the entire signaling scheme is limited to the innermost *Shell* of the original constellation, and it makes the probability of higher constellation points appearance almost zero.

In conclusion, the Maxwell-Boltzmann parameter λ (we call it as the shaping parameter λ) governs the trade-off between bit rate and average energy. In analogy with statistical mechanics, we might call λ as the *inverse temperature* of the Maxwell-Boltzmann distribution, i.e. $\lambda = 1/(kT)$, where k is the Boltzmann constant and T is the temperature. When $\lambda = 0$ (for infinite *temperature*), the uniform distribution is obtained, corresponding to the maximum possible entropy for the given constellation. When relates to statistical mechanics, all states of a system are equally occupied at infinite temperature. As $\lambda \to \infty$ (or the *temperature* cools toward absolute zero), the bit rate as well as the average energy are reduced as the points with large energy are selected less frequently. The "limiting constellation" (obtained at absolute zero *temperature*) consists of only the innermost points of the original constellation (the ground states in statistical mechanics), and these points are selected equally often [3].

6.2 Adaptive Probabilistic Shaped Modulation

Generally, PCS is practically enabled by probabilistic amplitude shaping (PAS). The problem with previously known PCS architectures is that performing coding after shaping at the transmitter distorts the shaped symbol distribution, as forward error correction (FEC) parity bits are generally not shaped. On the other hand, performing coding before shaping at the transmitter can cause error bursts upon de-shaping erroneously received symbols at the receiver. The PAS architecture elegantly circumvents this problem by optimally intertwining shaping and coding in a capacity-approaching and the efficiently implementable way [8].

6.2.1 The Architecture and Achievable Bit Rates

The general concept of PCS modulation resorting to the reverse concatenation principle associated with the PAS scheme is illustrated in Fig. 6.7. The DM is the key component of the PAS transmitter architecture, which is responsible for shaping the I and Q amplitude levels of the selected QAM template. This allows to allocate the remaining sign bits in the I and Q components (i.e. two bits in total) for carrying the systematic FEC parity bits, thus avoiding distorting the desired shaping through the FEC encoder. The total entropy that must be allocated for the FEC parity bits, H_{FEC}, can be calculated as,

$$H_{FEC} = (1 - R_{FEC}) \log_2(M_{PCS}) \tag{6.4}$$

where R_{FEC} is the FEC rate and M_{PCS} is the constellation size of the selected QAM template for PCS. Given the allocation of the FEC parity bits to the quadrant positions, the PAS scheme requires that $H_{FEC} \leq 2$, which consequently imposes that,

$$R_{FEC} \geq 1 - \frac{2}{\log_2(M_{PCS})} \tag{6.5}$$

As an example, for a 64QAM template, it results that $R_{FEC} \geq 2/3$. When the FEC rate is larger than the minimum imposed by (6.5), the remaining quadrant bits should be utilized to carry unshaped information bits. The available entropy for that effect is then simply given by,

$$H_{quad} = 2 - H_{FEC} \tag{6.6}$$

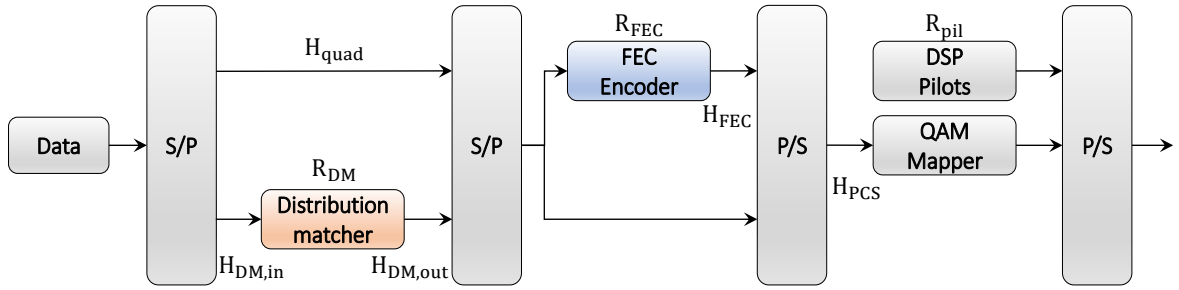

Figure 6.7: PAS transmitter architecture with digital signal processing (DSP) pilots insertion. S/P: serial-to-parallel; P/S: parallel-to-serial (adapted from [2]).

where, H_{quad} is the entropy of the remaining quadrant bits. Conversely, the information entropy fed to the DM, $H_{DM,in}$, is obtained from the amplitude bits in the QAM template,

$$H_{DM,in} = \log_2(M_{PCS}) - 2 \tag{6.7}$$

The DM will then provide a fine control over its output entropy,

$$H_{DM,out} = (H_{PCS}) - 2 \tag{6.8}$$

where H_{PCS} is the overall desired PCS entropy given by,

$$H_{PCS} = \frac{R_b}{2R_s R_{pil}} + H_{FEC} \tag{6.9}$$

where R_b is the target net bit rate, R_s is the operating symbol rate, R_{pil} is the DSP pilot rate and the factor of two accounts for dual-polarization transmission. Taking its input and output distribution entropies, the rate of the DM can simply be written as,

$$R_{DM} = \frac{H_{DM,out}}{H_{DM,in}} \tag{6.10}$$

Considering the allocation of the information payload in the PAS scheme of Fig. 6.7, the overall net bit rate of the transmitted PCS signal can be explicitly given by,

$$\begin{aligned} R_b &= R_s R_{pil}(H_{quad} + H_{DM,out}) \\ &= 2R_s R_{pil}[2 - (1 - R_{FEC})\log_2(M_{PCS}) + R_{DM}(\log_2(M_{PCS}) - 2)] \end{aligned} \tag{6.11}$$

where $0 \leq R_{DM} \leq 1$ is the free parameter that can be adjusted in order to adapt the transmitted bit rate. Given that the DM can only reduce the entropy of its input uniform distribution, i.e. $R_{DM} \leq 1$, it results that the maximum net bit rate supported by the PAS transmitter architecture is,

$$R_{b,max} = 2R_s R_{FEC} R_{pil} \log_2(M_{PCS}) \tag{6.12}$$

The maximum bit rate is then achieved for $H_{PCS} = \log_2(M_{PCS})$, i.e. for an uniform constellation, in which case the DM in Fig. 6.7 becomes a simple amplitude shift keying (ASK) mapper for the I and Q components. Conversely, the minimum net bit rate achievable by the PAS architecture is obtained when the DM collapses all its entries into a single output amplitude level, i.e. $H_{DM,out} = 0$ and thus $R_{DM} = 0$. In that extreme case, a QPSK output constellation is obtained, yielding the following minimum net bit rate,

$$R_{b,min} = R_{b,max} - 2R_S R_{pil}(\log_2(M_{PCS}) - 2) \tag{6.13}$$

where it is also implicit that the square QAM template for PCS must respect the condition $M_{PCS} > 4$.

6.2.2 Probability Distribution and Bit Rate Adaptation

Besides enabling the adaptation of the transmitted net bit rate, the DM can also be applied to minimize the average transmitted signal energy, thereby enhancing the energy efficiency of the transmission system. Following Shannon's theory for AWGN channels, the minimum

transmitted signal energy required to achieve a given bit rate is obtained by setting the QAM symbol probabilities, P_{x_n}, according to the Maxwell-Boltzmann distribution [3],

$$P_{x_n} = \frac{\exp\ (-\lambda |x_n|^2)}{\sum_{n=1}^{M_{PCS}} \exp\ (-\lambda |x_n|^2)} \tag{6.14}$$

where λ is the shaping parameter and x_n is the n-th symbol in the square M_{PCS} QAM constellation alphabet,

$$x_n = 2\left((n-1)\ \mathrm{mod}\ \sqrt{M_{PCS}}\right) - \sqrt{M_{PCS}} + 1 + i\left(2\left\lfloor \frac{n}{\sqrt{M_{PCS}}} \right\rfloor - \sqrt{M_{PCS}} - 1\right) \tag{6.15}$$

Note that a uniform distribution with symbol probabilities $P_{x_n} = 1/M_{PCS}$ is obtained by setting $\lambda = 0$, which corresponds to $R_{DM} = 1$. Considering the average energy of the corresponding constellations, the achievable shaping gain, G_{PCS}, can be provided by PCS using a QAM template of size M_{PCS} over a uniform QAM constellation of size M_{QAM} as,

$$G_{PCS} = 10\log_{10}\left(\frac{\sum_{n}^{M_{QAM}} |u_n|^2}{\sum_{k}^{M_{PCS}} |s_k|^2 P_{s_k}}\right) \tag{6.16}$$

where u_n and s_k are the symbols of the uniform and shaped constellations, respectively, which are obtained by replacing the corresponding constellation sizes in (6.15).

As an illustrative example of the PCS concept, let us consider the following parameters for a single polarization system:

- R_s = 30 Gbaud
- M_{PCS} = 36 Gbaud
- R_{pil} = 1 (no extra overhead for DSP pilots)
- R_{FEC} = 5/6 (20 % overhead for FEC)

Utilizing (6.12) and (6.13) with the aforementioned signal parameters (considering a single polarization system) and considering 36QAM format, it results that the achievable net bit rates with the PAS scheme lie within the interval of ~34 Gbps to ~129 Gbps. Note that, a varying data rate can be achieved by changing the rate of the DM block. A set of PCS constellation examples are shown in Fig. 6.8 corresponding to different bit rates in the range of ~34 Gbps to ~129 Gbps. Fig. 6.8(a) presents the PCS constellations corresponding to the 90 Gbps data rate. Fig. 6.8(a) shows that the high power constellation points (outer constellation points) have a relatively low probability of occurrence than low power constellation points (inner constellation points). Further, the probability of high power constellation points increases with the increased data rate from 100 Gbps to 125 Gbps as shown in Fig. 6.8(b) to Fig. 6.8(d), respectively. At a maximum 129 Gbps data rate (see Fig. 6.8(e)), the probability of symbol appearance is uniformly distributed over the entire constellation. It should be noted that the requested 36QAM PCS obtains a maximum of 5.17 bits entropy (i.e. $\log_2(36) = 5.17$ bits) in the case of a maximum achievable data rate of 129 Gbps. In practice, the bit rate can be controlled by adjusting the shaping parameter, λ, in (6.14).

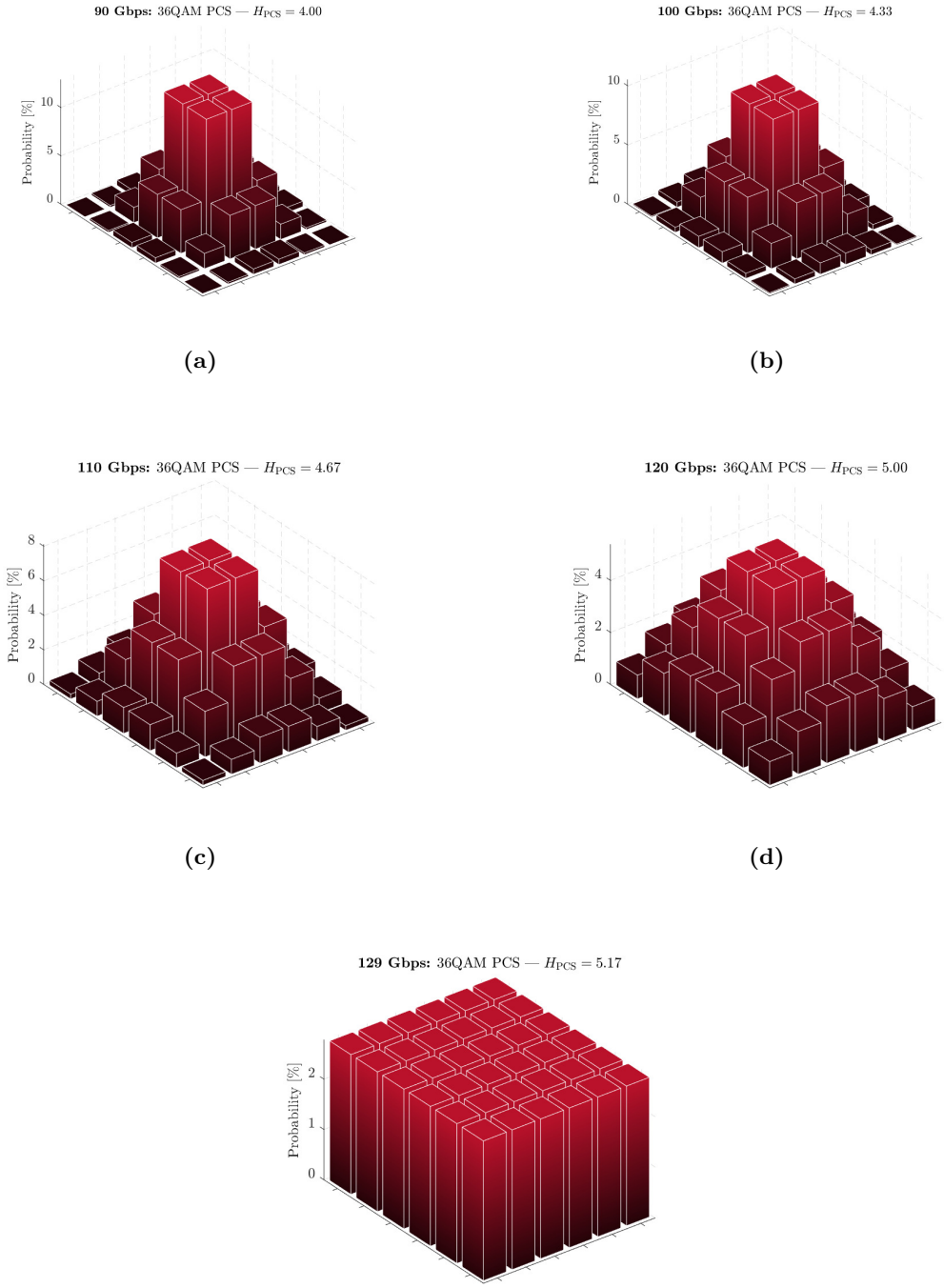

Figure 6.8: Graphical illustration of the symbol probability distributions in a 36QAM PCS constellation for different bit rates between the range from ~34 Gbps to ~129 Gbps. This graphs correspond to R_s = 30 Gbaud, M_{PCS} = 36, R_{pil} = 1, and R_{FEC} = 5/6 with a single polarization system.

6.2.3 Performance Assessment Metrics

Transmission systems utilizing the soft-decision-FEC (SD-FEC) coding paradigm, it is demonstrated that the generalized mutual information (GMI) is an adequate metric for pre-FEC performance assessment [9]. In an AWGN channel, and assuming a PCS-modulated transmitted signal, the GMI can be calculated as [10],

$$\text{GMI} = H_{PCS} - G(M_{PCS}, P_x, \sigma^2) \tag{6.17}$$

where G represents the loss of information due to propagation over the AWGN channel,

$$G(M_{PCS}, P_x, \sigma^2) = \frac{1}{N}\sum_{n=1}^{N}\sum_{k=1}^{\log_2(M_{PCS})} \log_2 \frac{\sum_{x_m\in\chi}\exp\big(-\frac{|y_n-x_m|^2}{\sigma^2}\big)P_{x_m}}{\sum_{x_m\in\chi(k,b_{n,k})}\exp\big(-\frac{|y_n-x_m|^2}{\sigma^2}\big)P_{x_m}} \tag{6.18}$$

where σ^2 is the noise variance of the AWGN channel, y_n is the n-th received symbol (out of a total of N symbols), x_m is the m-th symbol in the respective constellation alphabet, $b_{n,k}$ is the k-th bit of the n-th transmitted symbol and $\chi(k,b)$ is a subset of the constellation alphabet, χ, which contains bit $b \in [0\ 1]$in the k-th bit position. The GMI can then take values in the range of 0 to H_{PCS}, which ideally correspond to the worst and best signal to noise ratio (SNR) conditions, respectively. To provide an universal assessment of achievable information rate for any modulation format, the normalized generalized mutual information (NGMI) is commonly utilized, which can be defined as [11],

$$\text{NGMI} = 1 - \frac{G(M_{PCS}, P_x, \sigma^2)}{\log_2(M_{PCS})} \tag{6.19}$$

Considering an ideal FEC implementation, it can be shown that the minimum NGMI that ensures error-free transmission, NGMI_{th}, is given by $\text{NGMI}_{\text{th}} = R_{FEC}$. However, due to practical implementation constraints, the SD-FEC encoder/decoder typically suffers from a coding gap, i.e. it imposes that $\text{NGMI}_{\text{th}} = R_{FEC} + \delta_{FEC}$, where δ_{FEC} accounts for the non-ideal FEC performance loss. Notice that, in the case of uniform QAM, it follows that, $H(\chi) = \log_2(M)$ and therefore (6.19) simply reduces to NGMI = GMI/$\log_2$(M).

6.3 Experimental Results

This section presents the experimental setup employed for the virtual carrier assisted SCOH DC-Value method with the PCS modulation. The experimental setup is identical to the setup discussed in Fig. 4.8.

6.3.1 Experimental setup

At the transmitter side (see Fig. 6.9), various M-PCS 30 Gbaud symbols are generated using the PAS method discussed in Fig 6.7. After M-PCS mapping, symbols are passed through a pulse shaping root raised cosine (RRC) filter with a 0.1 roll-off factor. Following that, a complex tone $E_o e^{2\pi f_o t}$, at a frequency of f_o = 16.5 GHz (considering 0.1 RRC roll-off factor, 1.1 × 30 Gbaud/2 = 16.5 GHz), is added to the 30 Gbaud M-PCS signal, $E_s(t)$, in the digital domain. The desired carrier to signal power ratio (CSPR) is obtained by varying the

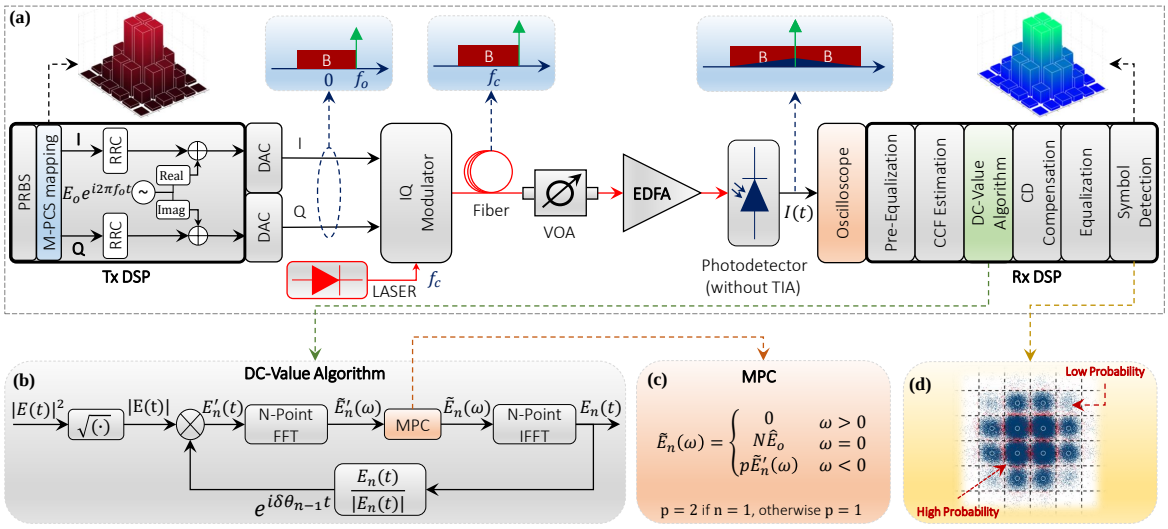

Figure 6.9: Experimental setup of the SCOH DC-Value method employing the PCS.

amplitude E_o of the complex tone. After Tx-DSP, the Keysight M8194A arbitrary waveform generator (AWG) containing 120 GSa/s digital to analog converter (DAC) is used to generate the signal. The output of the DAC is modulated at 1550 nm using a single polarization IQ Mach–Zehnder modulator (IQ-MZM). The output of the IQ-MZM signal is directly launched to the standard single-mode fiber (SSMF).

At the receiver end, following a similar procedure discussed in Chapter 4, the optical signal is amplified by an erbium-doped fiber amplifier (EDFA) and detected using a low-cost 40 GHz single photodetector without a trans-impedance amplifier (TIA). The photodetector output is then sampled by a 100 GSa/s Tektronix real-time oscilloscope (RTO) with 33 GHz bandwidth. Finally, the experimental data captured by the RTO is processed offline using MATLAB software.

6.3.2 Results and Discussion

In this subsection, we present obtained results for the 30 Gbaud transmission system with 20% FEC overhead. In the case of a single polarization 16QAM uniform modulation transmission system, we get the following data rate:

$$\begin{aligned} (\text{Net Data Rate})_{\text{MQAM}} &= R_s \; R_{pil} \; R_{FEC} \; \log_2(\text{M}) \\ &= 30 \text{ Gbaud} \times 1 \times \frac{5}{6} \times \log_2(16) \\ &= 100 \text{ Gbps} \end{aligned} \tag{6.20}$$

where, R_s is the baud rate of the signal, R_{pil} is the DSP pilot rate, R_{FEC} is the FEC overhead rate, and M is the constellation cardinality. Notice that the net 100 Gbps data rate can be achieved when (6.20) is considered with a 30 Gbaud 16QAM signal, $R_{pil} = 1$ and $R_{FEC} = 5/6$ (i.e. 20% FEC overhead). In the case of PCS modulation (refer to (6.15)), the net achievable

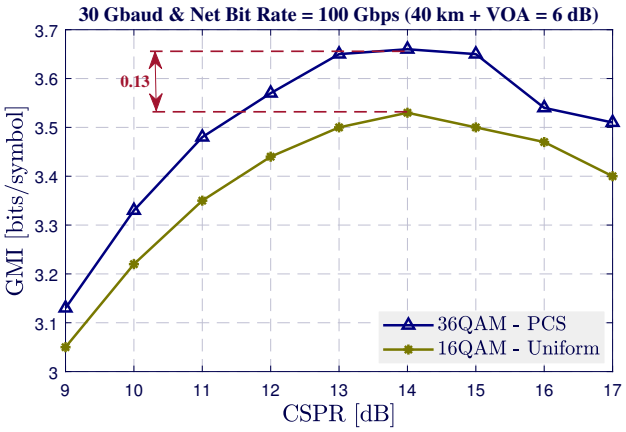

Figure 6.10: GMI vs CSPR for 36QAM PCS and 16QAM uniform modulation.

data rate can be varied by changing the rate of the DM, R_{DM}, as follows:

$$\begin{aligned}(\text{Net Data Rate})_{\text{MQAM–PCS}} &= R_s R_{pil}[2-(1-R_{FEC})\log_2(M_{PCS})+R_{DM}(\log_2(M_{PCS})-2)] \\ &= 30\times 1\times\left[2-\left(1-\frac{5}{6}\right)\log_2(36)+0.6924(\log_2(36)-2)\right] \\ &= 100 \text{ Gbps}\end{aligned} \tag{6.21}$$

where, R_s is the baud rate of the signal, R_{pil} is the DSP pilot rate, R_{FEC} is the FEC overhead rate, M_{PCS} is the constellation cardinality, and R_{DM} is the rate of the DM. Similarly, the net 100 Gbps bit rate can be achieved when (6.21) is considered with a 30 Gbaud 36QAM PCS signal, R_{pil} = 1, R_{FEC} = 5/6, and R_{DM} = 0.6924, we can achieve net 100 Gbps data rate. Note that the multiplication factor 2 is removed in the calculation of $(\text{Net Data Rate})_{\text{MQAM–PCS}}$ considering a single polarization system. In the following, we present the obtained results for both uniform and PCS modulation after transmission of 70 km distance.

36QAM PCS

This subsection presents the performance comparison of PCS and uniform modulation signaling after transmission of 70 km distance (40 km SSMF followed by 6 dB variable optical attenuator (VOA) attenuation). The performance is measured using a GMI and NGMI metric as a function of varying CSPR values in the transmission, respectively. Results depicted in Fig. 6.10 shows that the 36QAM PCS modulation provides an optimum 3.63 bits/symbol GMI at ~15 dB CSPR . Also, a similar trend is observed in a 16QAM uniform modulation format, where an optimum 3.53 GMI is observed for the same 15 dB CSPR transmission. The recovered constellation for both PCS and uniform modulation formats at an optimum operating CSPR are shown in Fig. 6.12(a) and (b), respectively. Notice that the obtained results correspond to 2 samples per symbol (SPS) DSP used in the signal reconstruction employing the DC-Value method. Results in Fig. 6.10 show that 36QAM PCS format provides ~0.13 bits/symbol GMI improvement compared to uniform 16QAM modulation format. Subsequently, the results shown in Fig. 6.11 presents a comparative analysis between PCS and

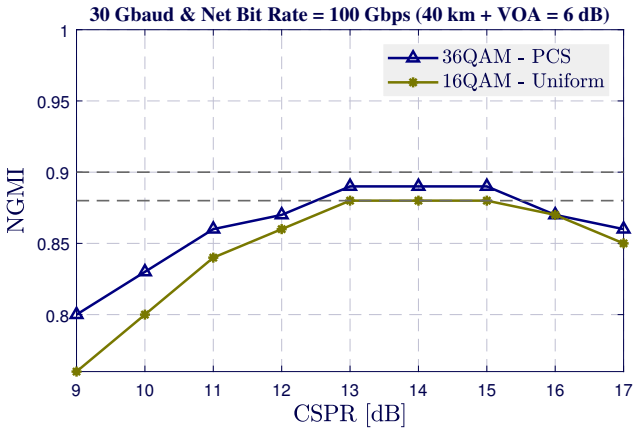

Figure 6.11: NGMI vs CSPR for 36QAM PCS and 16QAM uniform modulation.

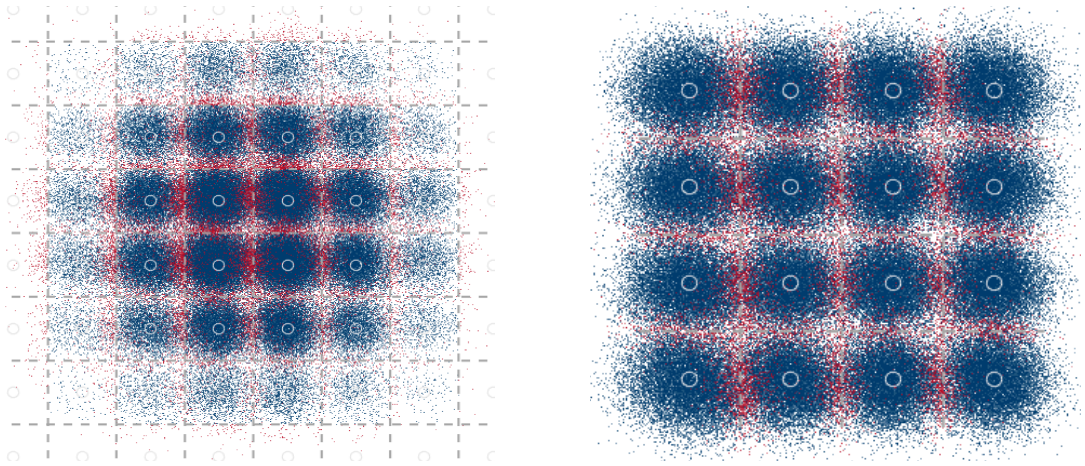

(a) **(b)**

Figure 6.12: Received signal constellation for 30 Gbaud signal considering (a) 36QAM PCS transmission, and (b) Uniform 16QAM transmission. (CSPR = 15 dB).

uniform modulation format using an NGMI metric. It shows that 36QAM PCS provides 0.01 NGMI improvement compared to uniform 16QAM modulation transmission. Notice that the EDFA is operated in constant output power mode, and the power of the optical signal falling on the photodetector remains identical for both PCS and uniform modulation formats. Nevertheless, it should be noted that the peak to average power ratio (PAPR) values are different in both PCS and uniform modulation cases. The value of PAPR increases with a constellation size and shaping parameter λ.

64QAM PCS

In this section, we present results for the increased constellation size (64QAM PCS) for the same 100 Gbps net bit rate with R_{FEC} = 5/6 and measure the system performance. Results shown in Fig. 6.13 presents the comparison between achieved GMI performance for 36 & 64QAM PCS and 16QAM uniform modulation transmission. Fig. 6.13 shows that the

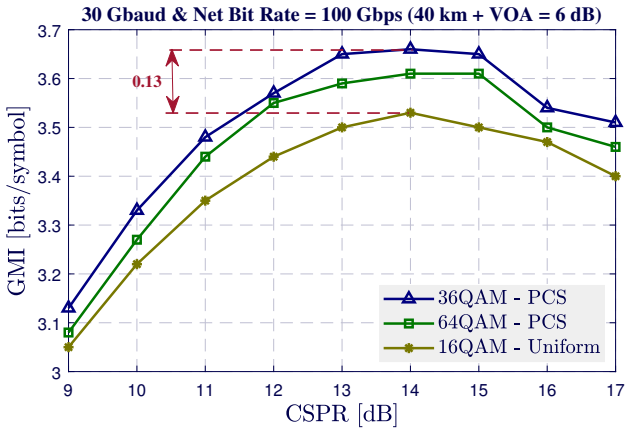

Figure 6.13: GMI vs CSPR for 36 & 64QAM PCS and 16QAM uniform modulation.

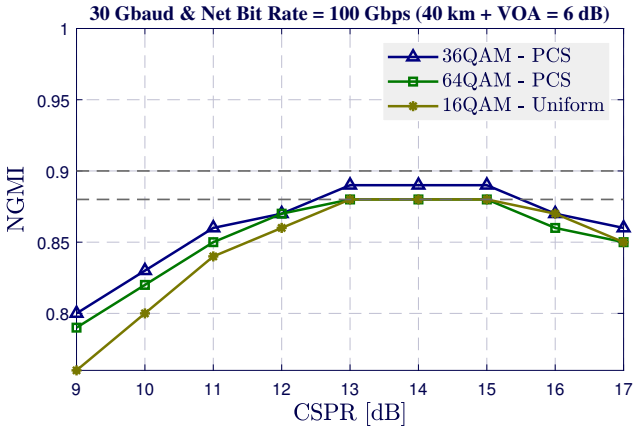

Figure 6.14: NGMI vs CSPR for 36 & 64QAM PCS and 16QAM uniform modulation.

36QAM PCS provides ~0.13 GMI gain compared to the uniform 16QAM modulation format (as we discussed earlier). Further, by increasing constellation size to 64QAM PCS, the system performance tend to degrade when compared to 36QAM PCS due to its increased constellation size and its related constraints. Recall that the PAPR increases with increased constellation size and so the PAPR for a 64QAM PCS case is highest when compared to 36QAM PCS and 16QAM uniform modulation. Notice that the signal with a higher PAPR sets a stricter requirement on the effective number of bits (ENOB) of the analog to digital converter (ADC) and DAC. Additionally, in the case of a SCOH transmission system, the higher PAPR can also affect the system performance. It can be viewed as high power constellation points experience a relatively low CSPR value compared to the lower power constellation points. Therefore, the higher power constellation points suffer more signal-to-signal beating noise (SSBN) and limit the system performance. Consequently, the choice of the optimum constellation size depends on various factors, such as ENOB, CSPR, and PAPR. The ENOB of the ADC can be varied by adjusting the vertical scale of the oscilloscope, making the received signal fill

the full screen. Nevertheless, the ENOB of the DAC still possesses a strict requirement in transmission and requires careful attention.

6.4 Final Remarks

In this chapter, we briefly discussed the underlying idea of probabilistic shaping and its offered advantages in signal transmission. The concept of PCS is based on the assignment of a probability distribution to constellation points. In practice, the Maxwell-Boltzmann distribution function can be employed to enable such probability distribution. Generally, the PCS can be realized by the PAS, and we discussed the architecture of the PAS in detail. Also, the performance assessment metric such as GMI and NGMI are explained briefly. The experimental results for the net 100 Gbps bit rate system are carried out for 36 & 64QAM PCS modulation and compared their results with uniform 16QAM modulation. Both PAPR and shaping gain increase with a larger constellation size, however, the higher PAPR indicates that the signal is more sensitive to ENOB and CSPR. This can also be confirmed from the experimental assessment that the 36QAM PCS provides better performance when compared to uniform 16QAM and 64QAM PCS modulations.

References

[1] F. Buchali, G. Böcherer, W. Idler, *et al.*, "Experimental Demonstration of Capacity Increase and Rate-adaptation by Probabilistically Shaped 64-QAM," *European Conference on Optical Communication (ECOC)*, pp. 1–3, 2015.

[2] F. P. Guiomar, A. Lorences-Riesgo, D. Ranzal, *et al.*, "Adaptive Probabilistic Shaped Modulation for High-Capacity Free-Space Optical Links," *IEEE/OSA Journal of Lightwave Technology*, vol. 38, no. 23, pp. 6529–6541, 2020.

[3] F. Kschischang and S. Pasupathy, "Optimal Nonuniform Signaling for Gaussian Channels," *IEEE Transactions on Information Theory*, vol. 39, no. 3, pp. 913–929, 1993.

[4] G. Böcherer, P. Schulte, and F. Steiner, "Probabilistic Shaping and Forward Error Correction for Fiber-Optic Communication Systems," *IEEE/OSA Journal of Lightwave Technology*, vol. 37, no. 2, pp. 230–244, 2019.

[5] P. Schulte and G. Böcherer, "Constant Composition Distribution Matching," *IEEE Transactions on Information Theory*, vol. 62, no. 1, pp. 430–434, 2016.

[6] F. P. Guiomar, L. Bertignono, D. Pilori, *et al.*, "Comparing Different Options for Flexible Networking: Probabilistic Shaping vs. Hybrid Subcarrier Modulation," *European Conference on Optical Communication (ECOC)*, pp. 1–3, 2017.

[7] "Faster, Further, Smoother: The Case for Probabilistic Constellation Shaping," *White Paper from Infinera*, pp. 1–12, 2020.

[8] J. Cho and P. J. Winzer, "Probabilistic Constellation Shaping for Optical Fiber Communications," *IEEE/OSA Journal of Lightwave Technology*, vol. 37, no. 6, pp. 1590–1607, 2019.

[9] A. Alvarado, E. Agrell, D. Lavery, *et al.*, "Replacing the Soft-Decision FEC Limit Paradigm in the Design of Optical Communication Systems," *IEEE/OSA Journal of Lightwave Technology*, vol. 33, no. 20, pp. 4338–4352, 2015.

[10] A. Alvarado, T. Fehenberger, B. Chen, *et al.*, "Achievable Information Rates for Fiber Optics: Applications and Computations," *IEEE/OSA Journal of Lightwave Technology*, vol. 36, no. 2, pp. 424–439, 2018.

[11] J. Cho, L. Schmalen, and P. J. Winzer, "Normalized Generalized Mutual Information as a Forward Error Correction Threshold for Probabilistically Shaped QAM," *European Conference on Optical Communication (ECOC)*, pp. 1–3, 2017.

Chapter 7

Conclusion and Future Work

This Ph.D. thesis contains a deep revision of the state of the art in the self-coherent (SCOH) transceiver schemes, highlighting their advantages and limitations, and proposes a novel solution for the phase recovery, carrying out a comprehensive optimization and experimental validation of this new technique. This chapter aims to present the main conclusions of this Ph.D. work and propose suggestions for future work.

7.1 Conclusions

Double sideband optical direct-detection (DD) schemes offer a low-cost and simple solution to extract information from an optical signal. Nevertheless, they impose an irreversible loss of phase information. single sideband (SSB) methods have been adopted as they enable the retrieval of amplitude and phase information using DD. However, they tend to suffer a strong penalty due to signal to signal-to-signal beating noise (SSBN) generated upon square-law detection. The adverse effects of SSBN can be alleviated either by enlarging the band-gap between the carrier and information signal or by increasing the carrier to signal power ratio (CSPR), at the expense of the spectral efficiency or nonlinear signal degradation, respectively.

The aforementioned problem of SSBN can be well addressed by a minimum phase signal based Kramers-Kronig (KK) receiver, which significantly reduces the impact of SSBN. The minimum phase condition of the signal implies that log-magnitude and phase are related by the Hilbert transform, and this requirement can be full filled by adding a constant value in the SSB complex signal. In practice, a continuous wave (CW) tone is added at the edge of the information signal spectrum that ensures the minimum phase condition upon DD. However, the nonlinear operations (logarithmic and exponential) in the KK algorithm demand the digital signal processing (DSP) to be operated a couple of times faster than the Nyquist sampling rate to accommodate spectral broadening induced by such operations. To reduce the sampling rate, such nonlinear functions can be replaced by approximations in the modified upsampling-free KK method. Nevertheless, such approximations tend to require higher tone power that increases the nonlinear distortions or sensitivity penalty [1].

To address the aforementioned high sampling rate and higher tone power requirements of the conventional KK and upsampling-free KK methods, respectively, a DC-Value method ex-

ploring the SSB and DC-Value properties of the minimum phase signal was proposed in this Ph.D. study. Like KK methods, the DC-Value method can also reconstruct the full optical field (amplitude and phase information) from the intensity of the optical field. The working principle of the DC-Value method is based on iteratively imposing the SSB and DC-Value properties of the minimum phase signal, referred to as minimum phase condition (MPC), in the Fourier domain. The DC-Value method has the potential to provide an upsampling free signal reconstruction process at low tone power operation [2]–[4].

So far, we performed an extensive survey on the state of the art SCOH methods, investigated their limitations, and proposed a novel solution namely the DC-Value method that can be operated at Nyquist sampling rate with low tone power operation. The key idea for enabling the SCOH is the reception of a signal that satisfies the minimum phase condition upon detection. The conventional KK, upsampling-free KK, and the DC-Value method are three methods whose working principle is based on the minimum phase signal transmission/reception. For SCOH transceivers, there are two methods to generate the minimum phase signal, (i) optical, and (ii) digital methods. The optical method increases the optical complexity and hardware requirement, therefore, we focused on a digital method in this Ph.D. study. Also, the KK and DC-Value methods require the implementation of the Hilbert filter and the MPC in algorithms, respectively. In chapter 4, the implementation of algorithms is explained in detail considering the location (right or left edge) of the optical tone. Also, it explains the experimental setup employed for the performance assessment. The experimental assessment was carried out for the short-reach optical links (up to 80 km) employing advanced modulation formats link QPSK and 16QAM. The comparative analysis of the performance of the KK, upsampling-free KK, and the DC-Value methods are presented. The experimental results show that the DC-Value method outperforms the KK methods, enabling a significant reduction of CSPR (2.7 dB with QPSK and 1 dB with 16QAM) [5].

Further, we presented that the performance of the DC-Value method is highly dependent on the receiver estimation of the carrier power that reaches the photodetector. It is because the carrier contribution factor (CCF) is an important parameter in the DC-Value method as it is used to guarantee the MPC for the DC-Value method algorithm. Therefore, an accurate CCF estimation method is mandatory to exploit all advantages of the DC-Value method. The CCF sensitivity analysis shows that the CCF estimation error should be no more than 5% to ensure close to optimum system performance. Using the knowledge of the CSPR value, we proposed a novel CCF estimation method compatible with both DC and AC-coupled photodetectors. The numerical analysis shows that the proposed CCF estimation method is quite insensitive to the CSPR value. In practice, results show that the optimum CSPR value usually lies higher than ~8 dB and we can ensure less than 1% CCF estimation error by the proposed method. [6].

As modulation order increases, the constellation points get closer together for the same average power, making them less tolerant to noise and impairments. The increased power can provide higher tolerance to noise, nevertheless, it also increases the nonlinearities. On the other hand, the decreased power helps reduce nonlinearities, but conversely, it reduces the noise tolerance level. The probabilistic constellation shaping (PCS) is an advanced modulation format technique that addresses the limitations of conventional QAM modulation employing the Maxwell-Boltzmann distribution to constellation points. Generally, the PCS can be realized by probabilistic amplitude shaping (PAS), and we discussed the architecture

of the PAS in detail. We also discuss the performance assessment metric such as generalized mutual information (GMI) and normalized generalized mutual information (NGMI) used in probabilistic shaping (notice that these metrics are also applicable to uniform modulation formats). The experimental results for the net 100 Gbps bit rate system were carried out for 36 & 64QAM PCS modulation and with the uniform 16QAM modulation. The experimental assessment shows that the 36QAM PCS provides better performance when compared to uniform 16QAM and 64QAM PCS modulations. It is because both peak to average power ratio (PAPR) and shaping gain increase with a larger constellation size, however, the higher PAPR indicates that the signal is more sensitive to the effective number of bits (ENOB) and CSPR. Therefore, the optimum constellation size in PCS depends on various parameters such as PAPR, ENOB, and CSPR [7].

7.2 Future Work

Many different ideas and future directions arose during this Ph.D. research. Some of them were deeply analyzed during the entire course of the research work but still there were others that due to time constraints were not possible to follow. The following ideas could be explored:

- In Chapter 4, we used a digital method to generate an SSB signal that reduces the digital to analog converter (DAC) resolution for the information-bearing signal. As an alternative, an optical method can also be used. Also, it is worth looking at [8], that reports a method where a radio frequency (RF) tone is added in the analog domain between the arbitrary waveform generator (AWG) and the IQ Mach–Zehnder modulator (IQ-MZM).

- For the case of using a digital method to generate an SSB signal, a lot of harmonics were observed after the IQ-MZM in the optical spectrum analyzer (OSA). The development of techniques to mitigate the impact of the DAC and IQ-MZM can be explored.

- In Chapter 6, we discussed that the PAPR, ENOB, and CSPR play a vital role in defining the optimum constellation size for probabilistic shaping. Following [9], a detailed analysis of signal and system design parameters such as bandwidth, CSPR, modulation order, probabilistic shaping, and chromatic dispersion can be performed in this direction.

- So far, we added a CW tone at the transmitter side, nevertheless, it is worth to explore the possibility to add at the receiver end as well. In this case, we can use an existing setup of a conventional coherent transmitter and use a simplified receiver in place of a conventional coherent receiver.

- Also, a thorough investigation like [10] showing the impact of optical amplifiers can be performed for the SCOH transceiver with probabilistic shaping.

⋆ ⋆ ⋆ ⋆ ⋆

References

[1] I. Alimi, R. Patel, N. Silva, *et al.*, "A Review of Self-Coherent Optical Transceivers: Fundamental Issues, Recent Advances, and Research Directions," *Applied Sciences*, vol. 11, no. 16, 2021.

[2] R. K. Patel, I. A. Alimi, N. J. Muga, *et al.*, "Optical Signal Phase Retrieval With Low Complexity DC-Value Method," *IEEE/OSA Journal of Lightwave Technology*, vol. 38, no. 16, pp. 4205–4212, 2020.

[3] N. J. Muga, R. K. Patel, I. A. Alimi, *et al.*, "Self-coherent optical detection for access and metro networks," *International Conference on Transparent Optical Networks (ICTON)*, pp. 1–4, 2019.

[4] N. J. Muga, R. K. Patel, I. A. Alimi, *et al.*, "DSP Optimization for Simplified Coherent Receivers," *International Conference on Transparent Optical Networks (ICTON)*, pp. 1–4, 2020.

[5] R. K. Patel, F. P. Guiomar, M. A. Fernandes, *et al.*, "Virtual Carrier Assisted Self-Coherent Detection Employing DC-Value Method," *Optical Fiber Communications Conference and Exhibition (OFC)*, pp. 1–3, 2021.

[6] R. K. Patel, F. P. Guiomar, M. A. Fernandes, *et al.*, "Impact of the Carrier Contribution Factor in the Self-coherent DC-value Method," *Optics Express*, vol. 29, no. 25, pp. 41 234–41 245, 2021.

[7] R. K. Patel, F. P. Guiomar, M. A. Fernandes, *et al.*, "Implementation of Self-Coherent DC-Value Method with Adaptive Probabilistic Constellation Shaping," *to be submitted to IEEE/OSA Journal of Lightwave Technology*, 2022.

[8] X. Chen, C. Antonelli, S. Chandrasekhar, *et al.*, "Kramers–Kronig Receivers for 100-km Datacenter Interconnects," *IEEE/OSA Journal of Lightwave Technology*, vol. 36, no. 1, pp. 79–89, 2018.

[9] E. S. Chou, H. Srinivas, and J. M. Kahn, "Phase retrieval-based coherent receivers: Signal design and degrees of freedom," *Journal of Lightwave Technology*, vol. 40, no. 5, pp. 1296–1307, 2022.

[10] D. Che, J. Cho, and X. Chen, "Does Probabilistic Constellation Shaping Benefit IM-DD Systems Without Optical Amplifiers?" *IEEE/OSA Journal of Lightwave Technology*, vol. 39, no. 15, pp. 4997–5007, 2021.

Appendices

Appendix A

Hilbert Transform

Hilbert transform of a signal is defined as the transform in which the phase angle of all negative spectral components of the signal are shifted by $\pm 90^o$, and positive spectral components are shifted by $\mp 90^o$. There are two cases of Hilbert transform, (i) Case I employed to generate upper sideband (USB) single sideband (SSB) signal (used in the case of negative carrier frequency), and (ii) Case II employed to generate lower sideband (LSB) SSB signal (used in the case of positive carrier frequency). If we consider a filter $H(\omega)$, described in Figure A.1, that has a unity magnitude response for all frequencies and the phase response is $\pi/2$ (or $-\pi/2$) for all positive frequencies and $-\pi/2$ (or $\pi/2$) for negative frequencies. Here, we

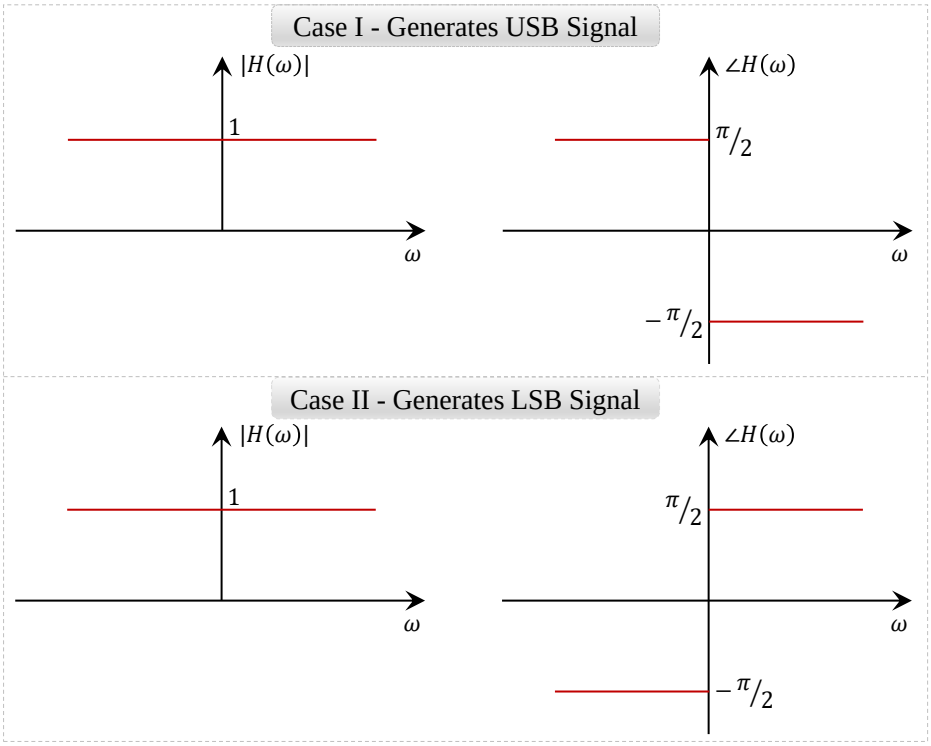

Figure A.1: Magnitude and phase of Hilbert transform filter. Case I generates USB SSB signal used in case of negative carrier frequency, and Case II generates LSB SSB signal used in case of positive carrier frequency.

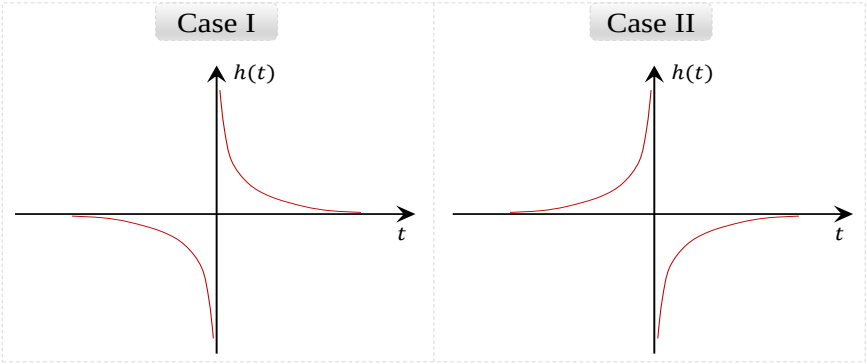

Figure A.2: Impulse response $h(t)$ of Hilbert transform filter. Case I used to generate USB SSB signal used for negative carrier frequency, and Case II used to generate LSB SSB signal used in case of positive carrier frequency.

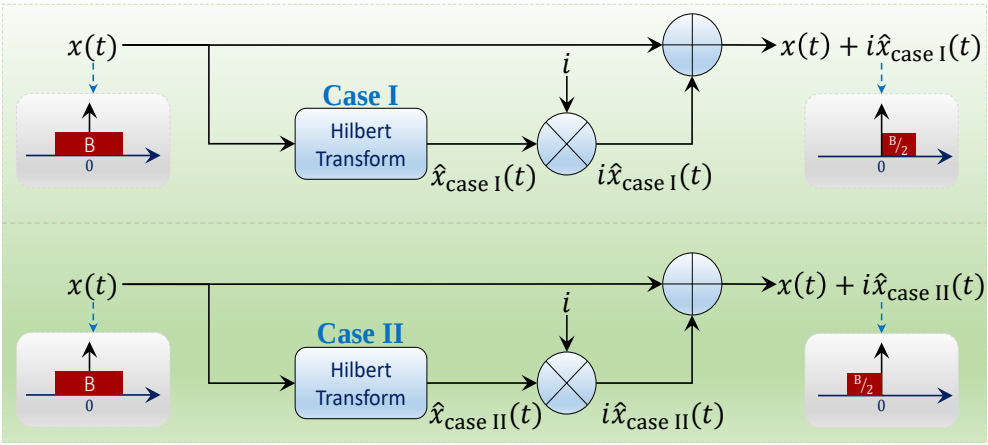

Figure A.3: Generation of an USB and LSB SSB using Hilbert transform.

consider Case II for the analysis and its transfer function can be written as,

$$H(\omega) = i\,\mathrm{sign}(\omega) = \begin{cases} i & \text{for } i > 0 \\ -i & \text{for } i < 0 \\ 0 & \text{for } i = 0 \end{cases} \tag{A.1}$$

The impulse response of this filter can be given as,

$$\begin{aligned} h(t) &= \mathcal{F}^{-1}[H(i\omega)] \\ &= i\mathcal{F}^{-1}[\mathrm{sign}(\omega)] \\ &= i\left(\frac{i}{\pi t}\right) \\ &= -\frac{1}{\pi t} \end{aligned} \tag{A.2}$$

where $\mathcal{F}^{-1}$ is the inverse transform. Similarly, the impulse response for Case I can be written as $\frac{1}{\pi t}$. The graphical representation of the impulse response of the Hilbert transform is shown in Fig. A.2. Also, the procedure shown in Fig. A.3 presents the SSB signal generation steps using Hilbert transformation. Subsequently, we present the implementation of discrete time Hilbert transform that can be employed in a practical system.

Appendix B

Implementation of Discrete Time Hilbert Transform

Equation (A.1) is extended from $-\infty$ to ∞ in the frequency domain. In the time domain, the number of points must be limited (say, to $2M+1$), which is equivalent to adding a rectangular window to the input signal. The Z-transform of windowed $h(nt_s)$ is given as,

$$H(z) = \sum_{n=-M}^{M} h(nt_s)z^{-n} \tag{B.1}$$

By definition, the equation is not causal because summation starts from a negative value. In order to implement it into the practice, (B.1) must be made causal. The FIR design scheme can be used to achieve the discrete Hilbert transform.
1: Write the Z-transform of the function $h(nt_s)$ as,

$$\begin{aligned} H(z) &= \sum_{n=-\infty}^{\infty} h(nt_s)z^{-n} \\ &= \sum_{n=\infty}^{-1} h(nt_s)z^{-n} + h(0) + \sum_{n=1}^{\infty} h(nt_s)z^{-n} \\ &= h(0) + \sum_{n=1}^{\infty}[h(-nt_s)z^{n} + h(nt_s)z^{-n}] \end{aligned} \tag{B.2}$$

Substituting $z = e^{i2\pi ft_s}$, the result can be written as,

$$\begin{aligned} H(e^{i2\pi ft_s}) &= H_r(e^{i2\pi ft_s}) + iH_i(e^{i2\pi ft_s}) \\ &= \sum_{n=-\infty}^{\infty} h(nt_s)e^{i2\pi nft_s} \\ &= h(0) + \sum_{n=1}^{\infty}[h(-nt_s)\cos(2\pi nft_s) + ih(-nt_s)\sin(2\pi nft_s) + \\ &\quad h(nt_s)\cos(2\pi nft_s) + ih(nt_s)\sin(2\pi nft_s)] \end{aligned} \tag{B.3}$$

where,

$$\begin{aligned} H_r(e^{i2\pi ft_s}) &= h(0) + \sum_{n=1}^{\infty}[h(-nt_s) + h(nt_s)]\cos(2\pi nft_s) \\ H_i(e^{i2\pi ft_s}) &= \sum_{n=1}^{\infty}[h(-nt_s) + h(nt_s)]\sin(2\pi nft_s) \end{aligned} \tag{B.4}$$

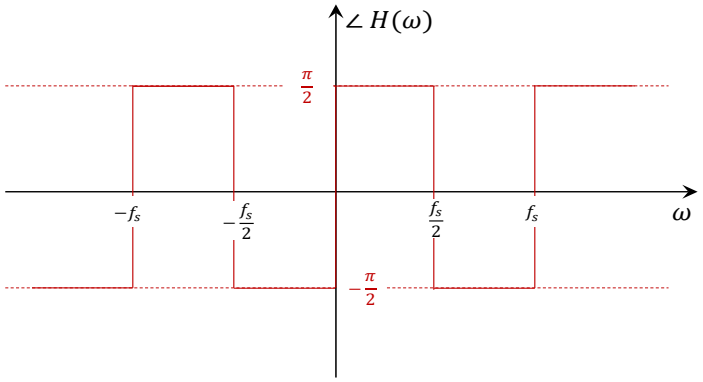

Figure B.1: Periodic representation of $H(f)$

2: When the sampling frequency is f_s, the transfer function $H(f)$ is limited to the bandwidth $\frac{f_s}{2}$. Due to the periodic property of sampling, the Hilbert transfer function is actually as shown in Figure B.1. This can be represented by Fourier series as,

$$H_i(e^{i2\pi f t_s}) = \sum_{n=1}^{\infty} b_n \sin(2\pi n f t_s) \tag{B.5}$$

$$\begin{aligned} b_n &= \frac{2}{f_s}\int_{-f_s/2}^{f_s/2} H(e^{i2\pi n f t_s})\sin(2\pi n f t_s)\ df \\ &= \frac{2}{f_s}\left[\int_{-f_s/2}^{0} \sin(2\pi n f t_s)\ df + \int_{0}^{f_s/2} \sin(2\pi n f t_s)\ df\right] \\ &= \frac{1}{n\pi}[-2 + 2\cos(n\pi)] \\ &= \begin{cases} 0 & \text{n = even} \\ -\frac{4}{n\pi} & \text{n = odd} \end{cases} \end{aligned} \tag{B.6}$$

In the above equation, the relation of $f_s t_s = 1$ is used.
3: The (A.1) has only the imaginary part, therefore, $H_r(f) = 0$ and $H_i(f) \neq 0$. This condition can be fulfilled if,

$$h(n) = 0 \text{ and } h(-nt_s) = -h(nt_s) \tag{B.7}$$

Using this relationship, H_i in (B.4) can be written as

$$H_i(e^{j2\pi n f t_s}) = 2\sum_{n=1}^{\infty} h(nt_s)\sin(2\pi n f t_s) \tag{B.8}$$

Comparing (B.8) and (B.5), we can obtain

$$h(nt_s) = -\frac{b_n}{2} \tag{B.9}$$

Finally, the impulse response of the discrete Hilbert transform can be written as,

$$h(nt_s) = \begin{cases} 0 & \text{n = even} \\ -\dfrac{2}{n\pi} & \text{n = odd} \end{cases} \tag{B.10}$$

Similarly, the discrete Hilbert transform for the Case I can be written as,

$$h(nt_s) = \begin{cases} 0 & \text{n = even} \\ \dfrac{2}{n\pi} & \text{n = odd} \end{cases} \tag{B.11}$$

The Hilbert transform represented by (B.10) and (B.11) can be used in Kramers-Kronig (KK) methods in the case of positive and negative carrier frequency, respectively.